

AD-785 578

FEASIBILITY STUDY OF EXPLOSIVELY DRIVEN
HYPERVELOCITY PROJECTILES

Physics International Company

Prepared for:

Army Mobility Equipment Research
and Development Center

April 1974

DISTRIBUTED BY:



National Technical Information Service
U. S. DEPARTMENT OF COMMERCE
5285 Port Royal Road, Springfield Va. 22151

Unclassified

SECURITY CLASSIFICATION OF THIS PAGE (Other Data Entered)

REPORT DOCUMENTATION PAGE		READ INSTRUCTIONS BEFORE COMPLETING FORM
1. REPORT NUMBER	2. GOVT ACCESSION NO.	3. RECIPIENT'S CATALOG NUMBER <i>AD 785 578</i>
4. TITLE (and Subtitle) Feasibility Study of Explosively Driven Hypervelocity Projectiles		5. TYPE OF REPORT & PERIOD COVERED Final 1 June 1973 to 1 January 1974
7. AUTHOR(s) K. Seifert		6. PERFORMING ORG. REPORT NUMBER PIFR-559 8. CONTRACT OR GRANT NUMBER(s) DAAK02-73-C-0396
9. PERFORMING ORGANIZATION NAME AND ADDRESS Physics International Company 2700 Merced Street San Leandro, California 94577		10. PROGRAM ELEMENT, PROJECT, TASK AREA & WORK UNIT NUMBERS
11. CONTROLLING OFFICE NAME AND ADDRESS U.S. Army Mobility Equipment Research and Development Center Fort Belvoir, Virginia 22060		12. REPORT DATE April 1974 13. NUMBER OF PAGES <i>167</i>
14. MONITORING AGENCY NAME & ADDRESS (if different from Controlling Office)		15. SECURITY CLASS. (of this report) Unclassified 16. DECLASSIFICATION/DOWNGRADING SCHEDULE
16. DISTRIBUTION STATEMENT (of this Report)		
17. DISTRIBUTION STATEMENT (of the abstract entered in Block 20, if different from Report)		
18. SUPPLEMENTARY NOTES		
19. KEY WORDS (Continue on reverse side if necessary and identify by block number) hypervelocity, explosive driver, armor defeat, projectile impact, rear-surface spall, multiple projectile launch		
20. ABSTRACT (Continue on reverse side if necessary and identify by block number)		

Reproduced by
NATIONAL TECHNICAL
INFORMATION SERVICE
U S Department of Commerce
Springfield VA 22151

DD FORM 1 JAN 73 1473 EDITION OF 1 NOV 68 IS OBSOLETE

Unclassified

SECURITY CLASSIFICATION OF THIS PAGE (Other D. Is Sealed)

CONTENTS

	<u>Page</u>
SECTION 1 INTRODUCTION	1
SECTION 2 BACKGROUND	3
2.1 Conceptual System Constraints	3
2.2 Mechanics of Rear Surface Spall Induced by Projectile Impact	6
2.3 Theory and Operation of the Linear Explosive Driver	13
SECTION 3 EXPERIMENTAL PROGRAM	21
3.1 Initial Design of Launcher System	21
3.2 Launcher Development and Testing	30
SECTION 4 COMPUTATIONAL SUPPORT	65
4.1 Introduction	65
4.2 Material Models and Equations of State	65
4.3 Explosive Driver Calculation	67
4.4 Two-Dimensional Launch-Cycle Calculation	69
SECTION 5 ANALYSIS AND CONCLUSIONS	79
5.1 Analysis	79
5.2 Conclusions	81
REFERENCES	85
APPENDIX A PISCES TM 1-DE, A One-Dimensional Eulerian Continuum Mechanics Code	
APPENDIX B PISCES TM 1-DL, Manual A	

Preceding page blank

iii

ILLUSTRATIONS

<u>Figure</u>	<u>Page</u>
1 Rectangular Stress Pulse Prior to Interaction with Free Surface at x_0	7
2 Rectangular Stress Pulse Reflecting from a Free Surface Prior to the Onset of Tension	8
3 Onset of Tension for a Reflected Rectangular Stress Pulse	8
4 Stress Pulse After Complete Reflection by a Free Surface at x_0	9
5 Triangular Stress Pulse Prior to Interaction with Free Surface at x_0	10
6 Onset of Tension for a Reflected Triangular Stress Pulse	10
7 Stress Pulse (Real and Virtual) for Remaining Material After Spall has Occurred	11
8 Ideal Operation of the Linear Explosive Driver	14
9 Operation of a Single-Stage Explosively-Driven Launcher	18
10 Possible Projectile-Sabot Assembly and Launch Sequence	23
11 Ballistics of Projectile Acceleration	25
12 SAHA Equation for Helium	29
13 Configuration of the First Experiment	34
14 Blunderbuss-1 x-t Plot	35

Preceding page blank

CONTENTS (Cont.)

<u>Figure</u>		<u>Page</u>
15	MERDC Blunderbuss-5 Detail	37
16	Radiograph of Projectile in Flight from Blunderbuss-1	38
17	Configuration of the Second Experiment	40
18	Blunderbuss-2 x-t Plot	43
19	Collapsed Pressure Tube from Shot Blunderbuss-2	44
20a	Front View of 1-Inch-Thick Armor Target After Impact	45
20b	Rear View of 1-Inch-Thick Armor Target After Impact	45
21	Configuration of Third Experiment	47
22	Blunderbuss-4--Projectile Design	49
23	Configuration of Fourth Experiment	50
24	Blunderbuss-5 Just Prior to Firing	53
25	Projectile from Blunderbuss-5 in Flight	54
26	Blunderbuss-7--Barrel Extender	56
27	Blunderbuss-7 Detail	57
28	Flash Radiograph of Projectile from Blunderbuss-7 in Flight	58
29	Sabot for Blunderbuss-8	61
30	MERDC Launch Cycle Study--Blunderbuss-8	62
31a	Sabot for Blunderbuss-8	63
31b	Projectiles for Blunderbuss-8	63
31c	Sabot for Blunderbuss-8	63
32	Velocity Vector Plot of the Final Composition C-4 Explosive Driver at a Time of 10 μ sec	68

CONTENTS (Cont.)

<u>Figure</u>		<u>Page</u>
33	Velocity Vector Plot of the Final Composition C-4 Explosive Driver at a Time of 80 μ sec	70
34	Velocity Vector Plot of the Composition C-4 Explosive Driver with the Full Barrel and Launcher at a Time of 10 μ sec	72
35	Initial Zoning for the Two-Dimensional Launch Cycle Calculation	73
36	Final Configuration of the Two-Dimensional Launch Cycle Calculation at a Time of 10 μ sec	75
37	State of Stress in the Projectile for the Two-Dimensional Calculations	76

SECTION 1

INTRODUCTION

Conceptually, a barrier weapon system consisting of a warhead that could deliver a large number of projectiles at very high velocities would be an extremely effective method of defeating armored vehicles such as tanks and personnel carriers. Assuming that the projectiles could be adequately dispersed, the principal advantage of such a warhead would be the larger target area that could be covered with one warhead. Since the energy required to launch projectiles to a given velocity is a direct function of the projectile mass, twenty times as many 5-gram projectiles could be launched to a specific velocity as a single 100-gram projectile. Thus, for a given launcher weight and volume, a much larger area could be controlled by the use of a number of smaller projectiles. Furthermore, the hyper-velocity projectiles would not be required to penetrate the armored vehicles since the lethality of the fragments spalled from the rear surface of the armor would be expected to neutralize the soft components inside the vehicle. For example, projectiles of 1 to 5 grams with velocities in the neighborhood of 10 km/sec would cause spallation on 1-inch armor plate currently in use. Of course, one of the most critical items in such a weapon is a launcher that is sufficiently portable and compact that it may be delivered ballistically and that is also adequate to launch a number of small projectiles to the high velocities that would be required. Most launching systems capable of accelerating integral projectiles to 10 km/sec are too massive to be weaponized. However, an explosively-driven

launcher (References 1-7) capable of launching multiple 1- to 5-gram projectiles to 10 km/sec showed promise of weaponization.

The objectives of the six-month program reported here were: (1) to demonstrate the ability of an explosive driver to launch a projectile to 9 to 10 km/sec within a total length of 1 meter and, (2) to determine the feasibility of launching multiple projectiles using the above launcher.

The first objective was accomplished by launching approximately 25 projectiles to greater than 9 km/sec. Although the launching of intact multiple projectiles was not achieved, such a goal is believed achievable.

SECTION 2 BACKGROUND

The program performed was a feasibility study to evaluate the possibility of developing an explosive driver hypervelocity launcher capable of launching simultaneously many small projectiles to velocities of 10 km/sec. Any feasible launcher developed must be capable of being incorporated into a weapon system. To design a launcher system effectively, its ultimate usage must be kept in mind: generation of rear surface spall on armored vehicle targets. The following subsections present background information concerning the constraints placed on the launcher, rear surface spall phenomena, and the explosive driver concept.

2.1 CONCEPTUAL SYSTEM CONSTRAINTS

The parameters shown in Table I define goals for a conceptual system (Reference 8). Note that the restrictions placed upon the feasibility study parameters are, in most cases, significantly relaxed from the conceptual system constraints.

TABLE I
HYPERVELOCITY LAUNCHER PERFORMANCE PARAMETERS

<u>Item</u>	<u>Conceptual System Parameters</u>	<u>Feasibility Program Parameters</u>
Impeller mass	2-50 kgm	Less than 10 kgm
Total warhead length (include acceleration portion)	Less than 1 meter	No restriction
Impeller diameter	Less than 40 cm	No restriction
Environment	Ground level Atm.	No restriction
Projectile flight distance	10-100 meters	No restriction
No. projectiles per warhead	20-1000	1-10
Mass of individual projectile	0.5-5 gm	1 gm
Density of individual projectile	0.7-20 gm/cm ³	To be determined
Projectile aerodynamic drag coefficient	Less than 0.2	No restriction
Projectile ejection velocity	6-10 km/sec	9-10 km/sec
Impact velocity	5-8 km/sec	No restriction
Ejection half angle (with respect to warhead axis)	15°-40°	15°-20°
Prime target: steel armor	1.5-6 cm thick	No restriction

Explosive drivers have been used in the past to launch single projectiles of different shapes to velocities of up to 12 km/sec. However, these launcher systems were considerably longer than the 1-meter length required for the conceptual system given in Table I. These launcher systems were necessarily long to have sufficient launcher gas mass without correspondingly high reservoir pressures.* Therefore, once a required system volume, length, and diameter are set and the areal density of the projectile is given, the minimum required reservoir or initial projectile base pressure is fixed. Any relaxation of the warhead length for a feasibility study would represent a reduction in the reservoir pressure and, therefore, failure to establish operational feasibility at the required system pressure.

The launcher system to be developed would therefore have the following restrictions: length--1 meter; diameter--less than 40 cm; muzzle velocity--9 to 10 km/sec. All of the tests would be conducted at range pressures of 1 atmosphere and in air. By adhering to these constraints, the feasibility of developing a weaponizable system for launching multiple hypervelocity projectiles could best be evaluated.

*The final gas pressure in the reservoir is proportional to the initial gas density and the square of the explosive detonation velocity.

2.2 MECHANICS OF REAR SURFACE SPALL INDUCED BY PROJECTILE IMPACT

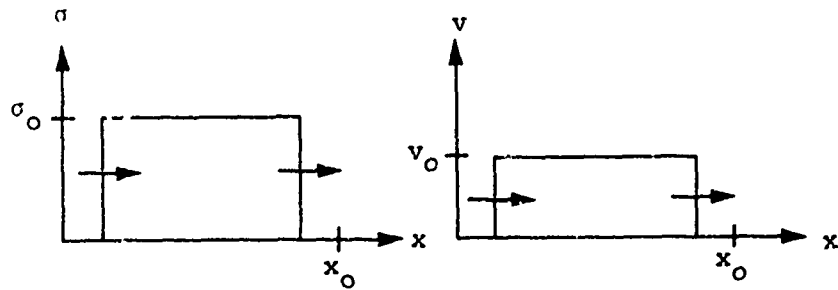
The impact of a high velocity projectile upon a slab of material results in a compressive stress pulse in the target that propagates away from the point of impact. This stress pulse contains most of the momentum carried by the projectile prior to the impact. When this compressive pulse encounters a free surface, it reflects and produces tension near the surface; if the cohesive strength of the material is exceeded, fracture occurs, and some or all of the momentum of the stress pulse is carried off in the resulting fragments of the material. This process of dynamic fracture by reflection of a compressive stress pulse at a free boundary is termed "spall."

The character and depth of the spall are greatly influenced by the amplitude, shape, and spatial width of the compressive stress pulse. These factors are, in turn, dependent upon the size, velocity, and composition of the projectile, and the material properties of the target.

To illustrate how the nature of the compressive pulse influences the characteristics of spall, let us consider two simple cases. First assume a rectangular elastic pulse, as in

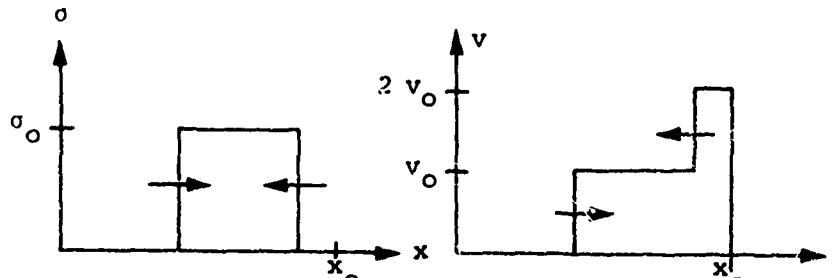
Figure 1, with amplitude σ_0 , moving toward a free surface at x_0 . For this discussion stress will be treated as positive in compression. The material contained within the pulse is moving toward x_0 with a velocity $v_0 = \sigma_0/\rho c$, where ρ and c are the density and sound speed of the material (Figure 1). Elsewhere, the material is at rest. When the loading portion of the pulse meets the free rear surface, it reflects and becomes an unloading wave, relieving the stress in the material ahead of it to a stress-free state, but in the process increasing its velocity by a factor of two (Figure 2). As the right-going and left-going unloading waves cross, they each enter unstressed material. Each wave reduces the magnitude of the stress in the material ahead of it by an amount σ_0 , so a tensile stress of $-\sigma_0$ is produced as in Figure 3.

If the magnitude of the tensile stress at this point is sufficient to produce fracture, spall will occur, and the material to the right of the failure location will move off with velocity somewhat less than $2v_0$, leaving the material behind at rest, and with both portions stress free (or nearly so).



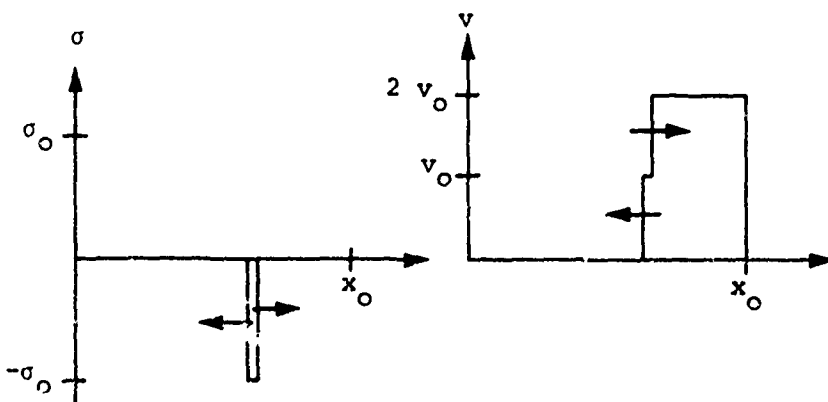
(a) Stress versus distance (b) Particle velocity versus distance

Figure 1 Rectangular stress pulse prior to interaction with free surface at x_0 .



(a) Stress versus distance (b) Particle velocity versus distance

Figure 2 Rectangular stress pulse reflecting from a free surface prior to the onset of tension.



(a) Stress versus distance (b) Particle velocity versus distance

Figure 3 Onset of tension for a reflected rectangular stress pulse.

Note that the initial tension (and hence failure) develops at a distance from the free surface equal to half the spatial width of the incident compressive stress pulse. If no fracture occurs, the right-going unloading wave reflects from the free surface and becomes a left-going loading wave that increases the negative stress (tension) to an unstressed level (Figure 4).

Next, consider a triangular compressive stress pulse, as in Figure 5. The development of the tension is somewhat easier to visualize in this case by construction of a virtual reflected pulse that becomes real as it enters the material. The stress at each instant is then the superposition of the portions of the two pulses that lie within the material. The stress state at a later time--when the reflected pulse enters the material--is shown in Figure 6. Note that the largest tension at each instant results from the superposition of the peak of the left-going wave with successive portions of the right-going wave. Since the right-going wave is compressive, it always acts to reduce the tension. Once the left-going wave passes the last

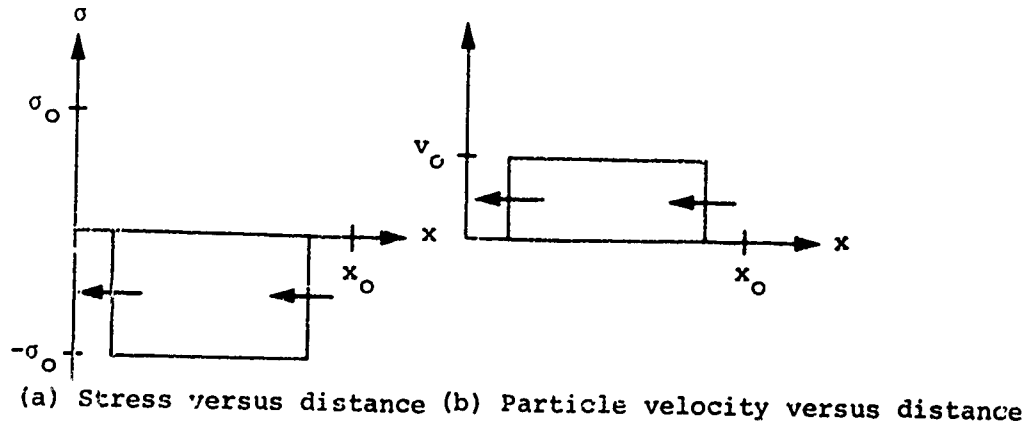


Figure 4 Stress pulse after complete reflection by a free surface at x_0 .

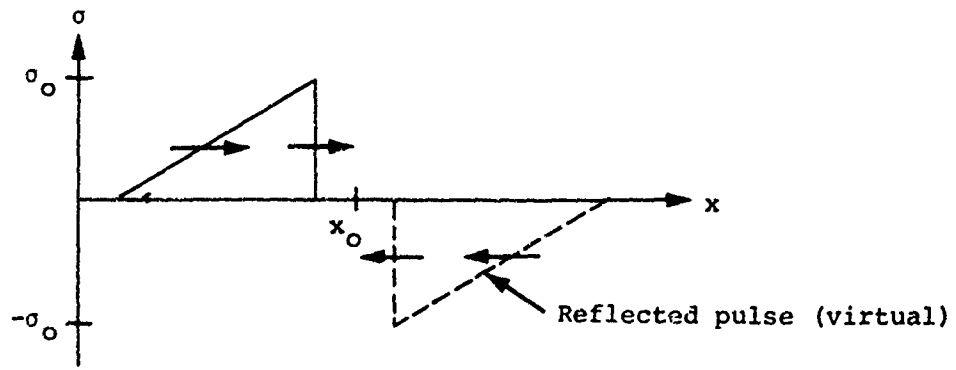


Figure 5 Triangular stress pulse prior to interaction with free surface at x_0 .

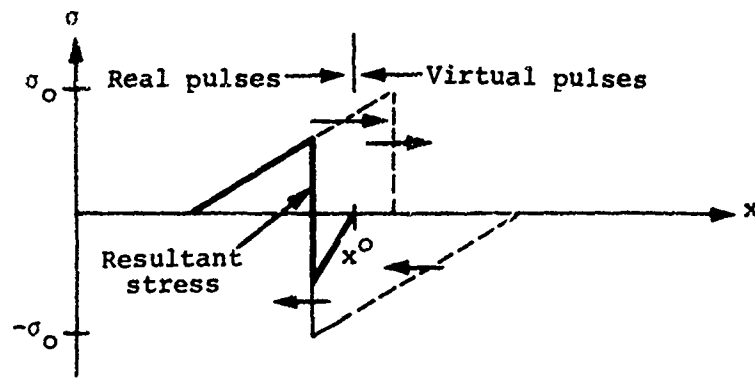


Figure 6 Onset of tension for a reflected triangular stress pulse.

portion of the right-going wave, no further increase in tension occurs. Since both waves are moving with the same speed (or nearly so, even when non-linear materials are encountered) in the absence of spall, the peak tension is again developed at a distance from the free surface equal to half the spatial width of the incident stress pulse.

Now let us consider how the spall process develops when the peak stress for a triangular pulse is large compared to the spall strength of the material. If, for instance, a spall plane suddenly formed at the point of peak tension at the time illustrated in Figure 6, a new free surface would be created there; no tension would remain in the material, but the remaining material would still contain a right-going compressive pulse that would reflect from the new free surface and hence develop additional tension (Figure 7). The process of the buildup of tension and spall then occurs repeatedly until the leading edge of the reflected pulse passes the trailing edge of the incident pulse, and no further tensile stress increases occur.

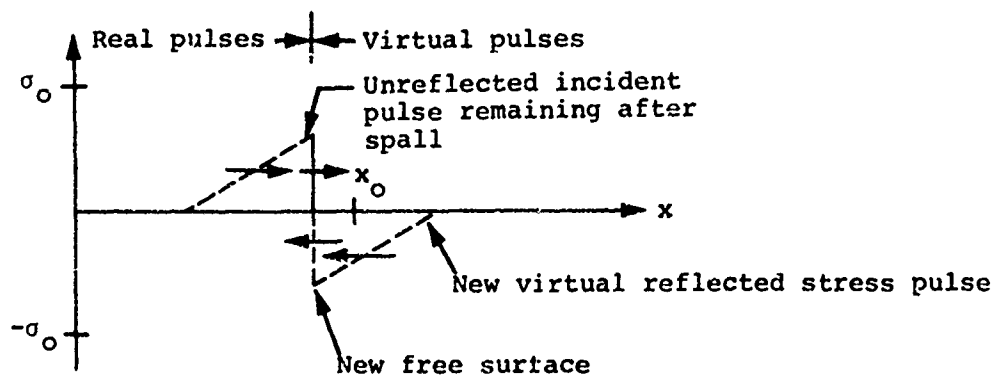


Figure 7 Stress pulse (real and virtual) for remaining material after spall has occurred.

A few generalizations can be made from these simplified analyses. The maximum depth of spall will not exceed half of the spatial width of the incident stress pulse. For a triangular pulse with a peak that greatly exceeds the spall strength, multiple spalls will occur and will probably produce a spray of very fine fragments. A more rectangular (flat-topped) stress pulse will produce fewer spall layers and will lead to comparatively large spall fragments. (For an introduction to stress wave effects, see References 9 to 11. More advanced treatments are found in References 12 and 13.)

The impact conditions (i.e., projectile size, geometric configuration and velocity) will establish the initial amplitude and duration (and hence spatial width) of the compressive stress pulse. The material properties of the target will affect the form of the pulse as it propagates toward the free rear surface, especially if the pulse must travel a large distance compared to its width. For many materials impacted to high stress levels, the decrease in compressibility with increasing pressure causes the stress pulse to become roughly triangular after propagation. However, the pressure-induced phase transition that occurs in iron and mild carbon steels at around 150 kbar leads to rarefaction shock upon unloading, which, in turn, causes a nearly flat-topped stress pulse to develop. Consequently, the character of the spall fragments in these materials may be quite different than that in materials in which no phase changes are produced.

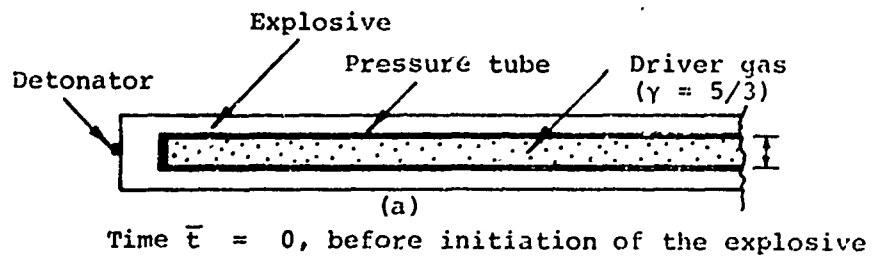
Typical armors used in combat vehicles (iron base armors) undergo this phase transition around 150 kbar. The unloading shock caused by this phenomenon, when subjected to projectile impact, leads to the creation of rear surface spall fragments. The goal of the program being conducted is to study the feasibility of a launcher capable of accelerating multiple projectiles to hypervelocities that, when impacting armored vehicles, would utilize this rear surface spall mechanism to neutralize "soft components" within the vehicle.

2.3 THEORY AND OPERATION OF THE LINEAR EXPLOSIVE DRIVER

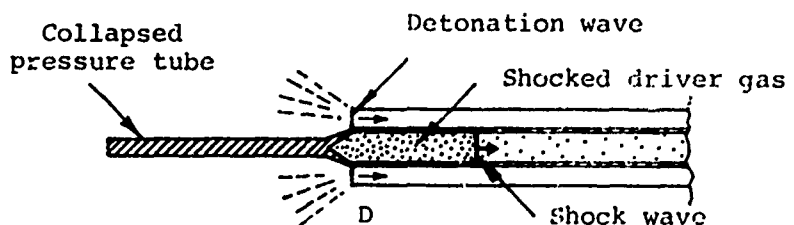
The linear explosive driver represents a technique whereby a substantial portion of the chemical energy of an explosive is converted in a controlled manner to the kinetic and internal energy of a gas. Basically, the energy densities in the gas are produced by a strong shock generated by the progressive collapse of a tube. The collapse of the tube is such that it may be represented as a piston propagating into a gas. The model used to describe the ideal operation of the driver is quite similar to that used to explain the basic discontinuous motion produced by a piston in one-dimensional gasdynamics.

The operational characteristics of the linear explosive driver are shown in Figure 8. A thin-walled metal tube (the pressure tube) containing the driver gas is surrounded by a chemical explosive. After a detonation is initiated in the explosive, a detonation wave propagates in the explosive along the outside of the metal tube. The pressure behind the detonation wave accelerates the tube wall in toward the axis, sealing the tube and forming a conical-shaped piston (Figure 8b). The velocity of the piston is equal to the detonation velocity of the explosive (D). The motion of this piston generates a strong shock wave in the stationary column of the driver gas. If the gas behaves ideally (i.e., the ratio of the specific heats, γ , of the gas is constant), then the velocity of the shock wave, S , is $(\gamma + 1) D/2$. The position-time histories of the piston and shock wave are shown in Figure 8c for an ideal driver gas ($\gamma = 5/3$). These trajectories are presented in the dimensionless coordinates:

$$\bar{x} = \frac{x}{d} \text{ and } \bar{t} = \frac{Dt}{d}$$

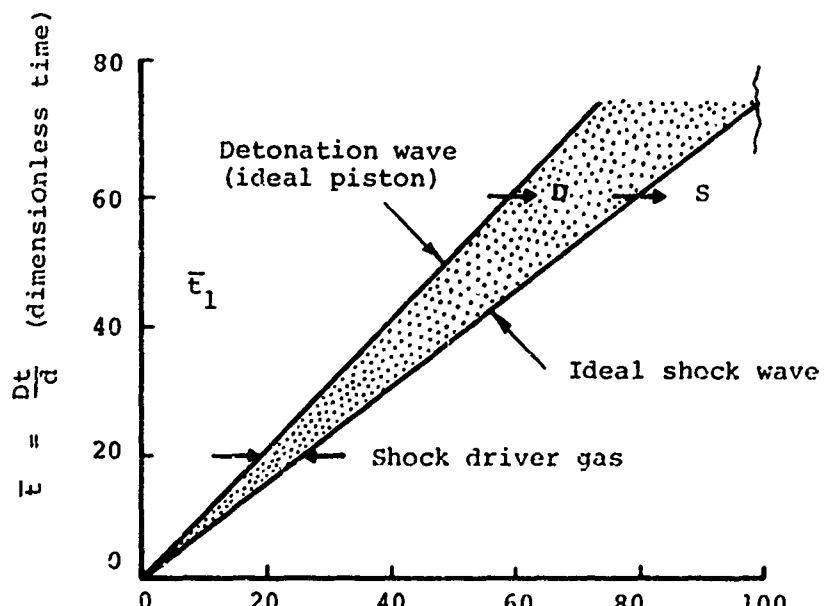


Time $\bar{t} = 0$, before initiation of the explosive



(b)

Time $\bar{t} = \bar{t}_1$, after initiation of the explosive



$$\bar{x} = \frac{x}{d} \quad (\text{dimensionless distance})$$

Position-time history of shock and detonation wave

Figure 8 Ideal operation of the linear explosive driver.

where x and t are the distance and time after the shock wave begins to move ahead of the detonation wave, d is the internal diameter of the pressure tube, and D is the detonation velocity of the explosive. The use of these coordinates facilitates the comparison of drivers having pressure tubes of different dimensions or utilizing explosives with different detonation velocities. It should be noted that in this coordinate system all slopes are normalized with respect to the detonation velocity of the explosive. For example, in Figure 8c the trajectory of the detonation wave has a slope of unity, while that of the shock wave has a slope of four-thirds:

$$\left(\frac{S}{D} = \frac{\gamma + 1}{2}, \gamma = \frac{5}{3} \right)$$

The thermodynamic state of the shocked gas (subscripts 1) is described by the following relations:

Pressure: $P_1 = \rho_0 \left(\frac{\gamma + 1}{2} \right) D^2 \quad (1)$

Temperature: $T_1 = \frac{T_0 \rho_0}{P_0} \left(\frac{\gamma - 1}{2} \right) D^2 \quad (2)$

Density: $\rho_1 = \left(\frac{\gamma + 1}{\gamma - 1} \right) \rho_0 \quad (3)$

Sound speed: $a_1 = \sqrt{\frac{\gamma(\gamma - 1)}{2}} D \quad (4)$

where ρ_0 , P_0 , and T_0 are the initial density, pressure, and temperature of the unshocked gas. These relations assume that

the initial pressure in the unshocked gas is quite small compared to the corresponding quantities in the shocked gas. It is noted that, for a given ideal gas, the magnitude of each of these properties, except density, is a function of the piston velocity (detonation velocity).

Using the ideal theory for reflection of a strong shock from a rigid wall, the gasdynamic conditions in the reservoir may be calculated. The pressure, temperature, and sound speed, for example, are found from the relations:

$$P_2 = \frac{3\gamma - 1}{\gamma - 1} P_1 = \left(\frac{3\gamma - 1}{\gamma - 1} \right) \left(\frac{\gamma + 1}{2} \right) P_0 D^2 \quad (5)$$

$$T_2 = \frac{3\gamma - 1}{\gamma} T_1 = \frac{T_0 P_0}{P_0} \left(\frac{\gamma - 1}{2} \right) \left(\frac{3\gamma - 1}{\gamma} \right) D^2 \quad (6)$$

$$a_2 = \sqrt{\frac{(3\gamma - 1)(\gamma - 1)}{2}} D \quad (7)$$

The performance of linear explosive drivers has been demonstrated over a wide range of experimental parameters. Internal diameters of pressure tubes made of copper, steel, lead, and aluminum have ranged from 1/4 inch to 16 inches; high-explosive weight has ranged from 27 grams to 9200 pounds; the explosive-to-pressure tube mass ratio has been varied from 0.5 to 10; driver gases have included helium, air, argon, and hydrogen; the initial pressure of the driver has been varied from 15 to 2450 psi; and the detonation velocities of the explosives used (liquid and solid) have ranged between 5.5 km/sec and 8.6 km/sec. While some of these tests have been one of a kind, the majority were essential to comprehensive experimental studies of a particular explosive driver design.

Although the performance of many of the drivers adheres closely to the ideal predictions, certain departures may occur. Four phenomena have been incorporated in a model of explosive driver operation to account for observed departures from the ideal driver performance described above. They are (1) radial expansion of the pressure tube behind the shock wave, (2) decomposition or predetonation of the driver explosive during the period of pressure tube expansion, (3) the effect of boundary-layer growth behind the shock wave, and (4) formation of a metal, gas, or metal-gas jet by the collapsing pressure tube. These phenomena are inter-related through the kinetics produced by the imploding pressure tube. Their interdependence is such that changes in driver behavior resulting from certain experimental parameter changes cannot be attributed solely to a particular phenomenon. However, the ability of the model to explain, predict, and control the behavior of explosive drivers justifies the categorization of these phenomena. A detailed discussion of these four phenomena is presented in References 1 through 4 and 14.

In a typical gun design the explosive driver is coupled to the barrel of the gun by a massive steel reservoir section. Materials used to form the reservoir section during the course of launcher development included lead, steel, concrete, and explosive. Guns have been operated in both the chambraged and unchambraged mode. When the strong shock generated by the explosive driver reaches the chambrage plane (or projectile location in an unchambraged gun), it reflects and forms a reservoir of very high enthalpy gas. The reservoir of gas is then expanded to accelerate the projectile, as illustrated in the example of a chambraged gun in Figure 9.

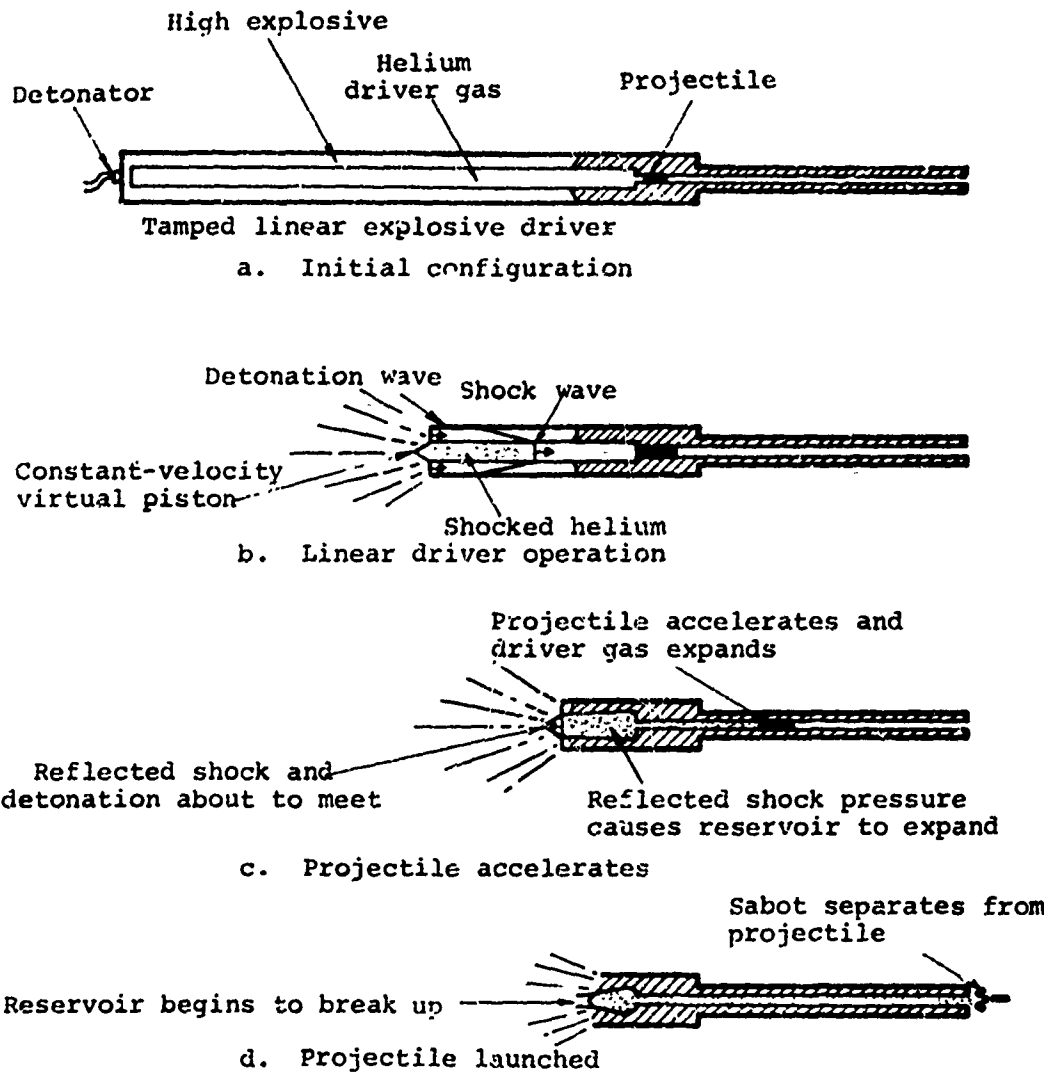


Figure 9 Operation of a single-stage explosively-driven launcher.

For launcher applications the length of shocked gas generated by the explosive driver is usually limited to less than 10 tube diameters to preclude the major effects of boundary-layer growth or pressure tube expansion. The jetting of the collapsing pressure tube that forms the piston is usually negligible in launcher applications because of the high gas pressures.

SECTION 3

EXPERIMENTAL PROGRAM

The program, as conceived, was essentially an experimental program designed to provide sufficient information to evaluate the feasibility of the successful development of a multiple projectile hypervelocity launcher utilizing explosive drivers. In this role the program was structured as a "cut-and-try" evolution of possible launcher designs. Successful features of launchers were incorporated into subsequent designs, and features deemed to be disadvantageous were replaced with more probable designs. Throughout the program the design of the launcher system was aided by computational analysis. This computational effort yielded insight into the design of the very high pressure explosive driver system, and, after the successful development of this driver, aided in attempts to evolve a launch cycle capable of accelerating intact projectiles to the required 10 km/sec.

In the following section the rationale for the original design parameters of the launcher system will be developed. The results of the testing program on actual launcher hardware will then be presented.

3.1 INITIAL DESIGN OF LAUNCHER SYSTEM

Past attempts to launch individual projectiles to hypervelocities have been more successful with projectiles constructed of an alloy of magnesium and lithium, or

Maglith. This metal has a density of 1.39 gm/cm^3 and a yield strength of about 20,000 PSI. It was decided in the initial conceptualization of the launcher that Maglith projectiles would be used for this feasibility study also.

A 1-gram sphere of Maglith has a diameter of 1.11 cm. Allowing for an additional 0.15 cm thickness of Maglith for a sabot, the areal density of the launch package would be 2.0 gm/cm^2 . The areal density was thus fixed for the program. Even if projectile materials were changed, the overall areal density of the projectile/sabot package would have to remain the same. If the areal density were to increase, a longer barrel would be needed to accelerate the assembly to a given velocity with the same pressure on the base of the projectile. Figure 10 is an example of a projectile/sabot assembly suitable for launching multiple projectiles from one barrel while maintaining a relatively low areal density.

Before one can launch a projectile/sabot assembly such as illustrated in Figure 10, one must first be able to launch a flat plate of areal density equal to 2.0 gm/cm^2 . To reach the final velocity for which a launcher system is designed, the projectile must be intact throughout the launch cycle. If the projectile, or a projectile/sabot assembly, breaks up during the launch cycle, then the velocity would be less than that achieved by an intact projectile. It is obvious that if the projectile/sabot assembly were to break up in the barrel, the integrity and velocity of the individual projectiles would be questionable at best.

An overall length of about 1 meter was selected as the basic requirement for the driver and barrel system. Basic physical principles show that very high pressures would be required

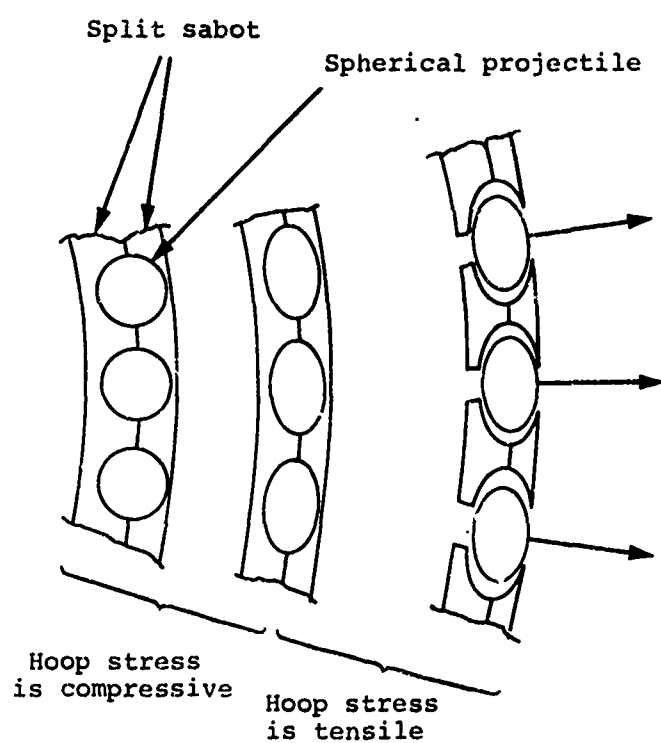


Figure 10 Possible projectile-sabot assembly and launch sequence.

to launch projectiles to 10 km/sec in such short lengths. Since the 1 meter length included both the explosive driver section and the barrel length required to reach 10 km/sec, the necessity of high chamber pressure is even more clear.

Experience with the explosive driver has shown that the most effective method of creating and containing very high pressure gases is through the use of a linear explosive driver. Alternate explosive driver techniques, such as an inverted driver system, were considered but were rejected on the basis of the very high base pressures that must be generated and contained.

For design purposes it was assumed that the launch cycle could be approximated by the launch cycle calculated in "The Theory of High Speed Guns," by A. Siegel (Reference 15). Past experience with explosive driver guns has shown this approximation to be relatively accurate; some inherent system losses are overcome by the collapse of the reservoir from external, high explosive tamping.

In the design calculations, the configuration of the launcher is assumed to be that of Figure 11. A closed breech was assumed which contained a static gas of mass (G), an initial pressure of (P_2), and an initial sound speed of (a_2). As the gas expands, it accelerates a piston of mass (M) and area (A). The assumption made in the gas dynamics cycle is that the pressure (P) of any element of gas during the expansion can be given by

$$P = P_2 (V_2/V)^\gamma$$

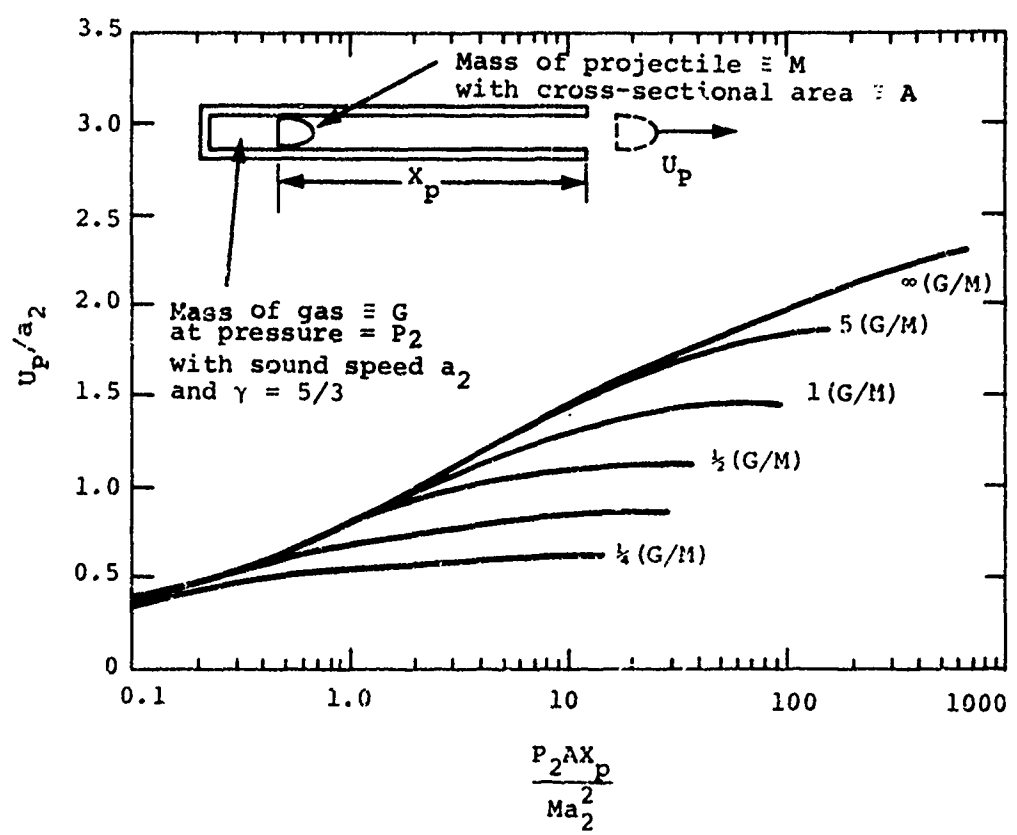


Figure 11 Ballistics of projectile acceleration.

where

v_2 is the initial volume of that gas element

v is the expanded volume of that gas element

γ is the ratio of specific heats for the gas and is assumed to be constant (for helium, $\gamma = 5/3$).

Figure 11 shows the curves (from Reference 15) which relate the projectile velocity (U_p) and the required barrel length (X_p) when the above parameters are known. Perusal of these curves indicates that high projectile velocities are facilitated by having as high a sound speed as possible in the gas. This sound speed is proportional to the detonation velocity of the explosive in the driver (see Equation 7, Section 2.3). For the system design, therefore, it was assumed that the explosive used would be similar to an HMX-based plastic bonded explosive (PBX) of the type developed and used by the Atomic Energy Commission. A typical detonation velocity of these explosives is 8.5 km/sec with a density of 1.87 gm/cc.

In the geometry of Figure 9, it is assumed that the gas from the driver stagnates when the shock impacts and reflects from the projectile/sabot assembly. Under this assumption, the conditions of the gas can be calculated to a close approximation. After trial and error it was decided that a 25-kbar driver should be used; i.e., the gas behind the initial shock wave is at a pressure of (P_1) of 25 kbar. The stagnated pressure (P_2) would be (from Equation 5):

$$P_2 = 6P_1 = 150 \text{ kbar}$$

The sound speed in the stagnated helium would be (from Equation 7)

$$a_2 = 9.8 \text{ km/sec}$$

As previously stated M/A was fixed at 2.0 gm/cm². Reference to Figure 11 shows that a projectile velocity of 9 km/sec (i.e., $U_p/a_2 = 0.92$) can be achieved with G/M ratio of 1. Then from Figure 11, the barrel length was determined to be

$$x_p = 1.7 \left(\frac{M}{A} \right) \frac{a_2^2}{P_2} = 22 \text{ cm}$$

The initial gas density required in the pressure tube (ρ_0) of a 25 kbar driver can be obtained from the Equation 1:

$$\rho_0 = \frac{2P_1}{(\gamma+1)D^2} = 0.026 \text{ gm/cc}$$

The required areal density of the gas (δ_g) for a given gas mass to projectile mass ratio is

$$\delta_g = \left(\frac{G}{M} \right) \delta_p = (1.0)(2.0) = 2.0 \text{ gm/cm}^2$$

The initial length of driver gas (l_g) is then

$$l_g = \frac{\delta_g}{\rho_0} = 77 \text{ cm}$$

The combined length of barrel and driver is then 99 cm, which is just within the specification of 1 meter overall length. The length could have been shortened by using a higher

pressure driver. It was felt, however, that the launching pressures should be kept as low as possible to insure the integrity of the projectiles during the launch cycle. Additionally, a pressure of 2100 PSI is required to obtain 0.026 gm/cm^3 helium density. This pressure is almost the limit that can be obtained from conventional gas bottles.

A word is in order concerning the temperature of the helium gas and the assumption of a known and constant γ . Figure 12 shows the calculated temperature and the degree of ionization at various pressures for helium gas which is first shocked in an explosive driver and then stagnated. This calculation comes from the Saha equation (Reference 16). Temperatures are shown assuming both nitromethane and PBX to be the driver explosive. At these temperatures ablation and radiation effects upon the projectile can probably be neglected. Many projectiles of plastic and metal have been launched at Physics International by helium at this temperature. Flash radiographs of the projectiles have shown no detectable ablation of the projectile due to the launching gas.

From these calculations, the basic driver and launcher parameters were defined and shown to be feasible. An explosive driver that generated a 25-kbar incident shock in helium gas was required to launch a projectile with an areal density of 2.0 gm/cm^2 . To achieve these pressures, an explosive with a detonation velocity of $8.5 \text{ cm}/\mu\text{sec}$ would be used, with the helium gas at an initial pressure of 2100 psi. The length of driver required to yield a $G/M = 1$ would be 77 cm, and the barrel for accelerating the projectile would be 22 cm in length.

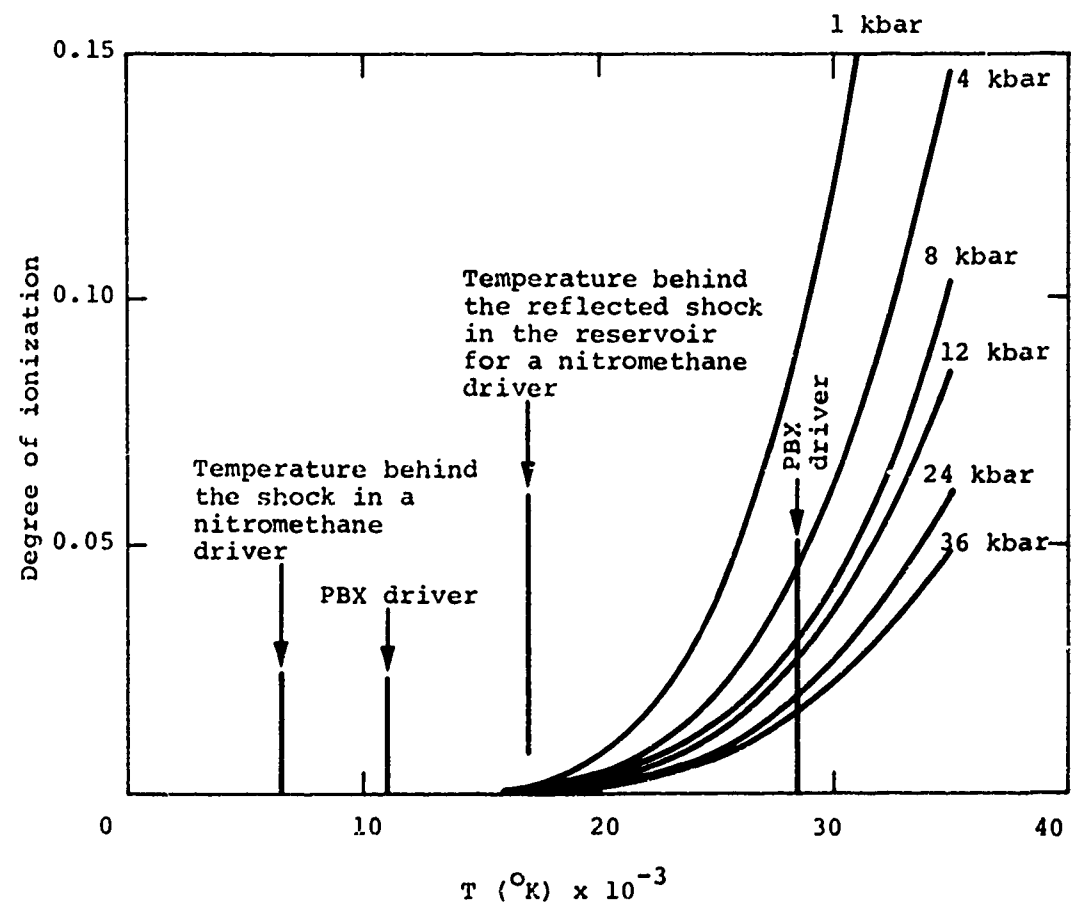


Figure 12 SAHA equation for helium.

With these basic parameters and requirements in mind, the experimental program was begun. Since a 25 kbar driver had never been built before, this was a totally new regime in which to experiment. Reference was made to previous drivers which had achieved 15-kbar incident shocks, and from the results obtained in these tests, inferences were made about the necessary features of a 25-kbar driver.

3.2 LAUNCHER DEVELOPMENT AND TESTING

Eight experiments were conducted in this program over a period of six months. Three of these experiments were attempts to launch multiple projectiles. The other shots were attempts to launch intact flat-plate projectiles to hypervelocities. These flat plate projectiles simulated possible projectile/sabot assemblies that would launch multiple projectiles from a single barrel. Each of these shots will be discussed in the following section. Table 2 is a summary of the shots conducted and the results of the experiment.

The first test conducted in the program was designed to be a checkout of the explosive driver configuration to be used in the later phases of the program. An aluminum disk, 4.14 cm in diameter and 0.74 cm thick, was used to simulate a seven-projectile sabot assembly to be utilized in later experiments. The thickness of the disk was adjusted to yield an areal density equivalent to the anticipated projectile/sabot assembly.

Since working with a liquid explosive is simpler than hand packing a plastic explosive, nitromethane was chosen for the driver explosive in the first shot. The detonation velocity

TABLE II SUMMARY

<u>Explosive Driver Characteristics</u>								
<u>Shot</u>	<u>High Explosive</u>	<u>Observed Detonation Velocity (cm/μsec)</u>	<u>Observed Shock Velocity (cm/μsec)</u>	<u>Resultant Incident Shock Pressure (kbar)</u>	<u>Driver Gas</u>	<u>Initial Pressure (atm)</u>	<u>Projectile Material</u>	<u>Number of Projectiles</u>
Blunderbuss -1	Nitromethane	0.73	0.78	11.8	Helium	150	Aluminum	1
Blunderbuss -2	Composition C-4	0.917	1.055	19.8	Helium	143	Aluminum	1
Blunderbuss -3	Composition C-4	0.926	1.10	21.5	Helium	143	Aluminum	1
Blunderbuss -4	Composition C-4	0.92	1.01	18.1	Helium	143	Nylon Aluminum Steel	2 3 2
Blunderbuss -5	Composition C-4	0.921	1.042	19.3	Helium	143	Maglith	1
Blunderbuss -6	Nitromethane	0.675	Data inconclusive	Not retrievable Designed to be 6.45	Helium	64	Maglith Aluminum Nylon	4 4 4
Blunderbuss -7	Composition C-4	0.916	1.11	21.9	Helium	143	Maglith	1
Blunderbuss -8	Composition C-4	0.907	1.01	18.2	Helium	143	Maglith Sabot also of Maglith	7

A2102

A

SUMMARY OF EXPERIMENTAL RESULTS

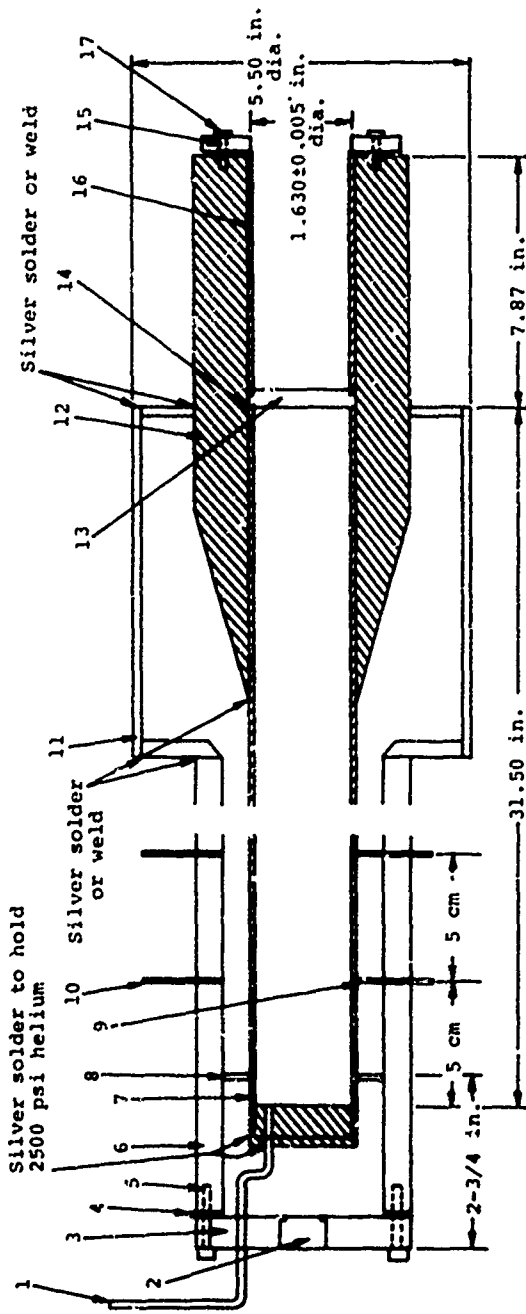
Number of Projectiles	Projectile Characteristics						Target Characteristics		
	Diam (cm)	Thickness (cm)	Mass (gm)	Barrel Length (cm)	Number of Barrels	Observed Launch Velocity (cm/sec)	Projectile Condition Down-Range	Target	Damage
1	4.14	0.74	26.9	20.0	1	0.65	Edge of projectile sheared off. Projectile warped in flash X-rays	None	N/A
1	3.84	0.74	23.1	20.1	1	Fragments 0.848 Main body 0.71	Broken up severely around edges X-rays do not clearly show main body of projectile	1 inch thick armor plate	Punched 5 cm dia hole through plate with severe rear surface spall
1	3.94	0.74	24.4	20.0	1	Fastest Fragment 0.91 Large Fragments 0.31	Completely broken up into many small fragments and some larger fragments	1 inch thick armor plate	Virtually no damage
2	1.44	1.75	3.25	18.3	2	Fastest Fragment 0.6	All projectiles broke up	1 inch thick armor plate	Virtually no damage
3	1.44	0.74	3.25	18.3	3				
2	1.44	0.257	3.26	18.3	2				
1	3.73	1.43	21.9	25.4	1	0.909	Relatively intact edges appear to have been broken	1 inch thick armor plate	Severe damage 5 cm dia hole with much rear surface spall
4	1.27	1.43	2.54	100	4	0.479 max	Intact	1½ inch thick armor plate	Al & Mg-Li-cratered plate about 1.3" dia x 0.25" deep nylon did very little damage no spall from any impact
4	1.27	0.74	2.53	100	4	0.390 max			
6	1.27	1.76	2.54	100	4	0.492 max			
1	3.66	1.43	21.1	25.4 cm plus 12.7 cm slotted barrel extension	1	0.953	Badly broken up into two large pieces and many smaller	2 one-inch thick armor plates separated by one inch	Severe damage to first plate, with large spall fragment thrown off. No damage to second plate
7	1.09 Sabot diam 3.73	1.24 Sabot thickness 1.43	1.62 each Total 21.9	25.4 cm plus 12.7 cm unslootted barrel extension	1	0.849	Totally broken up. Fragments burned up in atmosphere as they progressed down range	1 inch thick armor plate	Virtually no damage

B

required to yield a 25 kbar driver with a reasonable (2100 psi) initial gas loading pressure is 0.85 cm/ μ sec, however, nitromethane has a detonation velocity of only 0.625 cm/ μ sec. To overcome this low detonation velocity, the phenomenon of predetonation of nitromethane was to be used to increase the detonation velocity. Reference 14 discusses the mechanism of predetonation in nitromethane.

As shown in Figure 13, a heavy steel tamper was placed around the nitromethane. As the shock wave in the helium "breaks out" in front of the detonation of the nitromethane, it sends a shock wave through the undetonated nitromethane. When this shock reflects off the massive tamper, very high pressures are generated. These would hopefully predetonate the nitromethane. Past experiments conducted at PI had shown such an effect with drivers designed to yield 4 kbar shocked gas, although the induction time for this effect to occur was rather long. It was felt that since the experiment would yield at least a 15 kbar shock (based on the 0.625 cm/ μ sec detonation velocity of nitromethane), the induction time required for the predetonation of the explosive would be considerably reduced.

Analysis of the shot data shows that the detonation velocity of the nitromethane did, in fact, begin to accelerate; however, adverse effects from gas loss caused by incomplete closure of the pressure tube prevented the explosive pre-initiation from accelerating to the detonation velocity required. Figure 14 is a plot of the detonation and helium gas shock x-t history. Ion pins and cap pins were used in the



- 1 1/16 in. stainless steel tubing epoxy to lucite and plate
- 2 Detonator holder assembly
- 3 Lucite and plate
- 4 Neoprene gasket
- 5 Drill and tap (6) Places 8-32
- 6 Steel tangent 3-1/2 in. o.d.; 2-5/8 in. i.d.
- 7 Steel pressure tube; 1-3/4 in. o.d.; 0.063 in. wall
- 8 Steel, 1/16 in., support spider
- 9 Cap F.t., rateated every 5 cm
- 10 Ion pin, repeated every 5 cm
- 11 5.50 in. o.d., 0.120 in. wall carbon steel tubing
- 12 2.50 in. o.d., 0.875 in. wall carbon steel tubing
- 13 Aluminum projectile, press fit into barrel insert
- 14 1/32 in. thick neoprene gasket
- 15 Steel barrel insert retained
- 16 Barrel insert; 1-1/4 in. dia. 0.083 in. wall steel tubing lubricated with standard grease; o.d. only
- 17 Drill and tap for 10-24, dia. 1/8, places on a 2.50 in. dia. bolt circle

Figure 13 Configuration of the first experiment.

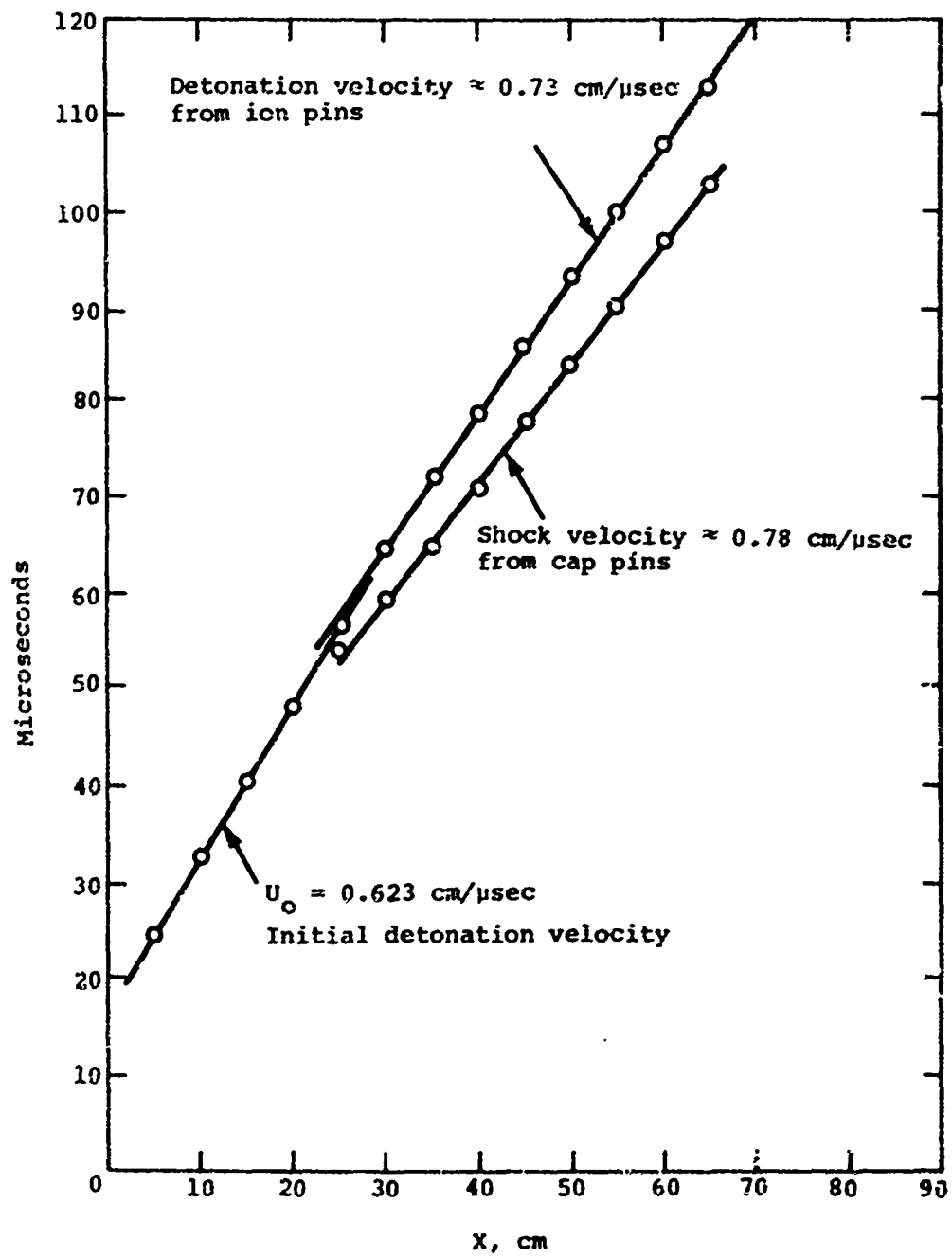


Figure 14 Blunderbuss-1 x-t plot.

diagnostics to observe the detonation and helium shock trajectories. Ion pins are simple coaxial conductors with a solid sheath that shorts out when the conductive ionized detonation wave passes over them. Cap pins, on the other hand, are basically the same as ion pins with the addition of a metal cap over the end of the conductor which is sensitive to pressure and shorts out the coaxial conductor with the application of pressure. A simple resistor-capacitor discharge circuit operating at 200 volts assures high signal levels from the pin to the oscilloscope. Both ion and cap pins were located every 5 cm along the length of the pressure tube. Cap pins are passed through the tamper and explosive and are in direct physical contact with the pressure tube. Ion pins are passed through the tamper and are in contact with the explosive (see Figure 15). Since the shock wave does not precede the detonation wave until breakout, both pins react to the detonation wave up to that point. The shock velocity achieved in this experiment was 0.78 cm/ μ sec, which yielded a 12-kbar driver. The flat disk projectile was launched relatively intact to a velocity of 0.62 cm/ μ sec. This velocity is close to the ideal velocity that would be achieved for a 12 kbar reservoir pressure, based on Seigel's work. The fact that the projectile was launched almost intact (a thin rim section of the disk was sheared and was launched to slightly higher velocities) under a 12-kbar reservoir pressure was encouraging and pointed out that the stresses generated by the launch cycle were not excessive in terms of launching an intact but severely distorted projectile. Figure 16 is a flash radiograph showing the projectile in flight.

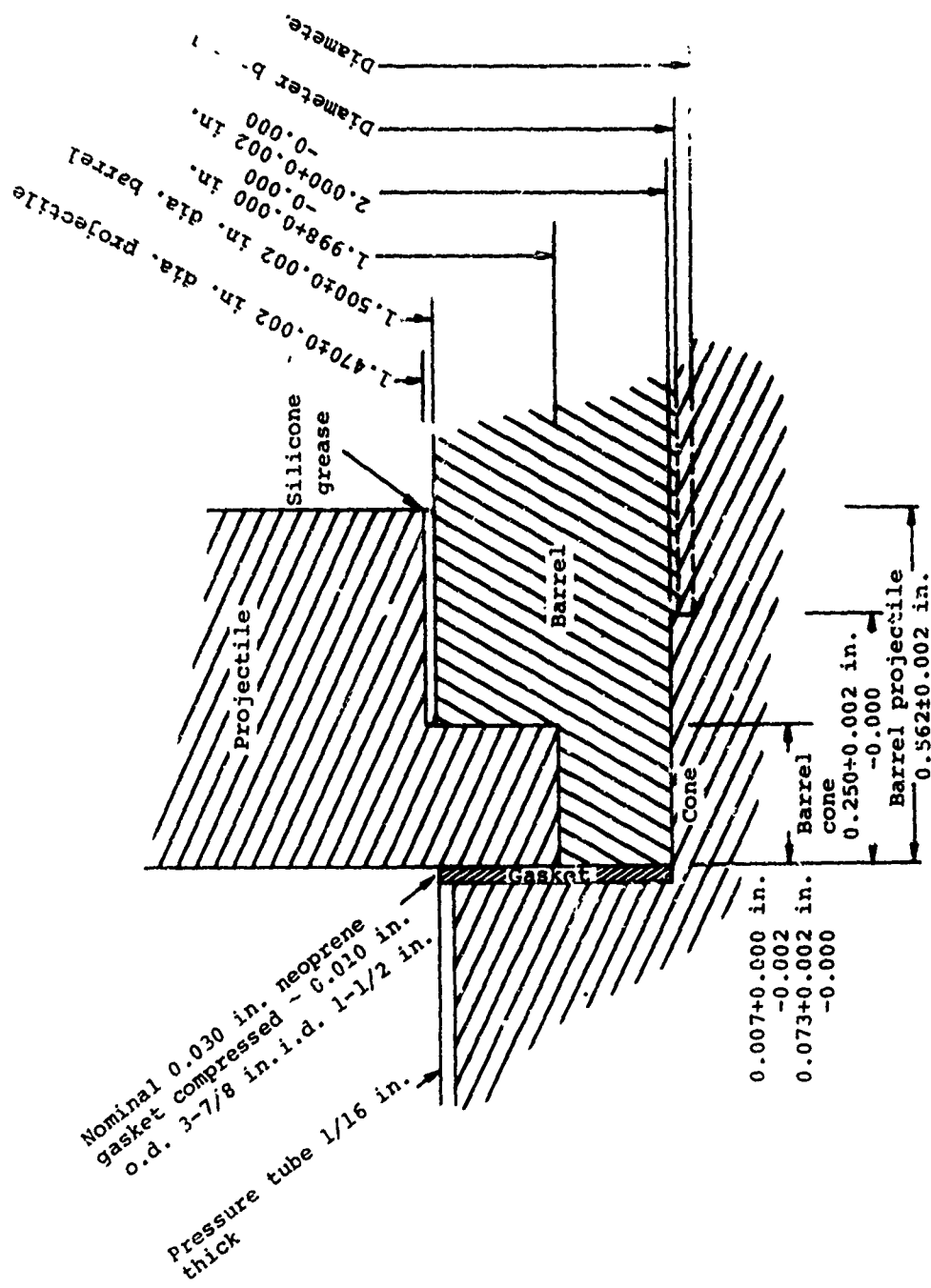


Figure 15 MEROC Blunderbuss-5 detail.

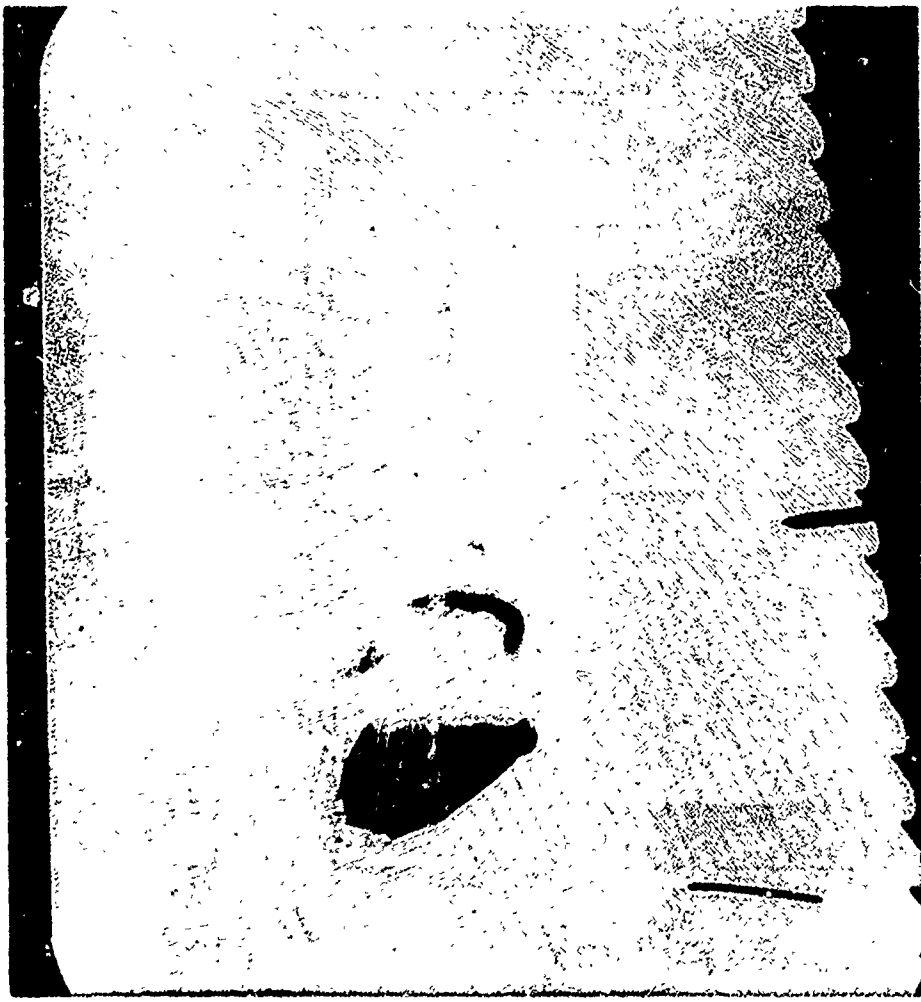


Figure 16 Radiograph of projectile in flight from Blunderbuss-1.

Blunderbuss-1 was unsuccessful, partially because the predetonation phenomenon was not as pronounced as was hoped, and partially because the collapse of the explosive driver pressure tube was incomplete. Design review of the driver indicated that the pressure tube-to-explosive mass ratio was on the borderline of full collapse, and, from the results of the test, clearly on the wrong side of the line. To aid in the further design of the explosive driver, numerous hydrodynamic computer code calculations were conducted. The results of these calculations will be discussed in Section 4. The most important reason for conducting these calculations was to aid in the prediction of the pressure tube-to-explosive mass ratio that would insure complete collapse of the driver pressure tube.

Since it appeared that even under very high pressures, the predetonation of the nitromethane explosive would not increase the detonation velocity sufficiently to yield a 25-kbar driver, it was decided that an explosive of a higher detonation velocity should be utilized. Various explosives were considered, and Composition C-4 was selected as the candidate explosive.

The second shot of the program was again a driver checkout shot. Figure 17 is a drawing of the shot configuration. The driver was designed to yield a 25-kbar incident shock in the helium gas. The internal pressure of the helium prior to the shot was 2100 psi, which, when coupled with a detonation velocity of 0.85 cm/usec, would yield a 25 kbar shock in the gas. As in the first shot, the projectile to be launched was an aluminum disk 0.74 cm thick by 3.84 cm in diameter.

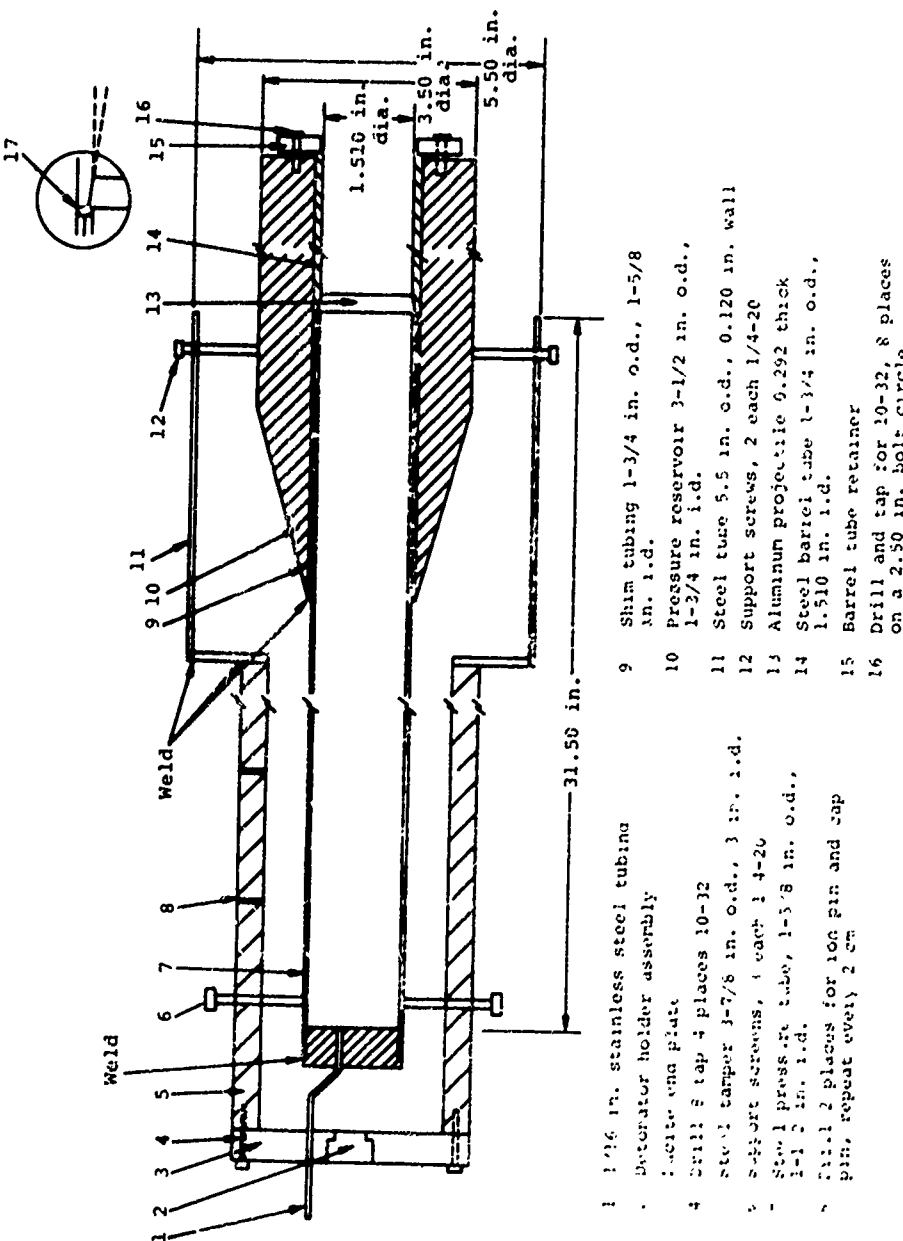


Figure 17 Configuration of the second experiment.

In the first shot the edge of the projectile sheared off, leading to partial breakup of the disk-like projectile, even though the reservoir pressures obtained were significantly less than the pressures required to achieve 10 km/sec muzzle velocity. To eliminate this edge-shearing phenomenon in the second shot, the disk-like projectile was designed as a truncated cone, with the edges tapered at an 8 degree angle. This taper would seat against a similar taper in the barrel liner and would hold against the initial pressure of 2100 psi.

Previous experience using Composition C-4 in explosive driver systems has shown a tendency for the detonation velocity of the C-4 to increase. This effect occurs due to precompression of the explosive by the shock in the helium gas that out-runs the detonation in the explosive. Thus, while the standard detonation velocity of C-4 is 0.804 cm/ μ sec, it was felt that the increase in detonation velocity due to precompression would approach the 0.85 cm/ μ sec required to achieve a 25 kbar driver. To insure that the pressure tube would collapse, efficiencies and C/M ratios typical of previously tested high pressure drivers were used in this new driver system. Additionally, the configuration of the driver system was checked out on the 1-1/2 D ELK code that was assembled to assist in the design of the drivers for this program. The results of this calculation showed that the driver pressure tube would indeed collapse completely.

Examination of the results of this shot show some very interesting phenomena. Initially, the detonation velocity of the C-4 explosive was the expected 0.804 cm/ μ sec. However, after breakout of the helium shock ahead of the detonation

front, the detonation velocity of the C-4 increased to 0.914 cm/ μ sec due to the precompression of the high explosive. Figure 18 is an x-t plot of the driver for this shot. This increase in detonation velocity was far above the expected increase and added to the efficiency of the driver system. However, gas losses due to bubble entrapment at the closure point of the collapsing pressure tube led to a final shock velocity of 1.055 cm/ μ sec, or an incident shock pressure of 19.8 kbar. Figure 19 shows the collapsed pressure tube, partially sectioned, releasing areas of gas bubble entrapment in the collapsed tube. The bubble entrapment is a manifestation of the growth of boundary layer gases in the pressure tube.

The projectile was launched to a velocity of approximately 7 km/sec; however, it was not an intact projectile. Examination of the flash radiographs showed that the edge of the projectile had broken off into significant pieces and that various small fragments of the broken pieces were accelerated to a velocity of 8.5 km/sec. In the radiographs the projectile appeared to be tumbling; however, a target plate of 1-inch-thick armor plate showed a very neat 1.5-inch-diameter hole punched through the center, indicating that the projectile impacted the plate normal to its line of flight (Figure 20).

From the results of this shot it was concluded that a workable 20- to 25-kbar driver had been designed and that this design would be utilized in future experiments. Although the ultimate incident shock obtained by the driver tested achieved a shock of only 20 kbar, the effort required to eliminate the gas bubble entrapment and increase the pressure to

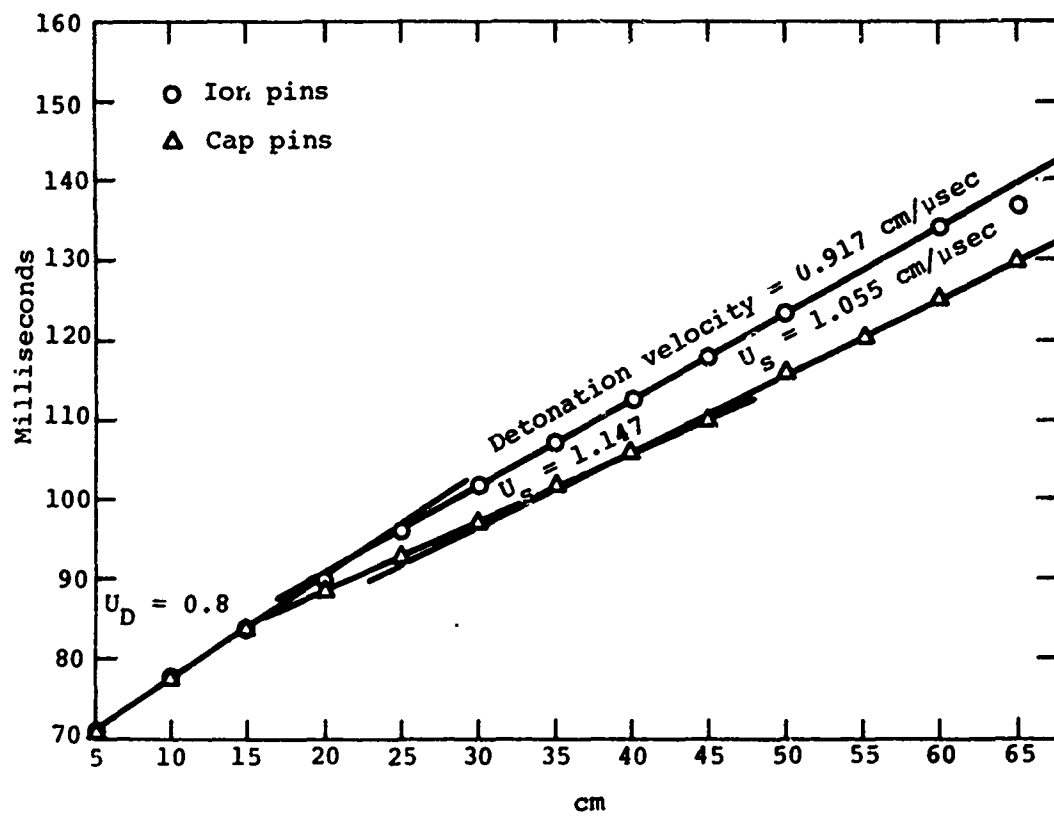
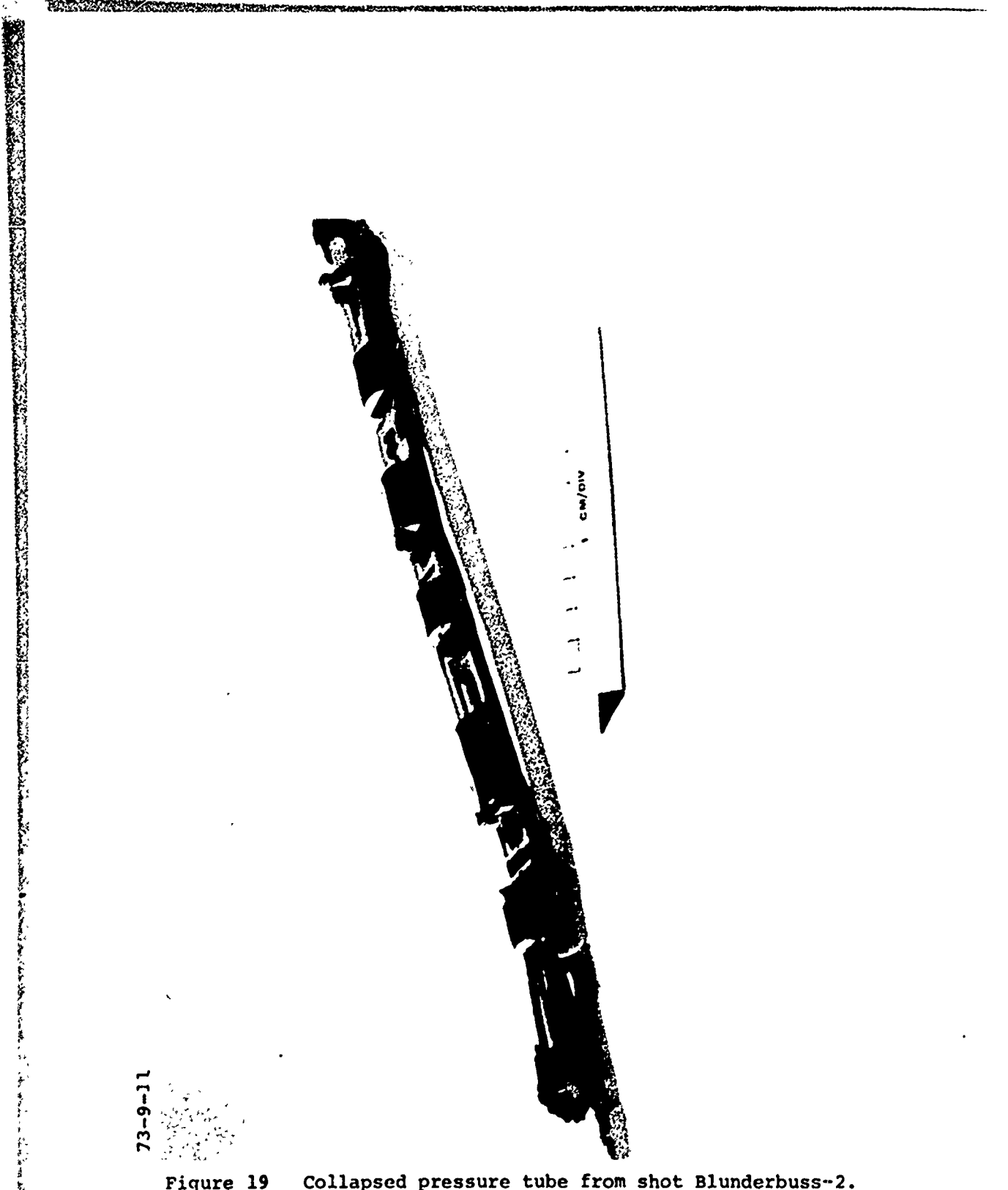


Figure 18 Blunderbuss-2 x-t plot.



73-9-11

A2100

Figure 19 Collapsed pressure tube from shot Blunderbuss-2.
Note entrapped gas bubbles in sectional portions of collapsed tube and "blow-out" holes from bubbles to outside.

73-9-12



Figure 20a Front view of 1 inch thick armor target after impact.

73-9-9

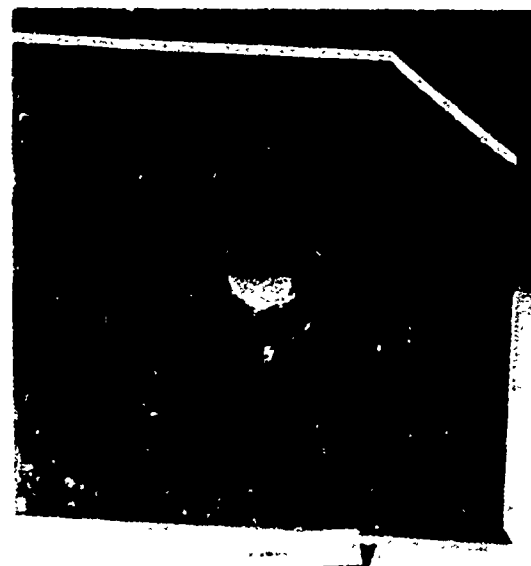


Figure 20b Rear view of 1 inch thick armor target after impact.
Note large spall area compared to penetration hole.

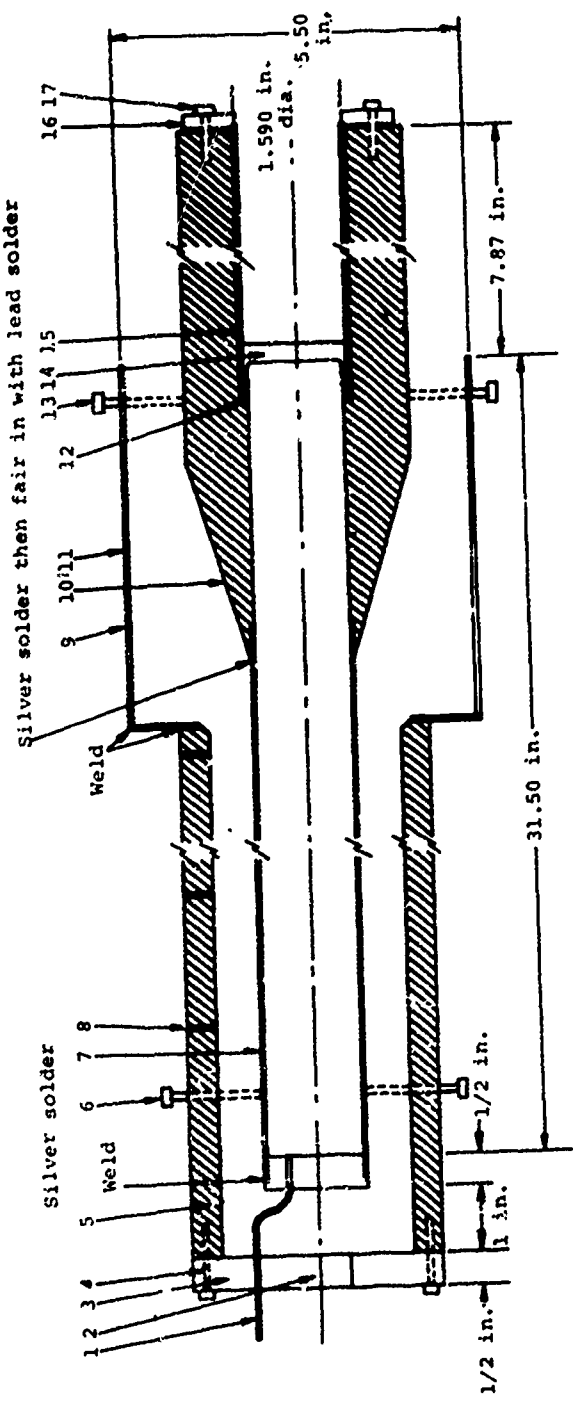
A2148

25 kbar was not deemed necessary. If required, a small extension of the barrel length would compensate for the loss in reservoir pressure.

Evidence from the previous shot indicated that the edge of the projectile was breaking up from shear stress induced when the projectile began acceleration. In the previous shot the projectile was held in place by a taper designed to fail only in shear. It was felt that a new design that allowed the projectile to feel very little shear forces at the beginning of the acceleration would increase the probability of launching an intact projectile.

The third shot of the experimental series utilized the same explosive driver as that developed for the second shot, Blunderbuss-2. The design of the projectile was modified so that a thin cylindrical section of the rear of the projectile would fail in tension rather than allowing the edge of the projectile, through its support, to fail in shear. Figure 21 is a drawing of the shot configuration. In this configuration the edges of the projectile would not see shear forces induced by the breaking up of the projectile support. It was hoped that this design would yield an intact projectile at the required velocity.

The explosive driver of Blunderbuss-3 performed consistently with the previous driver performance, yielding an incident shock of 21.5 kbar. However, the aluminum disk-like projectile was completely broken up. Very small fragments of the projectile were accelerated to a velocity of 9.05 km/sec.



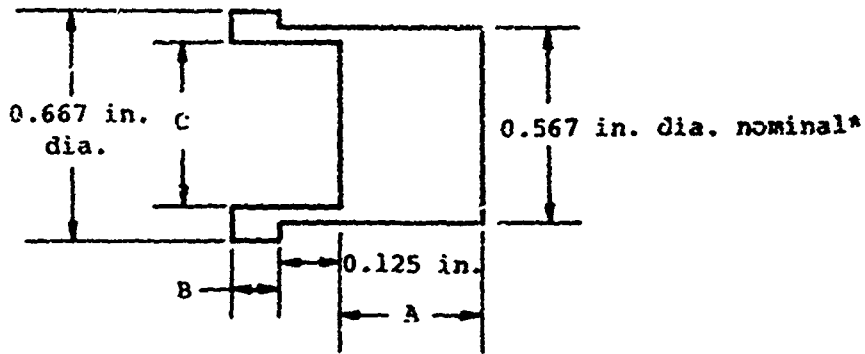
- 1 1/16 in. stainless steel tubing
- 2 Detonator holder assembly
- 3 Lucite end plate
- 4 Drill and tap 3 places 10-32
- 5 Steel tubing 3-7/8 in. o.d., 3 in. i.d. H.E. tamper
- 6 Support screws 3 each 1/4-20
- 7 Steel tubing 1-3/8 in. o.d., 1-1/2 in. i.d. driver pressure tube
- 8 Drill 2 places for ion pin and cap pin, repeat every 5 cm
- 9 Drill 1 places for ion pin as in 8
- 10 Steel rod 3-1/2 in. o.d. typer and reservoir section
- 11 Steel tubing 5-1/2 in. o.d. 0.120 in. wall
- 12 Neoprene gasket
- 13 Support screws 3 each 1/4-20
- 14 Aluminum Projectile
- 15 Steel tubing 1-3/4 in. o.d. barrel liner
- 16 Barrel liner retainer
- 17 Drill .03 d tap 8 Places for 10-32 on a 2.50 in. B.C.

Figure 21 Configuration of third experiment.

Immediately following Blunderbuss-3, Blunderbuss-4 was fired which was designed to launch seven projectiles to 10 km/sec. This shot utilized projectiles of aluminum, nylon, and steel. The configuration of these projectiles was the same as that in the previous shot, i.e., they were designed to fail in tension along a cylindrical parting plane behind the projectile itself (Figure 22). This shot utilized seven individual barrels to launch the projectiles, each projectile being approximately 0.5 inch in diameter (Figure 23). To insure equal acceleration characteristics, the areal density of all seven projectiles was maintained at 2.0 gm/cm^2 .

Diagnostics on this shot showed that the driver again performed as expected. Once more the incident pressure jump across the shock wave in the helium gas was approximately 20 kbar. Flash radiographs on this shot failed to operate correctly, so that no usable data was gathered from these diagnostics. A target of 1-inch-thick armor plate was used as a witness plate for the shot, however, and it showed that all seven projectiles had broken up before impacting the plate. Velocity achieved by the projectile fragments was a maximum of 6.05 km/sec.

Following the unsuccessful Blunderbuss-4, an in-house review of the technical status of the program was conducted. Experimental evidence had shown that the explosive driver portion of the launcher system was working adequately and would satisfy the requirements of the program. However, no shot was completely successful in launching an intact projectile to the required velocities. In closely examining the conditions of projectile launch, a theory that explains the projectile breakup in the early stages of launch was developed.



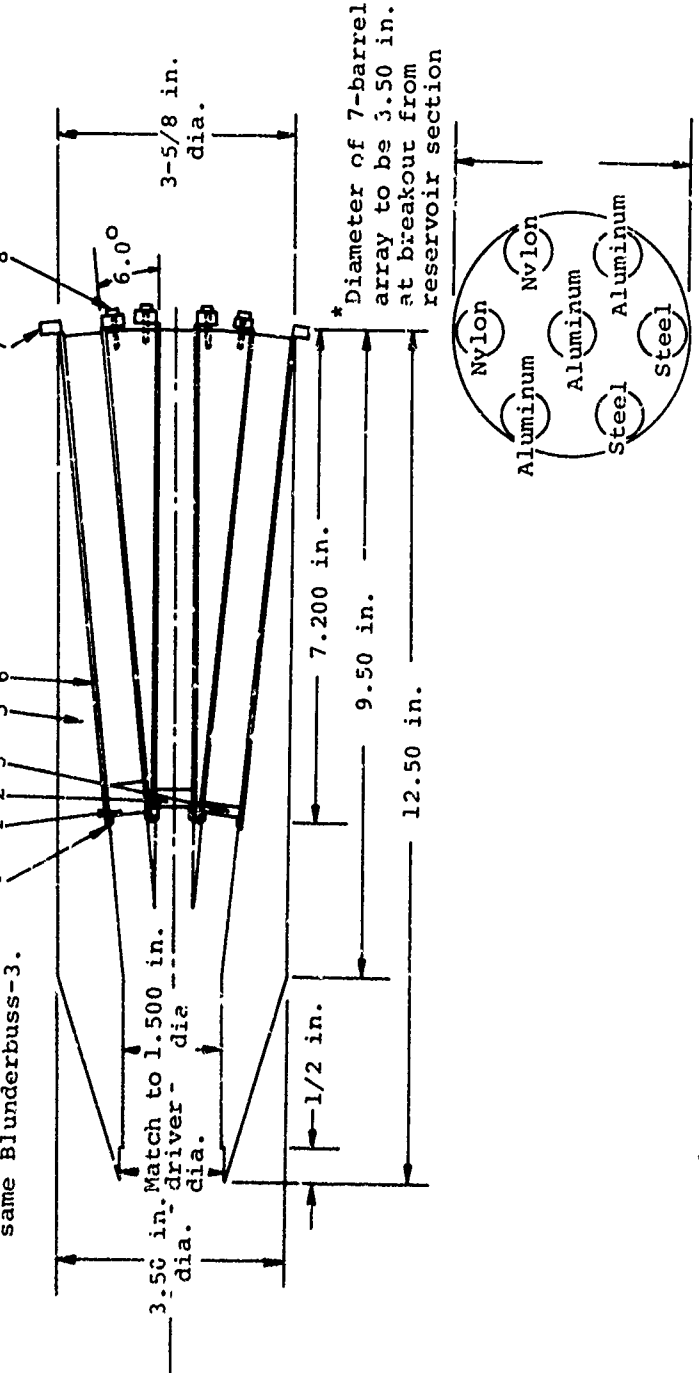
*Fit to individual barrel

Material	A	B	C	Number required
Nylon	0.689	0.130	0.491	2
Aluminum	0.291	0.032	0.550	3
Steel	0.101	0.032	0.546	2

All dimensions are in inches

Figure 22 Blunderbuss-4--projectile design.

Note: Driver and tamper assembly to be the same Blunderbus-3.



- 1 Nylon projectile
- 2 Aluminum projectile
- 3 Steel projectile
- 4 Neoprene gasket
- 5 Steel rod, 3-5/8 in. o.d. reservoir section
- 6 Steel tubing; 0.567 in. i.d., 0.667 in. o.d. barrel liner
- 7 Barrel liner retainer
- 8 Drill and tap 5 places per retainer for 10-32

Figure 23 Configuration of fourth experiment.

When the shock wave in the helium gas generated by the explosive driver stagnates against the rear of the projectile, it experiences a six-fold increase in pressure (see Section 2.3, Equation 5). Thus, with an explosive driver that yields an incident shock of 20 kbar, the reflected (or stagnation) pressure would be on the order of 120 kbar. At early stages of the launch cycle, therefore, the projectile is subjected to a compressive stress of approximately 120 kbar. This is well above the threshold for plastic flow, and the projectile would attempt to expand radially to relieve the axial compressive stresses. In a tight fitting barrel, which all of the shots up to this point had had, the edges of the projectile would be expected to push outward against the barrel. In hydrodynamic flow conditions, the difference between radial and axial stress (i.e., the deviatoric stress) would be expected to be on the order of 10 kbar or less (for aluminum). Thus, the projectile would be subjected to 120 kbar of axial compressive stress attempting to accelerate the projectile and approximately 110 kbar of radial stress resulting in very large drag forces at the periphery of the projectile. The shear stresses that result from interaction of these forces is extreme, resulting in breakup of the projectile. To confirm or modify this theory, a two-dimensional computer analysis of the launch cycle conditions was begun. The results of this analysis are discussed in Section 4.

The fifth shot of the experimental program, Blunderbuss-5, was designed to prevent the induced drag forces and subsequent shear stresses from affecting the initial launch conditions of the projectile. To accomplish this the projectile diameter was made undersize with respect to the bore of the barrel, and a

layer (approximately 0.015 inch) of Dow-Corning silicone grease was introduced between the projectile and the barrel. This layer of silicone grease would place a strengthless, low-friction material between the projectile and the barrel which hopefully would prevent the large induced shear forces from occurring.

Additional changes in the configuration of the launcher were as follows. Almost all previous experience with explosive driver accelerators has been in launching projectiles of magnesium/lithium alloy. Since very little experimental data has been developed in launching aluminum projectiles with explosive driver technology, it was decided that a return to Maglith was in order. Also, the thickness of the barrel was increased to the point that there would be very little chance that premature barrel failure would result in the lowering of the launch velocity through abnormal gas losses. Figure 15 is a drawing of the configuration of Blunderbuss-5. Figure 24 is a Polaroid photograph of the shot just prior to firing.

This fifth shot was judged to be quite successful. The explosive driver worked as expected and yielded an incident shock of 19.3 kbar. Projectile launch velocity was increased to 9.1 km/sec. Figure 25 is a flash radiograph of the projectile in flight at the velocity of 9.1 km/sec. It is obvious that the projectile is somewhat broken up; however, the thickness of the launched projectile is equivalent to the original thickness of the projectile. Since the velocity achieved by the projectile is quite high, it is unlikely that the projectile broke up during the launch cycle.

Figure 24 Blunderbuss-5 just prior to firing. White ring near rear of barrel section is C-4 explosive.



A2147



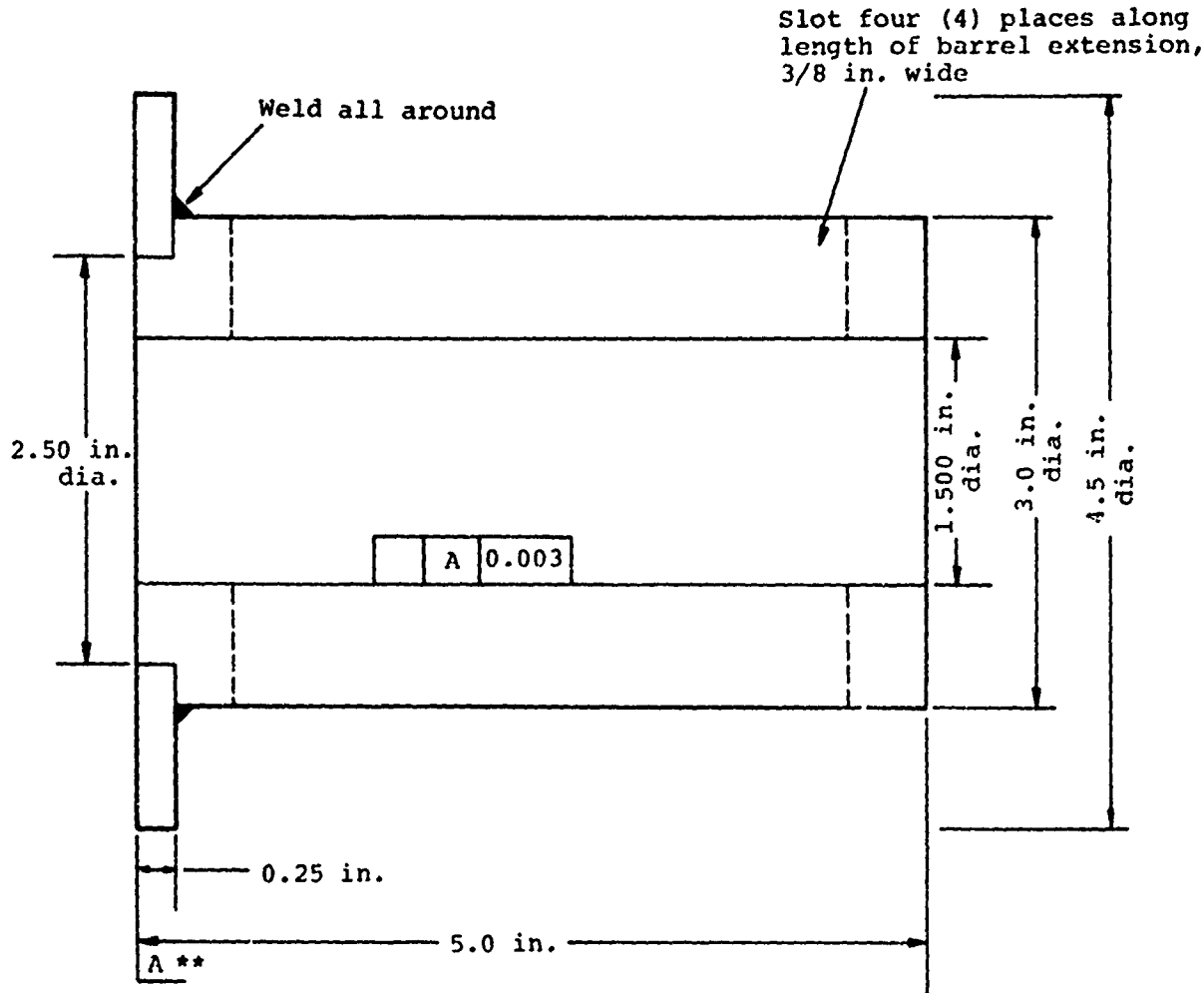
Figure 25 Projectile from Blunderbuss-5 in flight.

A2146

It was theorized that since the projectile could not have broken up in the barrel and still have achieved the high velocity at launch, breakup must have occurred after the projectile exited the barrel. Since the pressure on the rear of the projectile is not completely relieved by the time launch occurs, compressive stresses on the projectile could be severe enough to cause projectile breakup through the sudden release of the radial constraint of the projectile. Since the flash radiograph of Blunderbuss-5 shows that the thickness of the projectile corresponds to the original thickness of the projectile, yet the diameter of the projectile is reduced and non-symmetric, it appears that radial spall was the probable mechanism of projectile breakup after launch.

In a further attempt to launch an intact projectile, the sixth shot of the series (Blunderbuss-7) utilized a barrel extension to relieve the gas pressure behind the projectile, yet maintain radial constraint on the projectile itself. Figure 26 is a drawing of the barrel extension that was inset and welded to the basic launcher configuration of Blunderbuss-5. For this shot the silicone grease of Blunderbuss-5 was replaced by a Teflon sleeve around the Maglith projectile. Figure 27 is a drawing of the projectile assembly.

This shot attained marginal success. Driver performance was once more consistent with previous tests. The addition of the barrel extension and the Teflon sleeve did increase the launch velocity of the projectile to 9.6 km/sec. However, the original disk-like projectile was broken into three smaller fragments, and, from the report of the flash radiographs (Figure 28), the sum of the parts did not equal the original whole.



* Match to diameter of launcher barrel
** Machine surface -A- to fit against launcher barrel

Figure 26 Blunderbuss-7--barrel extender.

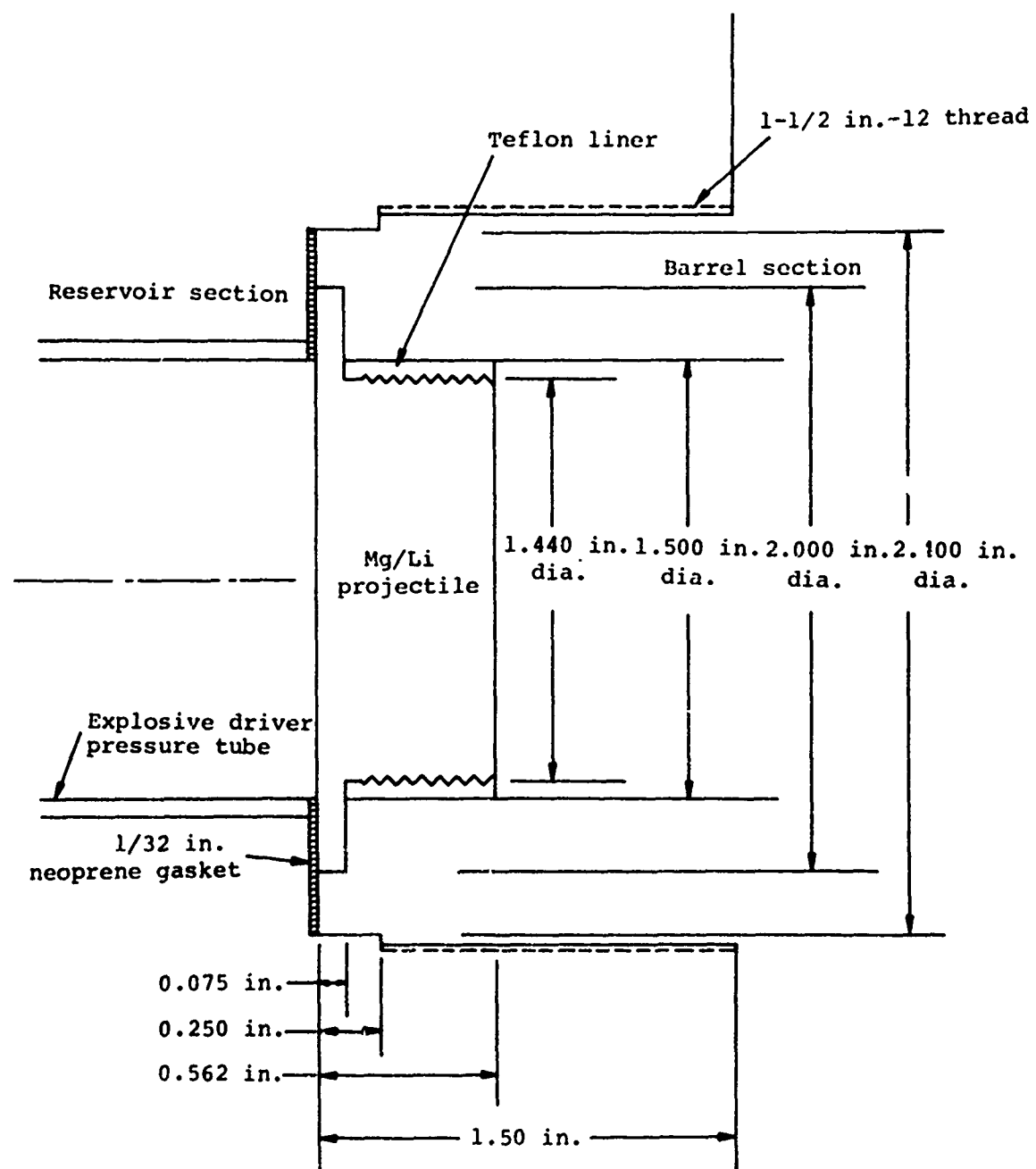


Figure 27 Blunderbuss-7 detail.

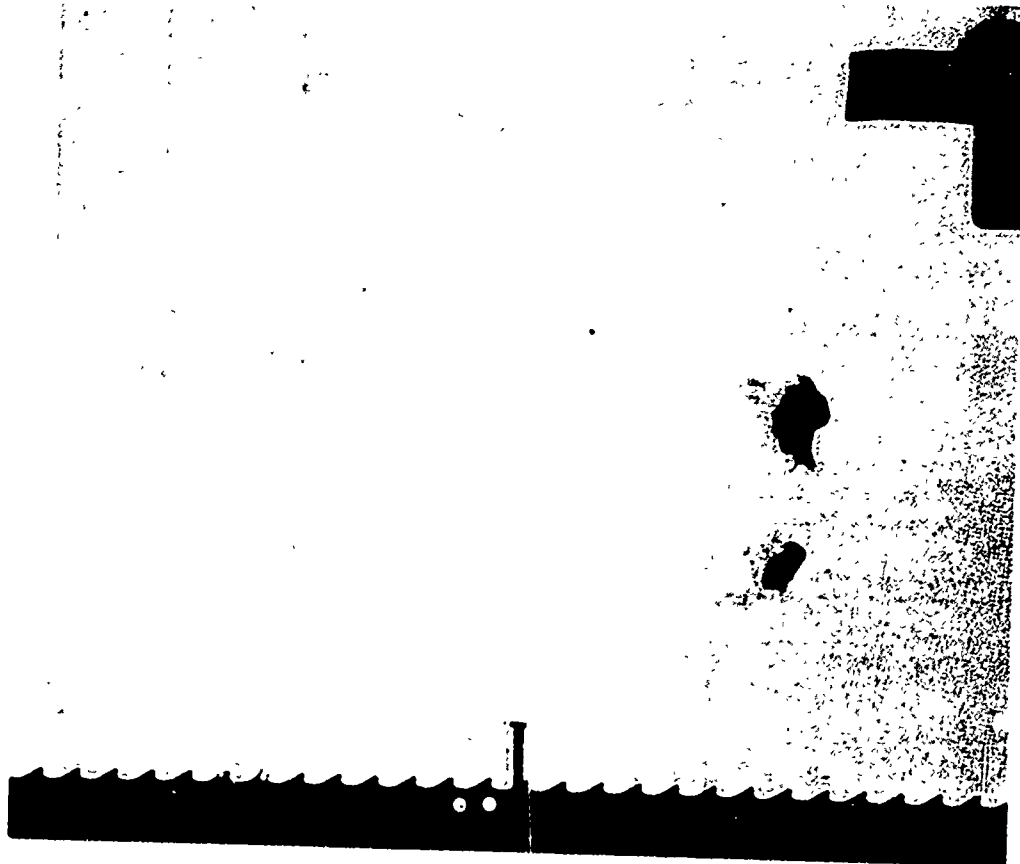


Figure 28 Flash radiograph of projectile from Blunderbuss-7
in flight.

A2145

Some calculational effort was expended at this point to characterize the launch process and to examine the collapse of the reservoir. These calculations matched with observed experimental results. Indications from these computations were that the projectile is still under pressures of about 35 kbar at the time that it exits the barrel. It appears that the high pressures on the rear of the projectile were great enough to cause the projectile to extrude into the slots cut into the barrel extension to vent the gases. When the now cross-shaped projectile comes to the end of the barrel extension slots, with part of the projectile extruded into the slots, the resulting impact forces cause the destruction of the projectile.

One other experiment was performed during this time frame. An attempt was made to launch twelve projectiles of three different materials to 10 km/sec from a 6 kbar explosive driver launcher system. Unfortunately, the explosive driver section of the launcher failed to collapse completely, and thus, the pressures required to reach 10 km/sec were not obtained. The average velocity of the projectiles was on the order of 4.5 km/sec. From the review of the shot data it appears that the charge-to-mass ratio of the high explosive to the driver pressure tube was below the minimum required to fully collapse the tube against the 6 kbar shock in the helium. (Note that this was a totally different driver and launcher design than the now standard 1 meter, Composition C-4 launcher.) The design of the shot had been checked by the use of the 1-1/2 dimension computer code and had been predicted to close the pressure tube. The closure predicted, however, was marginal. In future designs it is apparent that a greater margin of collapse energy must be used.

Blunderbuss-8, the final shot of the experimental program, was an attempt to launch seven individual projectiles contained in a single sabot utilizing a single barrel launcher. This shot was designed to show that multiple projectiles could be launched intact from a 20 kbar driver system. The sabot, as shown in Figure 29, was designed to take advantage of the possible radial breakup of the projectile as it exits the barrel. If the mechanism of projectile breakup in the two previous shots was radial spall caused by the sudden unloading of the projectile as it left the barrel, this same mechanism would cause the sabot to break up, yet it might leave the individual projectiles intact. Additionally, since the breakup was expected to occur radially, this would aid in the dispersion of the projectiles.

Figure 30 is a drawing of the shot configuration. A barrel extension was added to increase the length of the barrel by 10 cm, and the projectile was surrounded by a layer of silicone grease, as in Blunderbuss-5. There were no slots in the barrel extension for this shot, its function being to increase the muzzle velocity of the projectile. The projectile/sabot assembly was similar to the previous shots in that it was a disk-like package containing seven individual projectiles. Figure 31 illustrates the sabot and projectile configuration.

This experimental shot was essentially a calculated risk. It was felt that the causes leading to projectile breakup were known. Only one shot remained in which to launch multiple projectiles and exhibit total proof of concept, and it was decided that a multiple projectile launch should be attempted. The shot, however, did not meet expectations. The explosive driver system worked as expected; however, the projectile/sabot package was totally broken up, and a velocity of only 8.4 km/sec was obtained. Projectile and sabot fragments shown in the flash radiographs were tenuous at best and are not shown in this report due to the limited definition obtainable in half-tone reproductions.

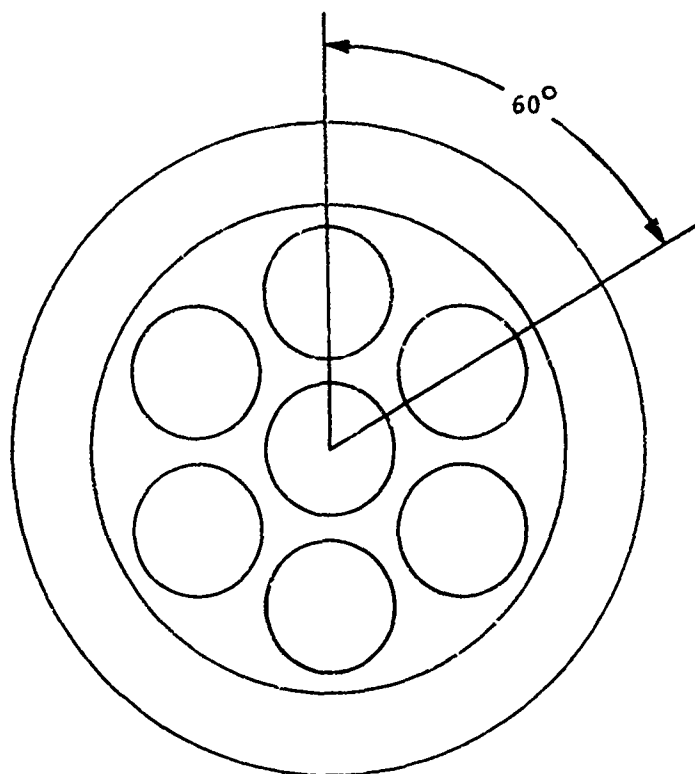
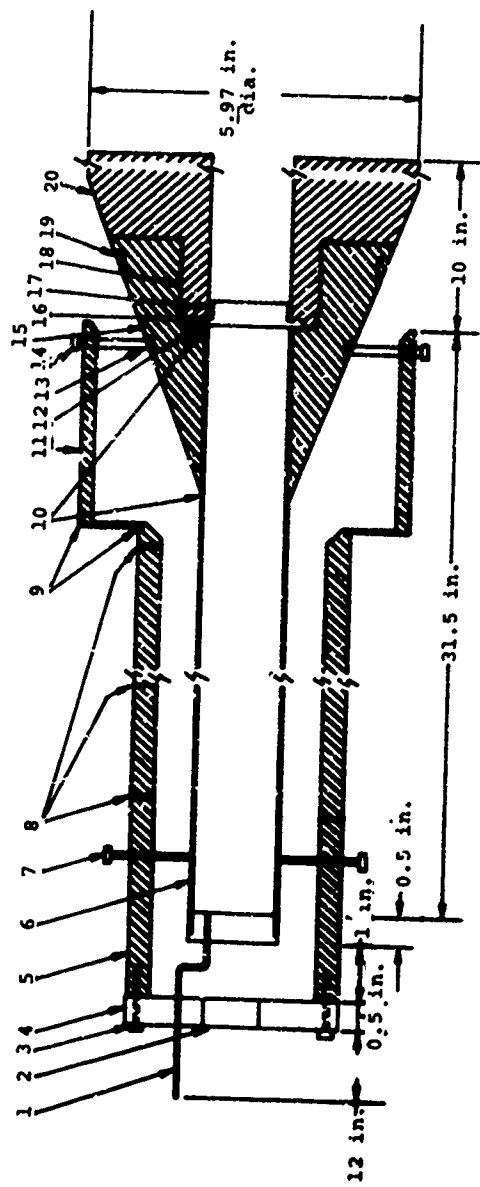


Figure 29 Sabot for Blunderbuss-8.



1. 1/16 in. stainless steel tubing
2. Detonator holder assembly
3. Drill and tap 3 pieces, 10-32
4. Lucite and plate
5. Steel tubing; 3-7/8 in. o.d., 3 in. i.d.
6. Steel tubing; 1-5/8 in. o.d., 1-1/2 in. i.d.
7. Support screws; 3 each, 1/4-20
8. Drill two places for pins; repeat every 5 cm, 28 pins total, 14 CCP pins and 14 ion pins
9. Weld
10. Silver solder (then fair with lead solder on tip)
11. Steel tubing; 6 in. o.d., 5-1/2 in. i.d.
12. Neoprene gasket
13. Spot face 3 places for 1/4-20 screw
14. Support screws; 3 each, 1/4-20
15. Taper section machine from solid steel round
16. Maglith projectile
17. Silicon grease 0.015 in. thick between projectile and barrel do not extend past end of projectile
18. Threads; 2-5 in-12 lubricate with silicone grease, 1/8 in. thread relief
19. Flats for assembly of barrel does not extend all the way around barrel
20. Barrel section machined from solid steel round (hot rolled), 6 in. o.d.

Figure 30 MERDC launch cycle study--Blunderbuss-8.

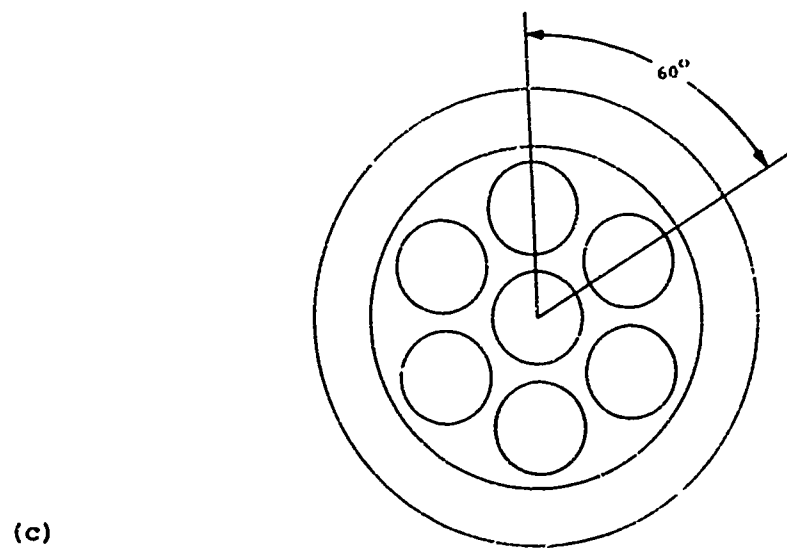
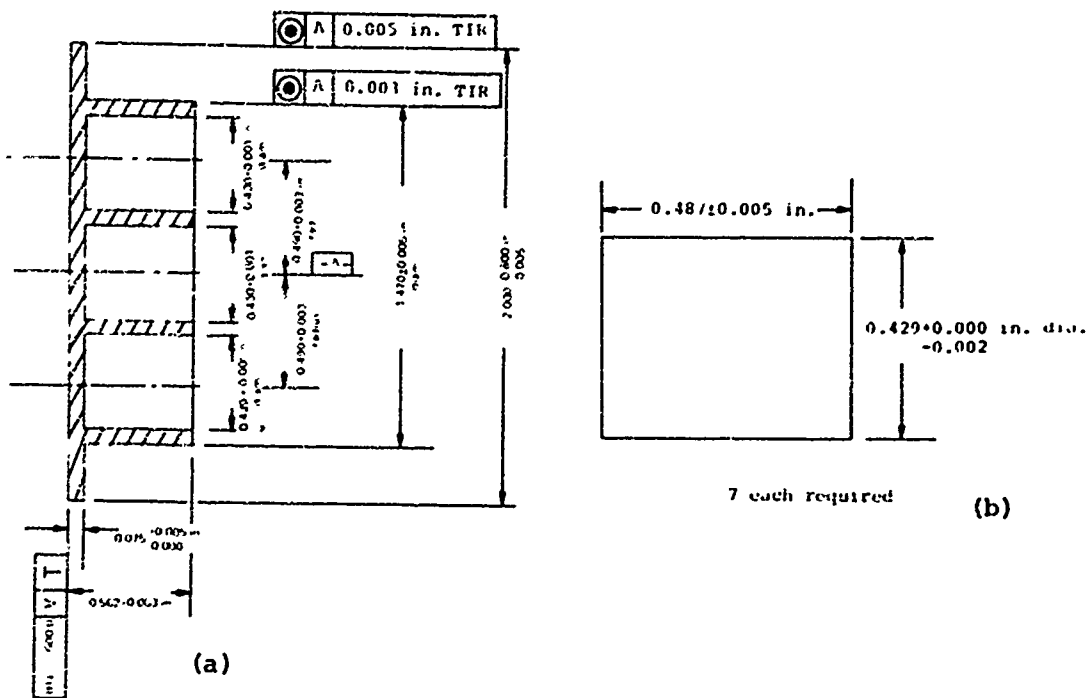


Figure 31 (a) Sabot for Blunderbuss-8.
 (b) Projectiles for Blunderbuss-8.
 (c) Sabot for Blunderbuss-8.

SECTION 4

COMPUTATIONAL SUPPORT

4.1 INTRODUCTION

The computational effort associated with the program was directed towards two basic objectives. The first objective was to provide data to assist in designing and analyzing the performance of the explosive driver used as the energy source for launching the projectiles. This objective was achieved by performing a series of one and one-half dimensional (one-dimensional Moving Wall Flume, see Appendix B for a description of the flume option) calculations. The second objective of the computational effort was to perform a calculation of the interactions at the driver/barrel, barrel/projectile, and driver/projectile interfaces, and the response of the projectile to the induced stresses. A two-dimensional calculation of the early stages of the launch cycle was performed to obtain this information.

4.2 MATERIAL MODELS AND EQUATIONS OF STATE

The yield models and equations of state used to describe the helium driver gas, the C-4 explosive, and the steel of the pressure tube, tamper, and barrel were identical for all the calculations. The two-dimensional launch cycle calculation also contained a magnesium-lithium (Maglith) projectile. The equation-of-state models used for these materials in the computational analyses are summarized in Table III.

TABLE III
SUMMARY OF EQUATIONS OF STATE AND YIELD MODELS

$$\text{Equation of State: } P = a_0 + a_1 u + a_2 u^2 + a_3 u^3 + [b_0 + b_1] E$$

$$\text{where } u = \frac{\rho}{\rho_0} - 1, \quad \rho = \text{density}$$

Yield Model: Von-Mises (constant yield stress = Y)

	a_0 (Mbar)	a_1 (Mbar)	a_2 (Mbar)	a_3 (Mbar)	b_0	b_1	E_0 10 ¹² ergs/gm	ρ_0 gm/cm ³	Y (Mbar)	G (Shear Modulus, Mbar)
Steel (liner)	0	1.69	0	0	0	0	7.85	0.003	0.822	
Steel (tamper and barrel)	0.0015	1.69	0	0	0	0	7.85	0.003	0.822	
C-4 explosive	0	0.028	0.407	-0.36	1.7	1.7	0.114	1.59	0	0
Magnesium- lithium	0	0.217	0.366	-0.0079	0	0	0	1.38	0.0012	0.181

4.3 EXPLOSIVE DRIVER CALCULATION

In general the principal information to be obtained from an explosive driver calculation is whether or not the liner collapses, the velocity of the point of collapse, the peak pressure at the shock front in the driver gas, and the velocity of this shock front. This information may be computed most efficiently using a one-dimensional, explicit, finite-difference continuum mechanics code with a Moving Wall Flume (variable area duct) capability. Until recently, PI's explosive driver calculations of this type were performed using a one-dimensional Lagrangian code. Experience proved this technique useful but indicated that a more precise solution of the state of the driver gas could be achieved if the gas were described as an Eulerian fluid retaining the Lagrangian description of the pressure tube, explosive, etc. A one-dimensional Eulerian code, PISCES 1DE, was available (Appendix A), and the PISCES 1DE and PISCES 1DL (Appendix B) codes were dynamically coupled in a manner similar to that employed in Physics International's two-dimensional, coupled Eulerian-Lagrangian code, ELK. The code resulting from the coupling of the PISCES 1DE and 1DL codes was used to perform the driver calculations for this program. In these calculations the driver gas is treated in an Eulerian frame of reference while the pressure tube, explosive, and tamper are treated using the conservation equations in their Lagrangian form.

Figure 32 shows the computational grid for the final Composition C-4 explosive driver configuration at a time of 10 μ sec after explosive initiation. Also shown are vector velocities of the tamper, explosive, pressure tube, and helium

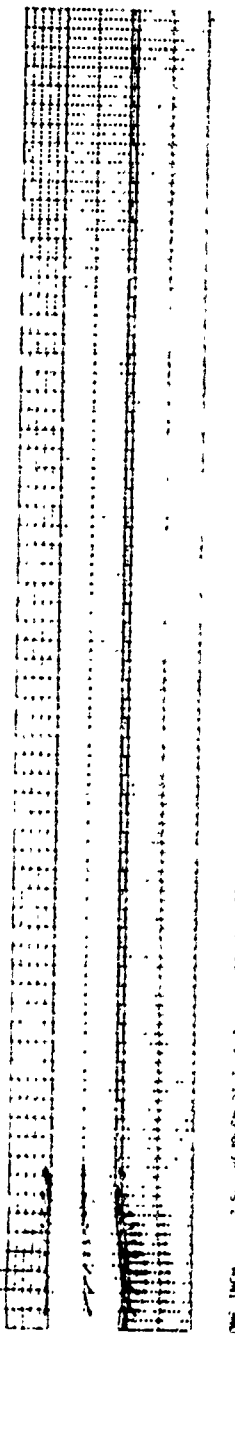


Figure 32 Velocity vector plot of the final composition C-4 explosive driver at a time of 10 usec.

at this early time. Figure 33 shows a portion of the grid and vector velocities for this computation at a time of 80 μ sec. As can be seen, the pressure tube is collapsing on axis as required and by a time of 80 μ sec. The helium shock has broken out and is leading the explosive detonation front. The calculational results show the velocity of the intersection point of the axis and pressure tube to be 0.75 cm/ μ sec. The velocity of the helium shock is 1.20 cm/ μ sec. The peak pressure of the shocked helium is 25 kbar.

This calculation and the corresponding experiments verified the design of the 25-kbar explosive driver.

4.4 TWO-DIMENSIONAL LAUNCH-CYCLE CALCULATION

A critical aspect of any gun designed to launch projectiles at very high velocities is to insure that the dynamic loading of the projectile does not result in projectile breakup. A two-dimensional calculation aided by complimentary one-dimensional calculations was performed to examine the loading of the projectile for the launch system designed in this program.

A complete two-dimensional calculation, including the explosive driver startup and complete collapse, is a very complex and lengthy computation and was beyond the scope of this program. Therefore, 2 one-dimensional Moving Wall Flume calculations were performed to provide a reasonable approximation for the time-history of the pressure tube collapse as well as the final shocked gas volume and a velocity versus time function describing the helium gas. Both of these calculations were identical to the previously described explosive driver calculation except that the full tamper and barrel of the final

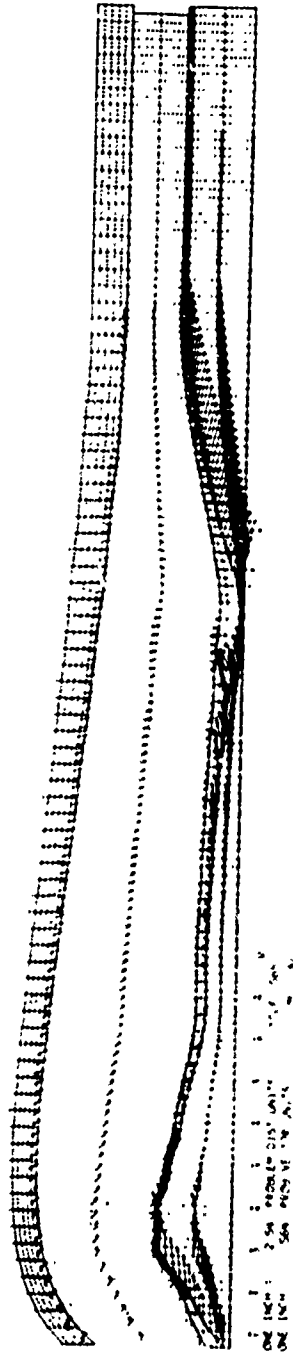


Figure 33 Velocity vector plot of the final composition C-4 explosive driver at a time of 80 usec.

launcher design were included. The initial finite-difference grid for these calculations is shown in Figure 34. The differences between these two calculations was solely in the treatment of the right boundary condition for the helium gas (Eulerian fluid). In one calculation the right boundary was a simple flow-through condition, i.e., zero velocity gradient at the boundary. In the second calculation, the right boundary was fixed, i.e., zero velocity at the boundary. These cases bound the real problem of an accelerating projectile in the barrel. The results of the two calculations were used to obtain approximate descriptions of:

- The time-history of the pressure tube collapse
- The time-dependent volume and velocity field associated with the helium just prior to interaction with the projectile

These results were used as initial and boundary conditions for the two-dimensional calculation of the response of the projectile during the first 10 μ sec of the launch cycle.

Figure 35 shows the initial zoning for the two-dimensional launch cycle calculation. The non-shaded region represents the helium gas. This region is bounded radially by a fixed boundary and on the left by a moving piston. The prescription for the moving piston was based on the results of the 2 one-dimensional calculations described above and models the collapse of the pressure tube. The zones for the helium gas had initial velocities approximating the conditions of the gas behind the helium shock front as determined from the one-dimensional calculations. The initial volume of helium gas was also based on the one-dimensional results. The shock front in the helium was at the

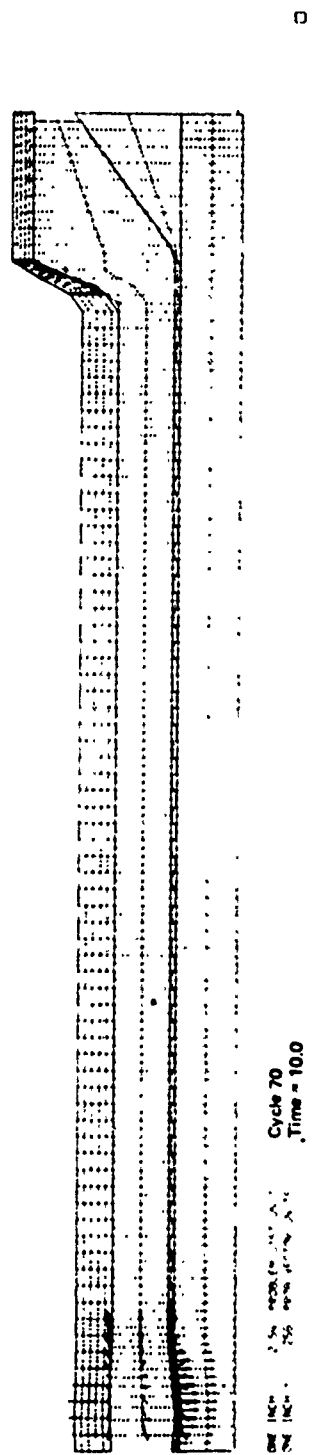


Figure 34 Velocity vector plot of the composition C-4 explosive driver with the full barrel and launcher at a time of 10 μ sec.

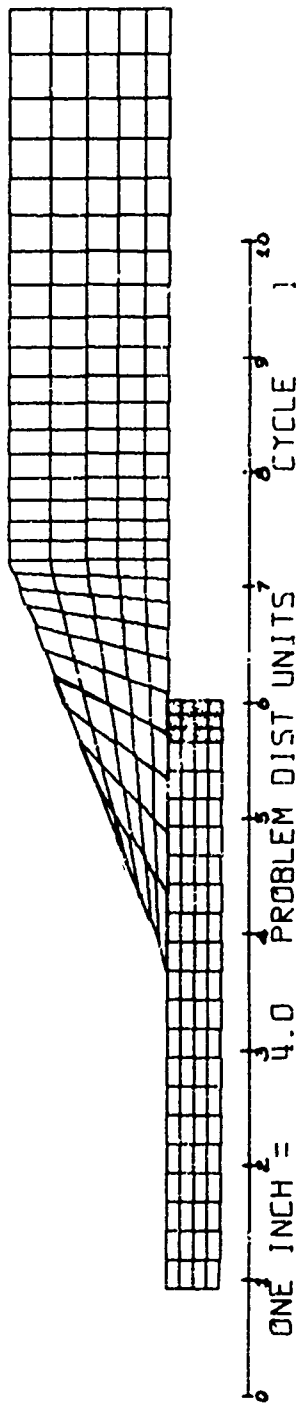


Figure 35 Initial zoning for the two-dimensional launch cycle calculation.

base of the projectile at time $t = 0$. The zones representing the magnesium-lithium (Maglith) projectile are those shaded zones to the right of the helium. The Maglith zones were initially at rest, simulating the state just prior to the projectile interacting with the driver gas. The zones immediately above the helium and projectile represent the steel barrel. The equations of state and yield models used in the two-dimensional calculation were identical to those previously described in Table III.

Figure 36 shows the computational grid at the final time of 10 μsec . As can be seen, by this time the projectile has separated from the barrel and is beginning to deform. Figure 37 shows the state of stress in the projectile at times of 2, 4, 6, 8, and 10 μsec . Until the time of about 6 μsec , the gradient of stress in the radial direction (away from axis of symmetry) is very small. However, beyond a time of about 6 μsec the reflection of the stress wave from the free surface and interaction of the projectile with the barrel result in severe radial stress gradients being established in the projectile. Between a time of 8 and 10 μsec , the projectile and barrel separate.

Due to programmatic restrictions, the zoning used in the two-dimensional launch cycle calculation was coarse, especially with respect to the steel barrel in the region near the projectile. This had the effect that a single zone in the barrel dominated the response of the projectile. This, in turn, results in a somewhat imprecise determination of the stress field in the projectile. A much more finely zoned computation would be required to determine the details of the time-dependent stress field in the projectile. Therefore, the results of the launch cycle

2DL SLUG IMPACT BY 20KBAR SHOCK

MESH PLOT

HOCK PROBLEM TIME = 1.003E+01 DATE = 73/11/27.

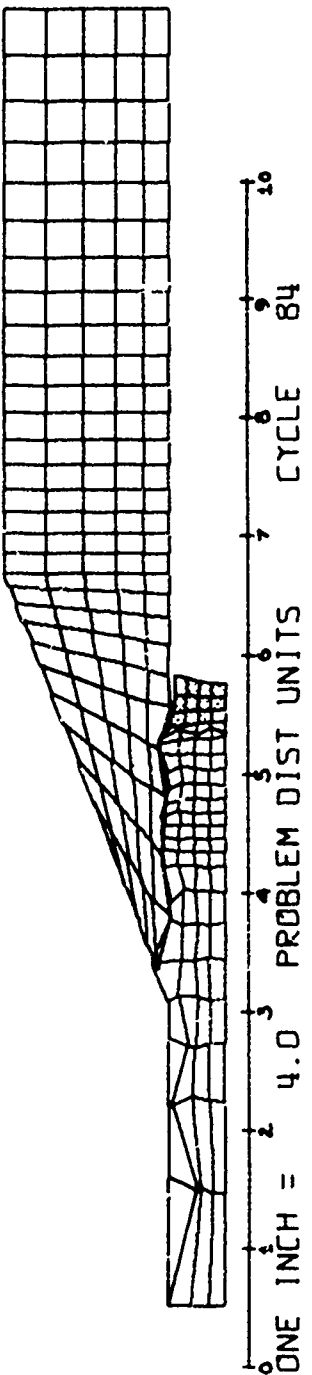


Figure 36 Final configuration of the two-dimensional launch cycle calculation at a time 10 μ sec.

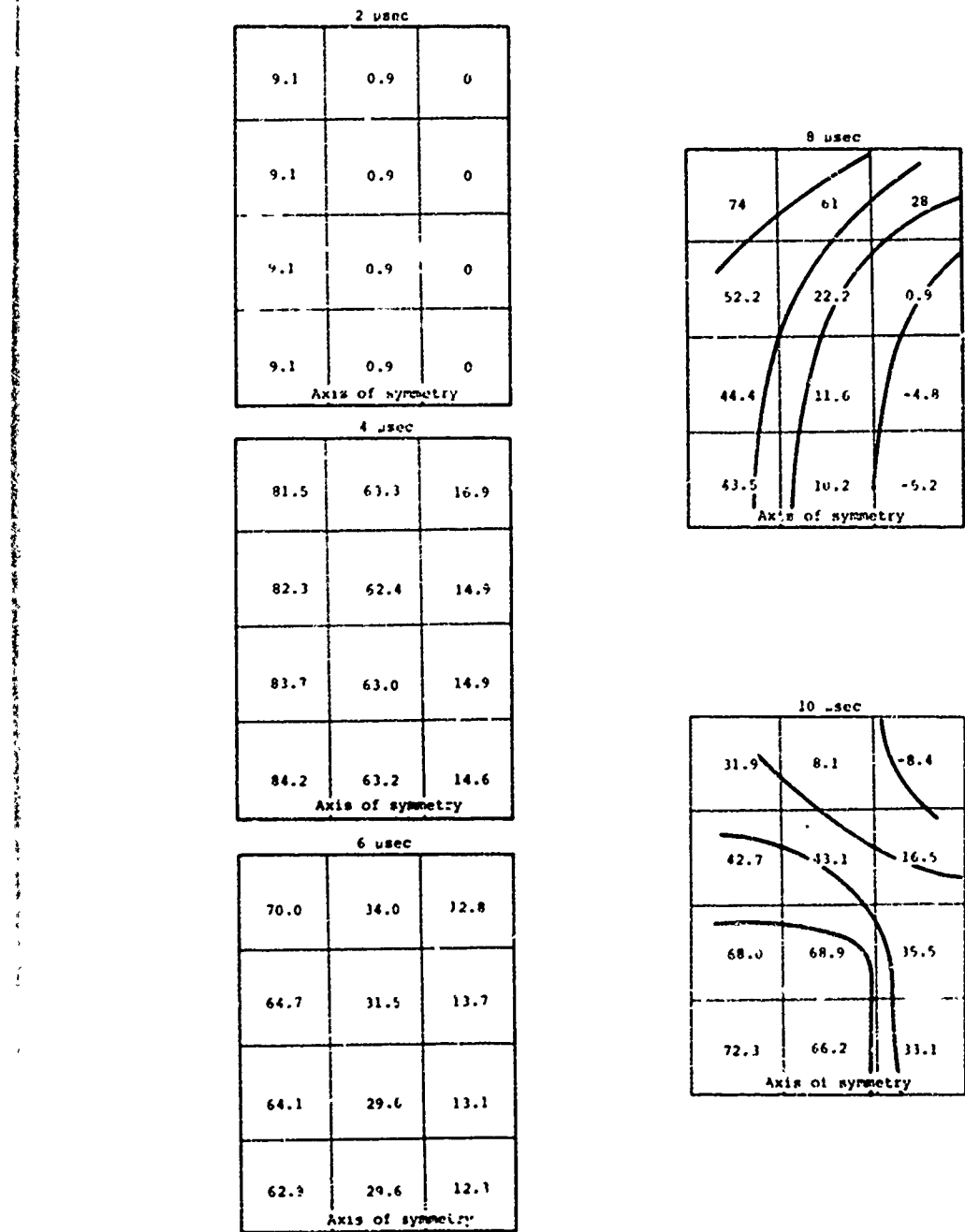


Figure 37 State of stress in the projectile for the two-dimensional calculations.

calculation must be interpreted with caution. However, on the basis of the calculation performed it is considered likely that the loading conditions that were modeled would have resulted in projectile breakup. This tentative conclusion is consistent with experimental results and the subsequent introduction of a gap between the periphery of the projectile and the barrel.

SECTION 5

ANALYSIS AND CONCLUSIONS

Significant accomplishments have been made during this six month program towards the goal of developing a multiple projectile hypervelocity launcher. Although the actual launch of intact multiple projectiles from a single barreled gun was not accomplished, the experimental results and the computational analysis completed during this program give added confidence in the ultimate feasibility of utilizing an explosive driver in a weapons system to launch multiple projectiles.

5.1 ANALYSIS

5.1.1 25-kbar Explosive Driver. Section 3.1 described the requirements in performance of an explosive driver that could be used to launch projectiles to 10 km/sec in a 20 cm barrel length. From the experiments conducted, it is evident that the explosive driver developed in this program is sufficient to accomplish the task.

Examination of the performance characteristics of the 25-kbar explosive driver yields some interesting insight into the operation of very high pressure explosive drivers. Referring back to Figure 18, the x-t diagram from shot Blunderbuss-2, it can be seen that neither the detonation velocity nor the shock

velocity are constant. Up until the time of breakout, that point at which the helium shock begins to lead the detonation in the explosive, the ion pins and cap pins report at the same time. From Figure 18, it can be seen that the detonation velocity of the C-4 explosive is 0.8 cm/ μ sec, the detonation velocity observed in detonation velocity tests.

After breakout of the helium shock in front of the detonation wave occurs, there is a marked acceleration of the detonation velocity of the C-4 to a velocity of 0.914 cm/ μ sec. This is an increase of 14 percent over the conventional detonation velocity. The mechanism whereby this increase in detonation velocity occurs is a precompression of the C-4 by the shock in the helium. As the shock in the helium moves out in front of the detonation wave, it transmits a shock through the metal pressure tube into the explosive. For the driver designed here, the pressure transmitted to the explosive would be on the order of 25 kbar. This precompression of the explosive increases its density, and the detonation velocity is increased. While this phenomenon increases the energy density of the explosive, the volume of the explosive is decreased due to the precompression, and, as would be expected, total energy is conserved.

As the detonation velocity increases, the shock velocity in the helium gas also increases to a relatively stable velocity of 1.147 cm/ μ sec. This shock velocity corresponds to an incident shock pressure of 25 kbar. However, as the detonation proceeds down the explosive driver, losses begin to occur that degrade the performance of the driver. The most significant losses arise from the entrainment of bubbles of high pressure gases at the collapse point of the pressure tube and the radial expansion of the pressure tube behind the shock front due to the extremely high pressures. This loss of gas behind the shock front sends

rarefactions towards the shock, and results in a net lowering of the incident shock velocity and a corresponding lowering of the incident pressure.

Again from Figure 18, the final shock velocity is about 1.055 cm/ μ sec. This equates to a shock pressure of 19.8 kbar. A reduction in shock pressure from 25 to 19.8 kbar has taken place due to driver losses.

The first task required in this program was the development of an explosive driver capable of producing pressures on the order of 25 kbar in order to launch disk-like projectiles to velocities of 10 km/sec. An explosive driver was developed that was designed to yield a 25-kbar incident shock in helium, and which actually yields an incident shock on the order of 20 kbar. Experimental evidence in launching projectiles obtained during this program indicates that the driver developed is sufficient for the program requirements.

5.1.2 Hypervelocity Launcher System. This program was designed to study the basic feasibility of a method that would be able to launch multiple projectiles to velocities of > 9 km/sec. As such, the goals of the program were not to design operational or prototype systems for field use, but rather to examine the basic explosive driver launcher techniques to determine the feasibility of developing a launcher within the parameters of the conceptual system requirements.

The approach to the problem was as follows: Two capabilities must be developed to be able to launch multiple projectiles to hypervelocities within an overall length approximating one meter.
(1) An explosive driver must be developed that will yield reservoir

conditions capable of launching a projectile package of 2 gm/cm^2 areal density, and (2) a projectile-sabot assembly must be designed to launch multiple individual projectiles from a single barrel. In order to maintain a 2 gm/cm^2 areal density, this projectile-sabot assembly will be in the form of a flat disk. Therefore, to prove feasibility of the concept, a method of launching this disk-like projectile to hypervelocities must first be developed.

This initial feasibility study concentrated on the ability to launch intact disk-like plates. For this reason, all shots (with the exception of three) dealt with the development of a launch cycle capable of accelerating a flat disk-like projectile to velocities of 9 km/sec (30,000 ft/sec).

In the first design (Figure 13), the edges of the plate (projectile) broke up rather early in the acceleration process. Several other methods of support were tried (Figures 17 and 21) without success. Intuition (later confirmed by a two-dimensional calculation) indicated that the interface between the steel barrel and the outer periphery of the low-density metal plate was the source of the problem. At least two problems stem from this interface. When stresses of the order of 100 kbar are applied to the two metals, the stress across the interface must also be of this magnitude. The shear stress as the plate tries to slide down the barrel will be in the tens of kilobars. The edge drag caused by these stresses can result in the edges lagging the rest of the plate. This would obviously lead to breakage of the edges. The second problem comes from the severe impedance mismatch between the two metals. This mismatch results ultimately in a stress gradient across the interface which causes an inward radial motion of the periphery of the plate.

With axial shock waves of approximately 100 kbar, the radial motions caused by such phenomena can be large enough to cause break-up of the plate.

It was for the above reasons that the design of the plate was changed to that shown in Figure 15. The space between the edge of the plate and the steel barrel was filled on one shot with silicone grease and in another with Teflon. It was hoped that this geometry would improve the impedance mismatch problems and eliminate the edge drag. The change was quite effective--the plate must have held together until the plate emerged from the barrel in order to achieve the observed velocity. Our analysis indicates, however, that at this time the plate was still subjected to approximately 35 kbar of axial pressure. The edge rarefactions resulting from the sudden release of such a high pressure would also cause a plate to break-up. In the final shot, PI took the chance that these rarefactions would lead to the expansion and breakup of the sabot but not of the 1 gram particles embedded in the sabot. Unfortunately, both the sabot and the particles broke up.

5.2 CONCLUSIONS

The objectives of this six-month program were: (1) to demonstrate the ability of an explosive driver to launch a projectile to 9 to 10 km/sec within a total length of 1 meter and, (2) to determine the feasibility of launching multiple projectiles using the above launcher. During this program the following specific tasks were accomplished:

- An explosive driver capable of producing an incident shock in helium gas of 20 kbar has been produced and has been shown to work reliably and repeatedly.

- A series of one-dimensional and one and one-half dimensional computer calculations was performed to understand driver performance and to aid in the two-dimensional calculation of the initial stages of projectile launch.
- Experimental shots were conducted with a 1-meter-long launcher that were successful in launching 25-gram projectiles to a velocity of 9.6 km/sec. The projectiles were only partially intact at distances of 2 feet down range. It is felt that the cause of projectile breakup is interaction between the projectile and the barrel during the launch cycle.
- A two-dimensional Lagrangian computer calculation was performed to analyze the initial launch cycle characteristics of the hypervelocity launcher. This calculation showed that the most likely cause of projectile breakup is induced inward radial velocities in the projectile due to the passage of the shock wave in the steel barrel over the projectile.

With the results of the computer calculation and a careful review of the test results, it is felt that the cause of projectile breakup can be isolated and corrected. If this deficiency is corrected, then it appears feasible that a launcher can be produced using the techniques developed in this program to launch intact multiple projectiles.

REFERENCES

1. J. D. Watson, E. T. Moore, Jr., D. Mumma, and J. S. Marshall, Explosively-Driven Light Gas Guns, PIFR-024/065, Physics International Company, San Leandro, California, September 1967.
2. E. T. Moore, Jr., Explosive Hypervelocity Launchers, NASA CR-982, Physics International Company, San Leandro, California, February 1968.
3. R. F. Flagg, J. S. Marshall, Jr., J. D. Watson, and E. T. Moore, Jr., Explosively-Driven Launchers, PIPR-098-SA-1, Physics International Company, San Leandro, California, April 1968.
4. J. D. Watson, An Explosively Driven-Gun to Launch Large Models to Reentry Velocities, PIFR-098, Physics International Company, San Leandro, California, April 1970.
5. J. D. Watson, A Summary of the Development of Large Explosive Guns for Reentry Simulation, PIFR-155, Physics International Company, San Leandro, California, August 1970.
6. G. B. Steel, Design Criteria for Explosive Drivers Used for Atmospheric Blast Simulation, PIFR-062, Physics International Company, San Leandro, California, September 1967.
7. S. Gill, E. T. Moore, D. Randall, and S. Gross, Evaluation of High-Pressure Airblast Attenuation Effectiveness of Air Entrainment Subsystems, NCEL Report CR69.025, Physics International Company, San Leandro, California, June 1970.
8. Purchase Description for Feasibility of Explosively-Driven Hypervelocity Projectiles, Attachment No. 1 to RFQ DAAK02-73-Q-1563, U.S. Army MERDC, Fort Belvoir, Virginia.

REFERENCES (cont.)

9. J. S. Rinehart and J. Pearson, Behavior of Metals Under Impulsive Loads, Dover Publications, Inc., New York, New York, 1965.
10. I. C. Skidmore, "An Introduction to Shock Waves in Solids," Applied Materials Research, 131-147, July 1965.
11. B. M. Butcher, L. M. Barker, D. E. Munson, and C. D. Lundergan, "Influence of Stress History on Time-Dependent Spall in Metals," AIAA Journal, 2, 6, 977-990 (1964).
12. D. G. Doran and R. K. Linde, "Shock Effects in Solids," Solid State Physics, 13, 229-290 (1966).
13. T. Barbee, L. Seaman, and R. C. Crewdson, Dynamic Fracture Criteria of Homogeneous Materials, AFWL-TR-70-99, Air Force Weapons Laboratory, Kirtland Air Force Base, New Mexico, November 1970.
14. S. P. Gill, Initiation and Decomposition of Nitromethane at 10-kbar Pressure, PITR-70-2, Physics International Company, San Leandro, California, March 1970.
15. A. E. Seigel, Theory of High Speed Guns, Agardograph 91, NATO-AGARD Fluid Dynamics Panel, North Atlantic Treaty Organization (1965).
16. I. T. Glass and J. Gordon Hall, Handbook of Supersonic Aerodynamics, Section 18, "Shock Tubes," p. 111 Navord Report 1488, Vol. 6, December 1959.

APPENDIX A
PISCESTM IDE
A ONE-DIMENSIONAL EULERIAN CONTINUUM MECHANICS CODE

PISCES 1DE
A ONE-DIMENSIONAL EULERIAN CONTINUUM MECHANICS CODE

TECHNICAL MEMO TCM 73-14

Stephen C. Jardin

September 1973

**Applied Mechanics Department
Physics International Company
2700 Merced Street
San Leandro, California 94577**

S.S.

TCAM 73-14

CONTENTS

	<u>Page</u>
LIST OF SYMBOLS	111
SECTION 1 INTRODUCTION	1
SECTION 2 THE DIFFERENTIAL EQUATIONS	3
SECTION 3 THE DIFFERENCE EQUATIONS	9
SECTION 4 SAMPLE CALCULATIONS	13
SECTION 5 CONCLUDING REMARKS	31
REFERENCES	33
APPENDIX A ACCURACY AND STABILITY OF THE DIFFERENCE EQUATIONS	A-1
APPENDIX B INPUT	B-1

LIST OF SYMBOLS

r, x	space variable
t	time variable
ρ	mass density
u	material velocity
A	cross-sectional area of duct in flume symmetry ($d=4$)
Σ_r	radial stress = $-p + s_1$
Σ_θ	tangential stress = $-p + s_2$
e	specific internal energy
p	pressure
η	$= \frac{\rho}{\rho_0} - 1$
V	relative volume = ρ_0/ρ
E	internal energy = $\rho_0 e$
ρ_0	reference density
a_1 a_2 a_3 b	{ equation of state coefficients
s_1	first stress deviator
s_2	second stress deviator
s_3	third stress deviator
μ	shear modulus
γ_0	yield strength

TCAM 73-14

m	momentum density = ρu
e	total energy density = $\rho(e + u^2/2)$
S	first stress deviator density = ρs_1
T	second stress deviator density = ρs_2
\vec{U}	material state vector
\vec{F}	
\vec{G}	
\vec{R}	
C_q	vector quantities
c	artificial viscosity coefficient
f_{ts}	sonic velocity
f_{ac}	time step "safety factor"
$\overset{\exists}{A}$	time step accuracy factor
$\overset{\exists}{A}$	Jacobian matrix $\partial \vec{F} / \partial \vec{U}$
$\overset{\exists}{B}$	Jacobian matrix $\partial \vec{G} / \partial \vec{U}$
$\overset{\exists}{C}$	$= \overset{\exists}{A} - \rho u \overset{\exists}{B}$
$\overset{\exists}{T}_\Delta$	truncation error
$\overset{\exists}{U}$	Fourier amplitude vector
k	wave number
w	angular frequency
$\overset{\exists}{Z}$	amplification matrix
λ_c	eigenvalue of the matrix $\overset{\exists}{C}$
Y	ratio of specific heats
K	bulk modulus
$\overset{\exists}{I}$	unit matrix

SECTION I
INTRODUCTION

What follows is a description of a numerical method for the solution of the time-dependent equations of continuum mechanics expressed in an Eulerian framework. The method is general in that a wide range of material models may be incorporated into it. The differential equations solved are the Eulerian counterpart of the Lagrangian equations formulated by Wilkins (Reference 1). The difference method used is essentially that made popular by MacCormack (Reference 2). It is shown to be of second-order accuracy in both space and time and stability criteria are derived. The results of several sample problems using this method are presented and compared to solutions obtained using the PISCES IDL computer code.

SECTION 2
THE DIFFERENTIAL EQUATIONS

The partial differential equations listed below are those solved by the computer code. For flow in one space variable (r) and time (t), the equations for plane ($d = 1$), cylindrical ($d = 2$), spherical ($d = 3$) and flume ($d = 4$) geometries are (References 1,3,4):

Equation of continuity

$$\frac{\partial p}{\partial t} + \frac{\partial}{\partial r}(\rho u) + (d-1)\frac{\partial u}{r} = 0 \quad d = 1,2,3$$

$$\frac{\partial}{\partial t}(\rho A) + \frac{\partial}{\partial r}(\rho u A) = 0 \quad d = 4$$

Equation of motion

$$\frac{\partial}{\partial t}(\rho u) + \frac{\partial}{\partial r}(r u^2 - \bar{z}_T) - \frac{(d-1)}{r} \left[\Sigma_T - \Sigma_{f_1} - \rho u^2 \right] = 0 \quad d = 1,2,3$$

$$\frac{\partial}{\partial t}(\rho u A) + \frac{\partial}{\partial r}(\rho u^2 A) + A \frac{\partial p}{\partial r} = 0 \quad d = 4$$

Energy equation

$$\frac{\partial}{\partial t} \left[\rho \left(e + \frac{1}{2} u^2 \right) \right] + \frac{\partial}{\partial r} \left[\rho u \left(e + \frac{1}{2} u^2 - \frac{1}{\rho} \bar{z}_T \right) \right] + (d-1) \frac{\rho u}{r} \left(e + \frac{1}{2} u^2 - \frac{1}{\rho} \Sigma_T \right) = 0 \quad d = 1,2,3$$

$$\frac{\partial}{\partial t} \left[\rho \left(\frac{u^2}{2} + e \right) \right] + \frac{\partial}{\partial r} \left[\rho u A \left(e + \frac{P}{\rho} + \frac{u^2}{2} \right) \right] + P \frac{\partial A}{\partial r} = 0 \quad d = 4$$

An equation of state must be provided to determine the pressure, p , as a function of the relative volume, $V = \rho_0/\rho$, and the internal energy, $E = \rho_0 e$. For example, a typical equation of state might be

$$p = a_1(\eta - 1) + a_2(\eta - 1)^2 + a_3(\eta - 1)^3 + b\eta E$$

where a_1, a_2, a_3 and b are constants and $\eta = 1/V = p/p_0$.

For flume symmetry ($d = 4$) the area $A(r,t)$ must be supplied (along with initial and boundary conditions) to complete the specification of the problem. This area function may be either pre-specified or it may be determined dynamically during the course of the calculation.

For the other geometries ($d = 1, 2, 3$) we need additional relations to determine $\Sigma_r (d = 1, 2, 3)$ and $\Sigma_\theta (d = 2, 3)$ as these are not, in general, determined completely by the pressure, p . These relations are

$$\Sigma_r = -p + s_1$$

$$\Sigma_\theta = -p + s_2$$

where the stress deviators s_1 and s_2 are determined from the following relations.

The first stress deviator equation:

$$\frac{\partial}{\partial t}(\rho s_1) + \frac{\partial}{\partial r}(\rho u s_1) - \frac{4}{3}\mu \frac{\partial u}{\partial r} + \frac{(d-1)\mu u}{r} \left(s_1 + \frac{2}{3}\mu \right) = 0 \quad (d = 1, 2, 3)$$

The second stress deviator equation:

$$\frac{\partial}{\partial t}(\rho s_2) + \frac{\partial}{\partial r}(\rho u s_2) + \frac{2}{3}\mu \rho \frac{\partial u}{\partial r} - 2\mu \rho \frac{u}{r} + (d-1) \frac{\mu u}{r} \left(s_2 + \frac{2}{3}\mu \right) = 0 \quad (d = 2, 3)$$

$$s_2 = -\frac{1}{2}s_1 \quad (d = 1)$$

TCAM 73-14

The third stress deviator equation:

$$s_3 = -[s_1 + s_2] \quad (d = 1, 2, 3)$$

where μ is the shear modulus.

The stress deviators as determined above are then modified by a yield condition. For example,

$$(s_1^2 + s_2^2 + s_3^2) - \frac{2}{3}Y_0^2 \leq 0$$

where Y_0 is the material strength.

Next, we rewrite the above equations in vector form, introducing the variables

$$\begin{aligned} p \\ m = \mu u \\ c = \rho(e + u^2/2) \\ S = \rho s_1 \\ T = \rho s_2 \end{aligned}$$

The equations assume the compact form

$$\frac{\partial}{\partial t} \vec{U} + \frac{\partial}{\partial r} \vec{F} = \rho \mu \frac{\partial}{\partial r} \vec{C} + \vec{R}$$

where

$$\vec{U} = \begin{bmatrix} p \\ m \\ c \\ S \\ T \end{bmatrix}$$

TCAM 73-14

$$\vec{F} = \begin{bmatrix} m \\ \frac{m}{r} \alpha - \Sigma_r \\ \frac{m}{r} (\epsilon - \Sigma_r) \\ \frac{m}{r} \alpha S \\ \frac{m}{r} \alpha T \end{bmatrix}$$

$$\vec{C} = \begin{bmatrix} 0 \\ 0 \\ 0 \\ \frac{4m}{3\rho} \\ -\frac{2m}{3\rho} \end{bmatrix}$$

$$\vec{R} = \begin{bmatrix} 0 \\ 0 \\ 0 \\ 0 \\ 0 \end{bmatrix} \quad d = 1$$

$$\vec{R} = \begin{bmatrix} -(d-1)\frac{m}{r} \\ \frac{(d-1)}{r} \left[\Sigma_r - \Sigma_\theta - \frac{m^2}{\rho} \right] \\ -\frac{(d-1)}{r} \frac{m}{\rho} [\epsilon - \Sigma_r] \\ -\frac{(d-1)}{r} m \left[\frac{S}{\rho} + \frac{2}{3} \mu \right] \\ 2 \mu \rho \frac{u}{r} - (d-1) \frac{m}{r} \left(\frac{T}{\rho} + \frac{2}{3} \mu \right) \end{bmatrix} \quad d = 2, 3$$

TCAM 73-14

$$\vec{R} = \begin{bmatrix} -\frac{1}{A} \frac{dA}{dr} m - \frac{1}{A} \frac{dA}{dt} p \\ -\frac{1}{A} \frac{dA}{dr} p^2 - \frac{1}{A} \frac{dA}{dt} m \\ -\frac{1}{A} \frac{dA}{dr} p (e+p) - \frac{1}{A} \frac{dA}{dt} (e+p) \\ 0 \\ 0 \end{bmatrix} \quad d=4$$

A-7

SECTION 3
THE DIFFERENCE EQUATIONS

The two-step difference method used to approximate the solution to Eq. (1) is defined by

$$\vec{U}_j^* = \vec{U}_j^n - \frac{\Delta t}{\Delta x} (\vec{F}_{j+1}^n - \vec{F}_j^n) + (\rho \mu)_{j+\frac{1}{2}}^n \frac{\Delta t}{\Delta x} (\vec{G}_{j+1}^n - \vec{G}_j^n) + \Delta t \vec{R}_j^n \quad (2a)$$

$$\vec{U}_j^{n+1} = \frac{1}{2} \left[\vec{U}_j^* + \vec{U}_j^n - \frac{\Delta t}{\Delta x} (\vec{F}_j^* - \vec{F}_{j-1}^*) + (\rho \mu)_{j-\frac{1}{2}}^* \frac{\Delta t}{\Delta x} (\vec{G}_j^* - \vec{G}_{j-1}^*) + \Delta t \vec{R}_j^* + \vec{D}_j^n \right] \quad (2b)$$

where the subscripts refer to a spatial mesh of points x_j with spacing Δx and the superscripts refer to the times

$$t^n = \sum_{i=1}^n \Delta t^i$$

where Δt^i is the time increment that the solution is advanced during cycle i . Also, \vec{F}_j^n , \vec{G}_j^n , and \vec{R}_j^n equal $\vec{F}(\vec{U}_j^n)$, $\vec{G}(\vec{U}_j^n)$, and $\vec{R}(\vec{U}_j^n)$, respectively.

\vec{D}_j^n is the artificial viscosity operator given by the expression

$$\vec{D}_j^n = C_q \frac{\Delta t}{\Delta x} \left[|u_{j+1}^n - u_j^n| (\vec{U}_{j+1}^n - \vec{U}_j^n) - |u_j^n - u_{j-1}^n| (\vec{U}_j^n - \vec{U}_{j-1}^n) \right]$$

where u_j^n is the material velocity at position x_j and at time t^n and C_q is a constant of order unity. A value of C_q different from zero is not needed for stability in calculations for which the linear stability

analysis applies, but may be needed to preserve stability when computing a strong shock, motion near the axis of cylindrical or spherical symmetries, or other violent or nonlinear phenomena. For these calculations, a value of C_q of 2.0 should suffice to preserve numerical stability.

The finite-difference method of Eq. (2) first obtains the approximate value \tilde{U}_j^* at each point by Eq. (2a) which uses forward differences to approximate the spatial derivatives. The approximate solution is then used to calculate \tilde{F}_j^* , \tilde{G}_j^* , and \tilde{R}_j^* which are used with backward differences in Eq. (2b) to obtain the new value of the solution \tilde{U}_j^{n+1} .

The specification of the solution is complete if, in addition to the prescription (2) for advancing the solution in time, we provide initial conditions \tilde{U}_j^0 ; $j = 0, 1, \dots, j_{\max}$, and boundary conditions $\tilde{U}_0^n, \tilde{U}_{j_{\max}}^n$; $n = 0, 1, \dots, n_{\max}$.

The accuracy and stability of the difference method (2) is analyzed in the Appendix. It is shown there that the method is of second order accuracy and that the linearized stability criterion is given by the well known Courant Friedrichs Lewy (CFL) condition $\frac{\Delta t}{\Delta x} (|u| + c) \leq 1$ where u is the local fluid velocity and c is the local sonic velocity. The linearized stability criterion is a necessary but not sufficient condition to insure stability of the actual difference equations which are nonlinear. Thus, to apply the CFL criterion, we introduce a time step "safety factor" f_{ts} (where $0 < f_{ts} < 1$) and determine the stable time step from the condition

$$\Delta t \leq f_{ts} \frac{\Delta x}{|u| + c} \quad (3)$$

The CFL stability criterion is obtained by ignoring the effect of the vector \tilde{R} . It is easily seen that the inclusion of \tilde{R} does not significantly

affect the linearized stability criterion quoted above as the change in the eigenvalues of the associated amplification matrix is only the order of Δt . Also, \tilde{R} is included in the two-step difference scheme in such a manner that the method retains its second-order accuracy. Although the method is strictly accurate to second order, the vector \tilde{R} may be of such a magnitude that the third-order inaccuracy in \tilde{R} dominates the other error terms, resulting in an effective loss of accuracy in the spatial derivative terms.

To insure that this is not the case, we subject the time step Δt to the additional constraint

$$\Delta t \leq (f_{ac}) \frac{U_1}{R_1} \quad (4)$$

where U_1 and R_1 are the first components of the vectors \tilde{U} and \tilde{R} and (f_{ac}) is an "accuracy factor" which satisfies $0 \leq f_{ac} < 1$. A recommended value for f_{ac} is 0.2.

The actual time step Δt used in each cycle of the calculation is the maximum value of Δt which satisfies the two criteria of Eqs. (3) and (4) at each location in the mesh.

SECTION 4 SAMPLE CALCULATIONS

The results of several simple calculations are presented in graphical form in this section for the purpose of illustrating the computational capability of the numerical method presented. Each problem was run both with the PISCES IDE code and with the PISCES IDL code to facilitate comparisons between the accuracy and the efficiency of the two codes in solving a wide class of one-dimensional continuum mechanics problems. In each case, the two codes used the same number of zones (or mesh points) and were run for the same amount of problem time. The number of computational cycles and the computer time needed to run differed between the two codes because of different time-step stability criteria for Lagrangian and Eulerian codes. Timing tests have shown the zone cycle time (the time to compute one zone for one cycle) to be virtually identical in PISCES IDL and PISCES IDE.

Test Problem 1: Elastic-Plastic Plane Plate Impact

At time $t = 0$, a steel plate of thickness $25 \times .1$ (100 zones) moving at a velocity of $.004 \text{ cm}/\mu\text{sec}$ impacted a stationary steel plate of thickness 25 cm . The steel was modeled with $\rho = 7.85$, $K = 1.69$, $G = .822$, and a von Mises yield strength of $Y_0 = .003$.

The results of the Eulerian and the Lagrangian calculation are summarized in Figures 1a and 1b, where a series of stress profiles at different times are superimposed. No artificial viscosity was used in either calculation. PISCES IDE required 102 cycles to run this problem to $35 \mu\text{sec}$ while PISCES IDL required 129 cycles.

Test Problem 2: Flume Test A

At time $t = 0$, there exists a gas with $\rho = .01$, $\gamma = 5/3$ in a straight flume of length 40 cm (100 zones). A center section of 4 cm initially has an energy density of 10^{-5} (hot gas) while the remainder of the gas has an initial energy density of 1.5×10^{-9} (cold gas).

Figures 2a and 2b show the pressure distributions in the pipe at three successive times. The 1DL problem used a quadratic artificial viscosity coefficient of 2.0 and a linear artificial viscosity coefficient of 0.1. The 1DE problem used $CQ = 2.0$. PISCES 1DE required 115 cycles to run this problem to 250 μ sec, while PISCES 1DL took 354 cycles.

Test Problem 3: Flume Test B

This problem is identical to Test Problem 2 except for the shape of the flume. In Test Problem 2, the flume was straight. In this problem, the flume has a straight section in the center section of 4 cm and then diverges outward from the center each way with a slope of 1/8.

The results of this problem are illustrated in Figure 3. PISCES 1DE required 116 cycles and PISCES 1DL required 330 cycles to run this problem to 250 μ sec.

Test Problem 4: Cylindrical Implosion--Paynes Problem

This is a problem whose solution by other methods appears in the literature (References 6 and 7). The initial conditions in cylindrical coordinates (r, θ) are: $\rho = 1.67$, $p = 1$, $m = 0$ for $r \leq 1$; $\rho = 6.67$, $p = 4$, $m = 0$ for $r > 1$. The gas is ideal with $\gamma = 5/3$. The material was divided into equally spaced zones of width .02 cm.

TCAM 73-14

Figures 4a and 4b summarize the results of the calculations using PISCES 1DE and PISCES 1DL. The Lagrange calculation used a quadratic artificial viscosity coefficient of 2.0 and no linear artificial viscosity. The Euler calculation used a coefficient of 2.0 for artificial viscosity. The problem required 258 cycles in 1DE and 492 cycles in 1DL to run out to time t = 1.4.

Test Problem 5: Elastic-Plastic Cylindrical Plate Impact

At time $t = 0$ a steel spherical shell of thickness 37.5 (150 zones) moving inward with a radial velocity of .004 impacts a steel sphere of radius 12.5 (50 zones).

Stress profiles from the 1DE and the 1DL calculation are illustrated in Figures 5a and 5b. PISCES 1DL used 2.0 for a quadratic viscosity coefficient and 0.0 for linear viscosity. PISCES 1DE used a coefficient of viscosity of 2.0. It took 198 cycles for 1DE to run out to time $t = 60$ and 198 cycles for 1DL.

Test Problem 6: Spherical Implosion

This problem is identical to Test Problem 4 except that the symmetry is spherical rather than cylindrical. The results are illustrated in Figures 6a and 6b.

Test Problem 7: Elastic-Plastic Spherical Plate Impact

This problem is identical to Test Problem 5 except that the symmetry is spherical rather than cylindrical. The results are illustrated in Figures 7a and 7b.

TCAN 73-14

TEST PROBLEM 1 EULERIAN ELASTIC PLASTIC PLANE PLATE IMPACT

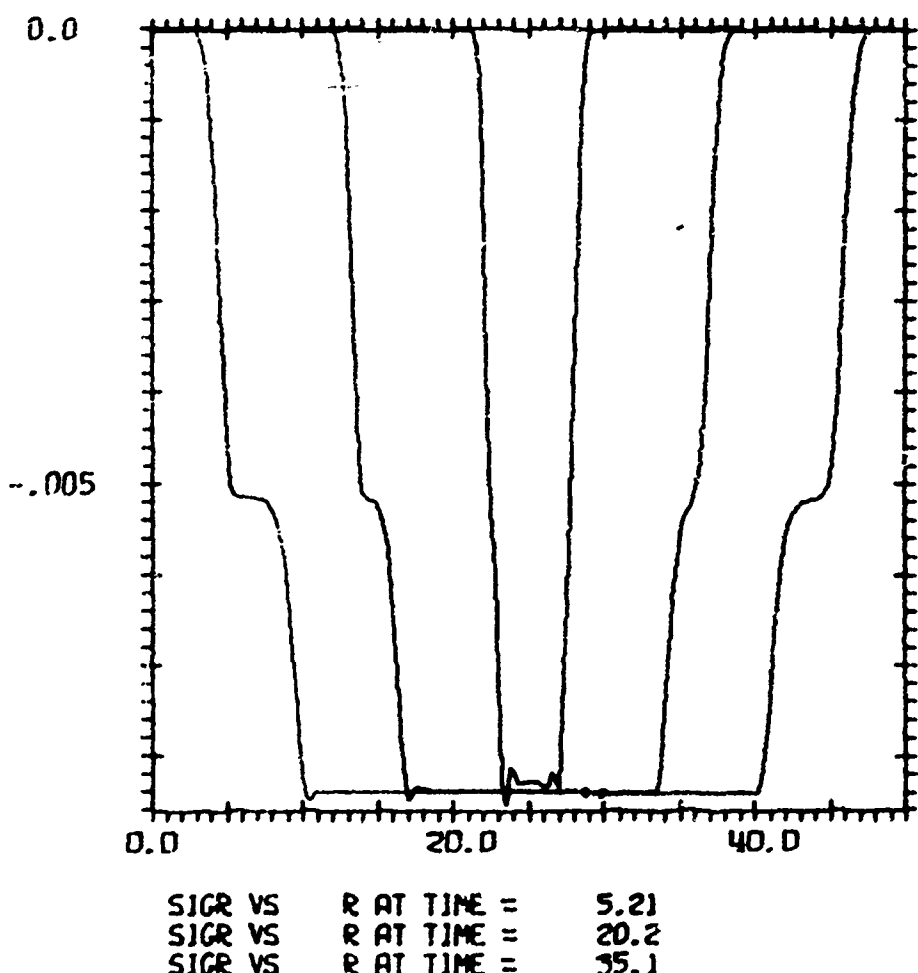


Figure 1a

TCAM 73-14

TEST PROBLEM 3 LAGRANGE ELASTIC PLASTIC PLANE PLATE IMPACT

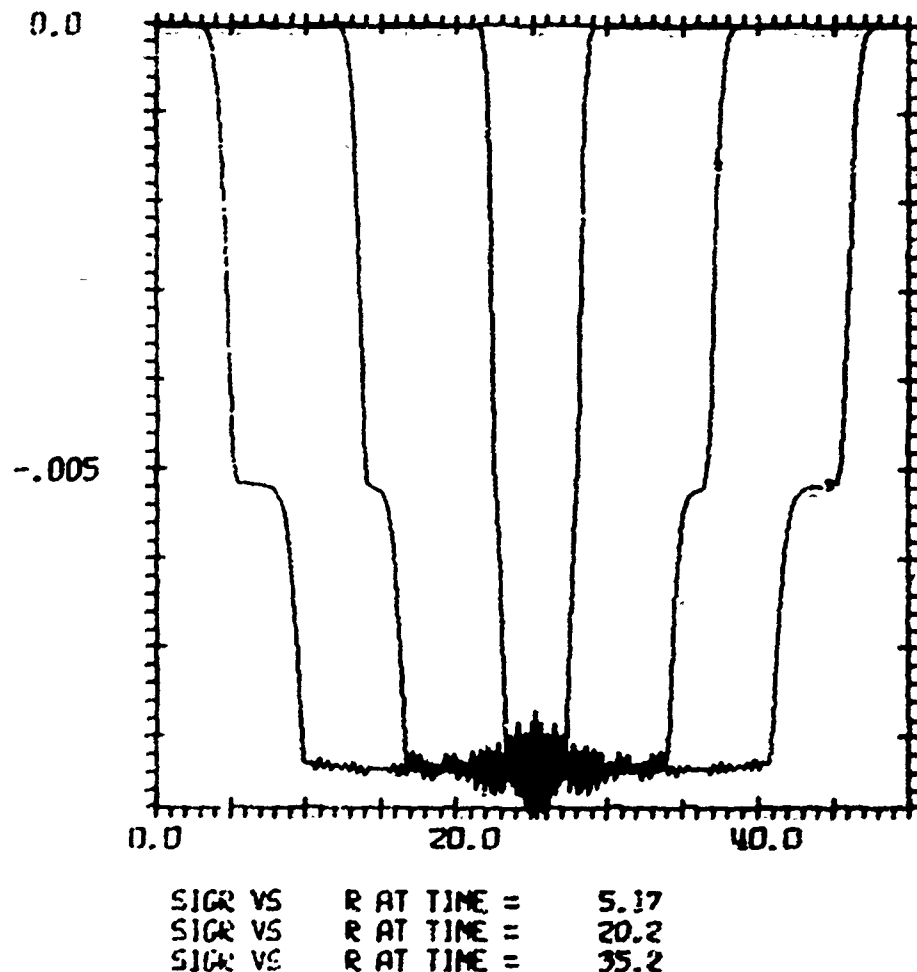


Figure 1b

TCAM 73-14

FILTER EJECTION - FLUME TEST A - LULER

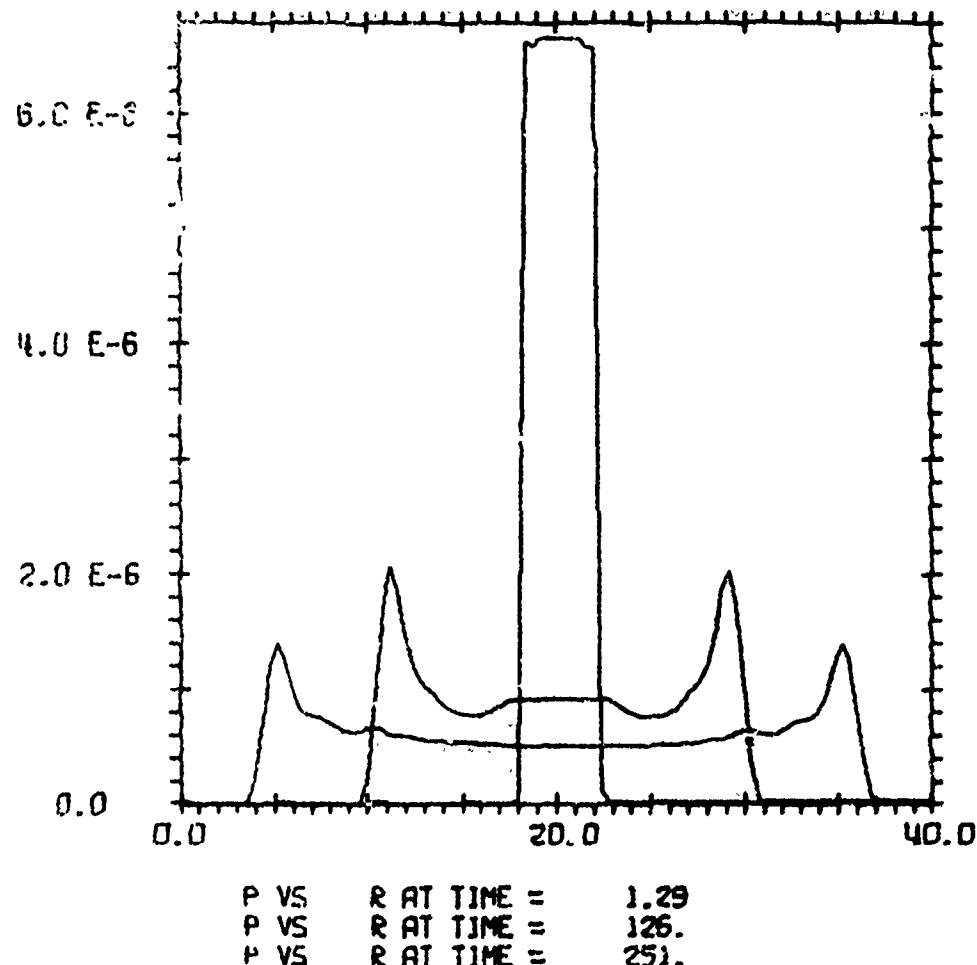


Figure 2a

TCAM 73-14

EULER LAGRANGE - FLUME TEST A - LAGRANGE

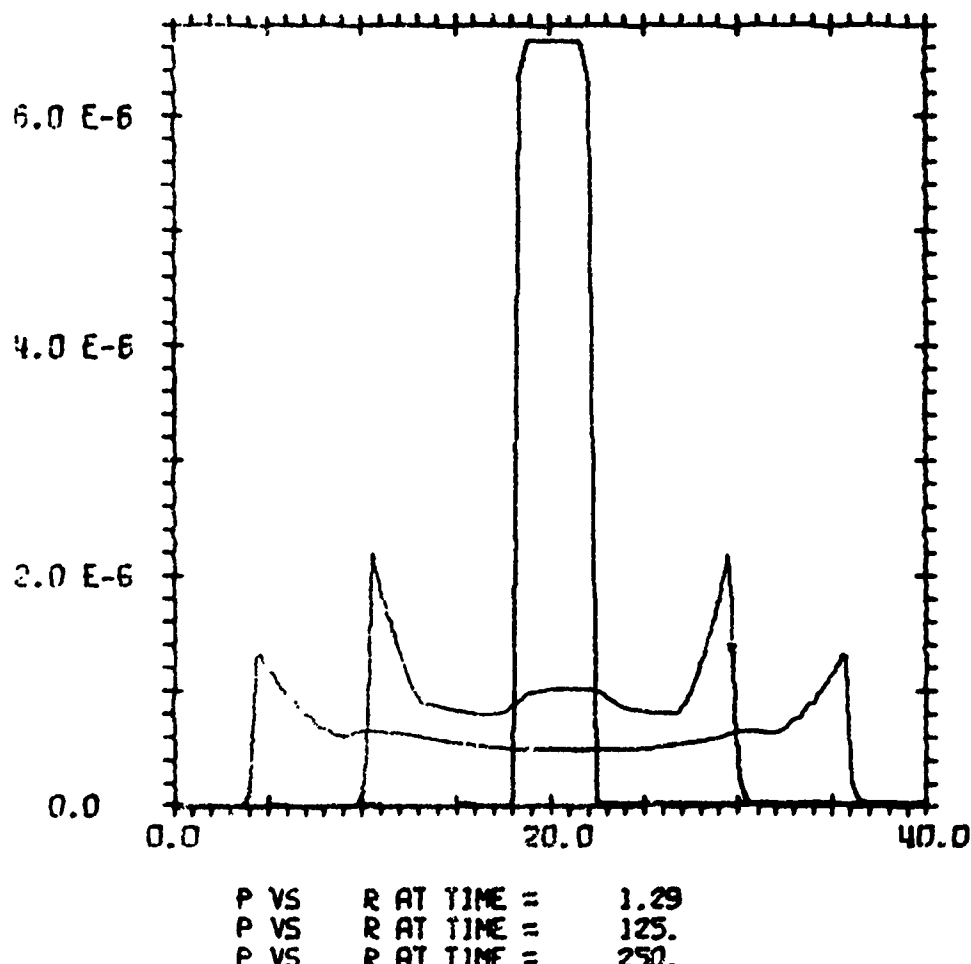


Figure 2b

TCAN 73-14

EULER/LAGRANGE - FLUME TEST B - EULER

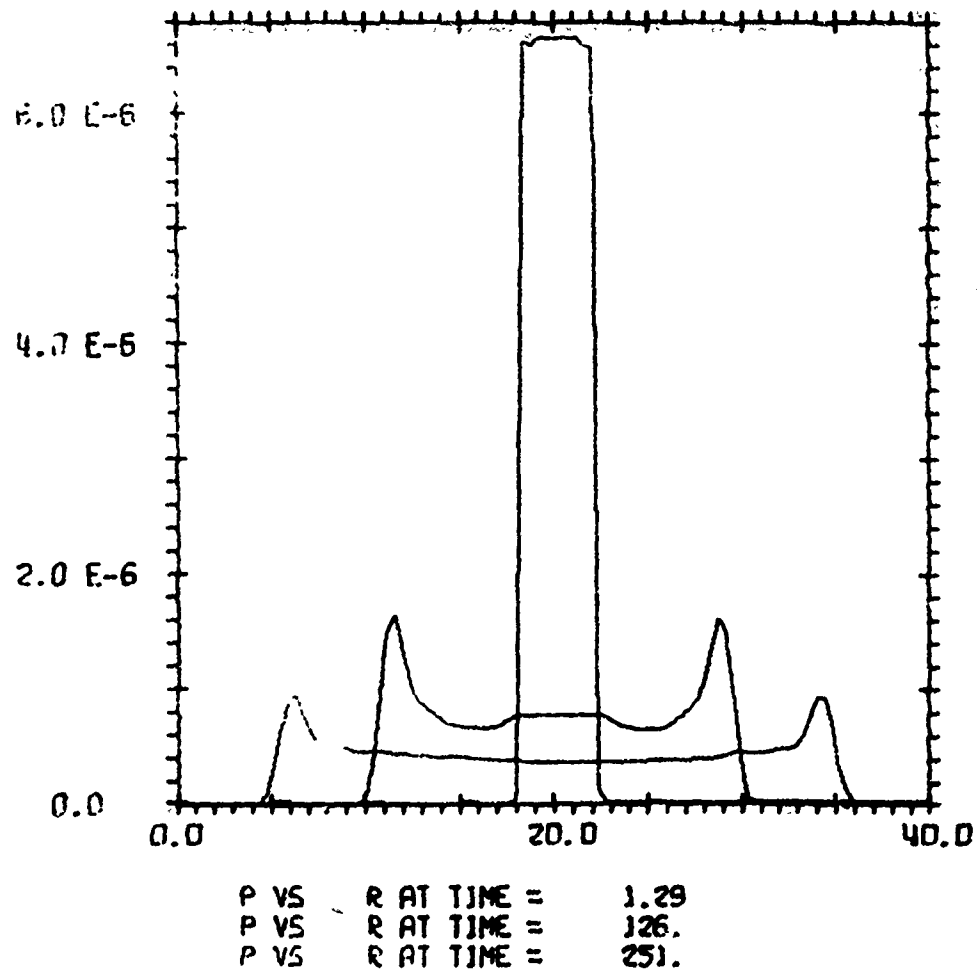


Figure 3a

TCAN 73-14

EULER LAGRANGE - FLUX TEST B - LAGRANGE

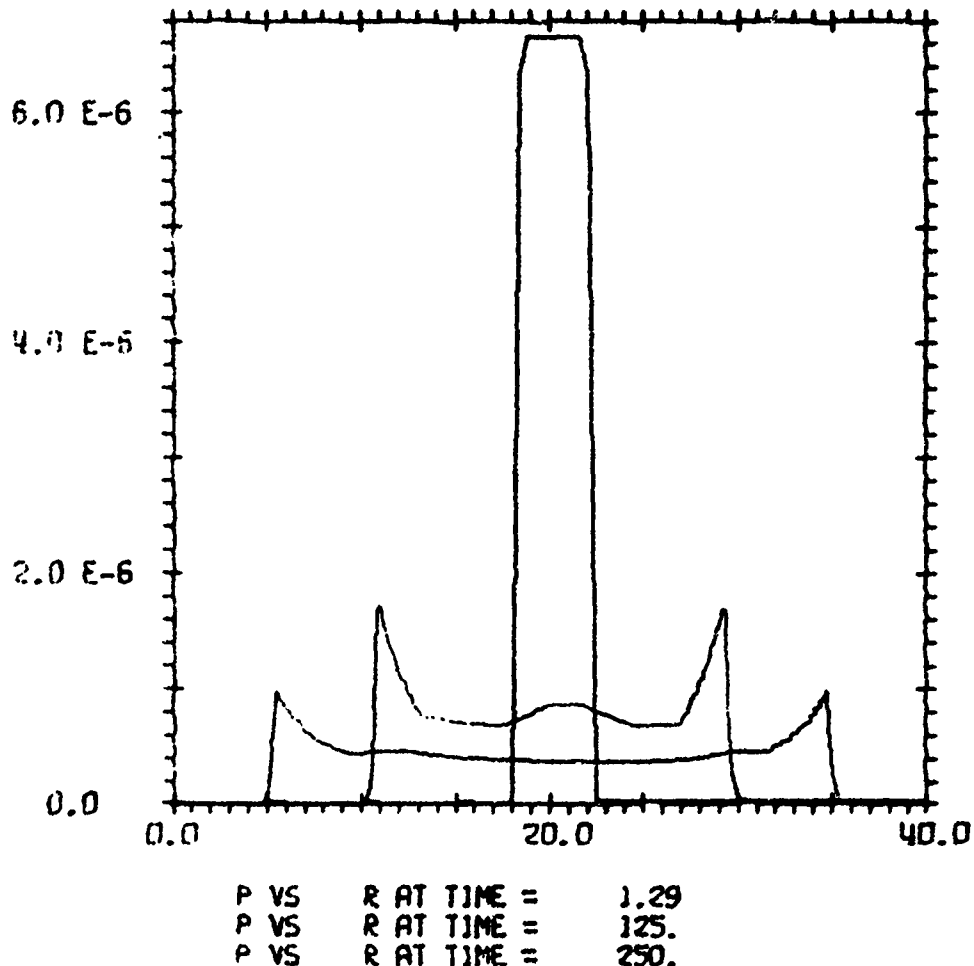
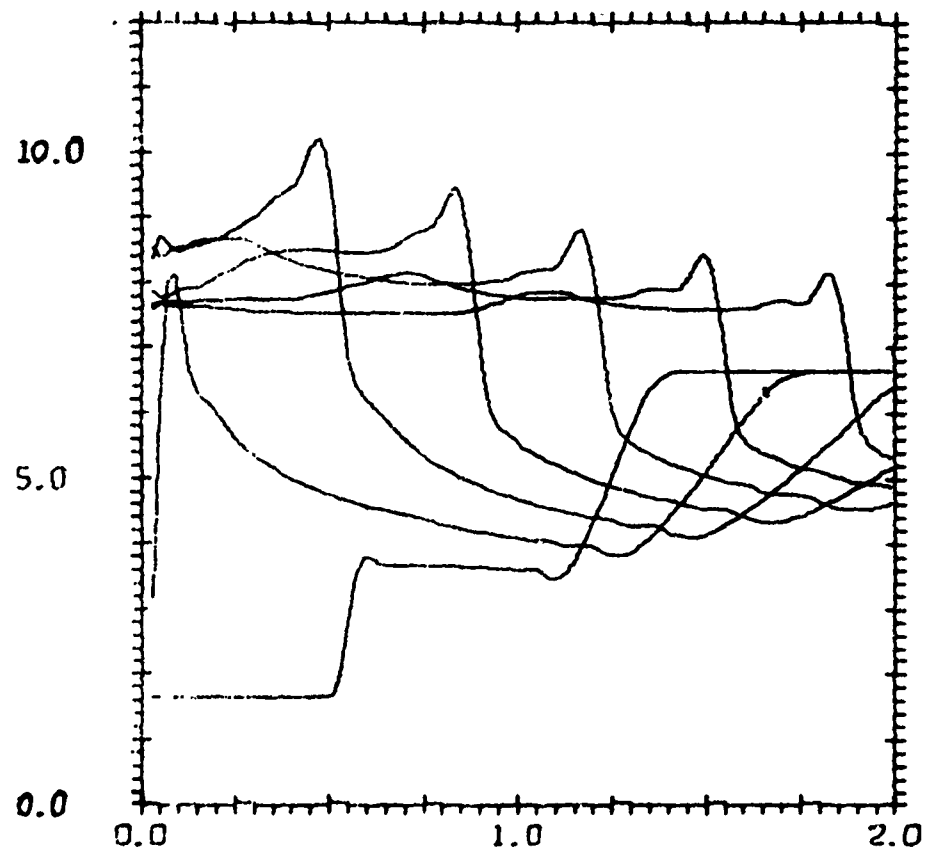


Figure 3b

TCAN 73-14

STELLARINEARICL IMPLOSION -- PATNES PROBLEM EULER

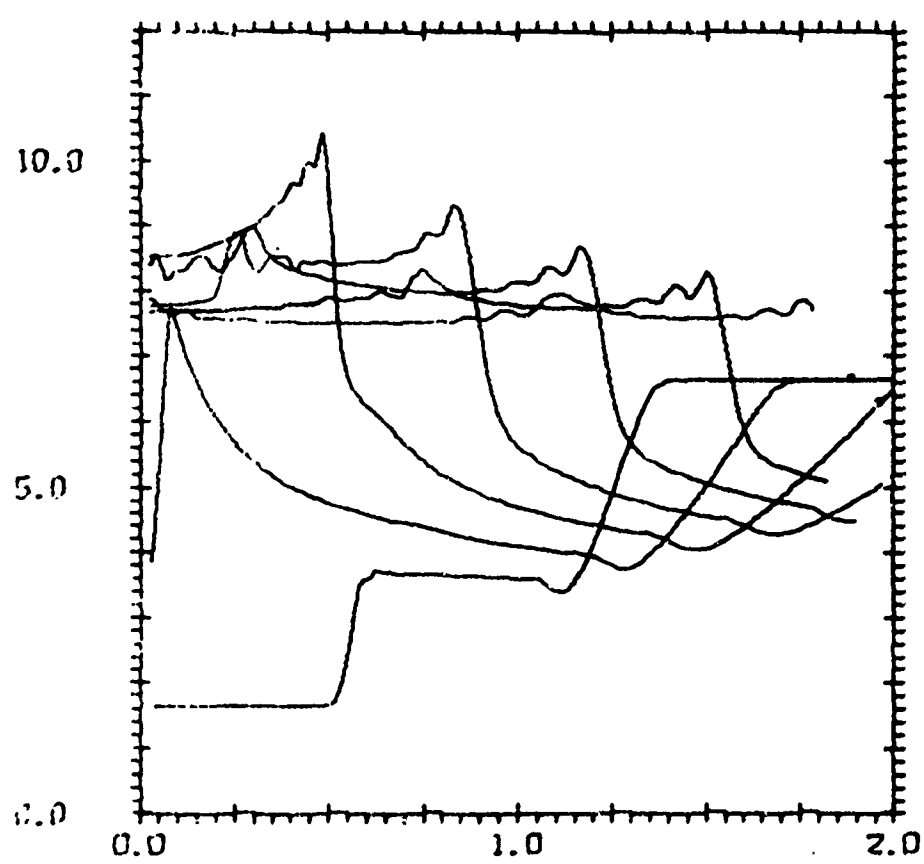


P VS	R AT TIME =	.202
P VS	R AT TIME =	.400
P VS	R AT TIME =	.603
P VS	R AT TIME =	.802
P VS	R AT TIME =	1.00
P VS	R AT TIME =	1.20
P VS	R AT TIME =	1.40

Figure 4a

TCALL 73-14

CYLINDRICAL IMPLOSION -- PAYNES PROBLEM LAGRANGE



P VS	R AT TIME =	.202
P VS	R AT TIME =	.400
P VS	R AT TIME =	.601
P VS	R AT TIME =	.802
P VS	R AT TIME =	1.00
P VS	R AT TIME =	1.20
P VS	R AT TIME =	1.40

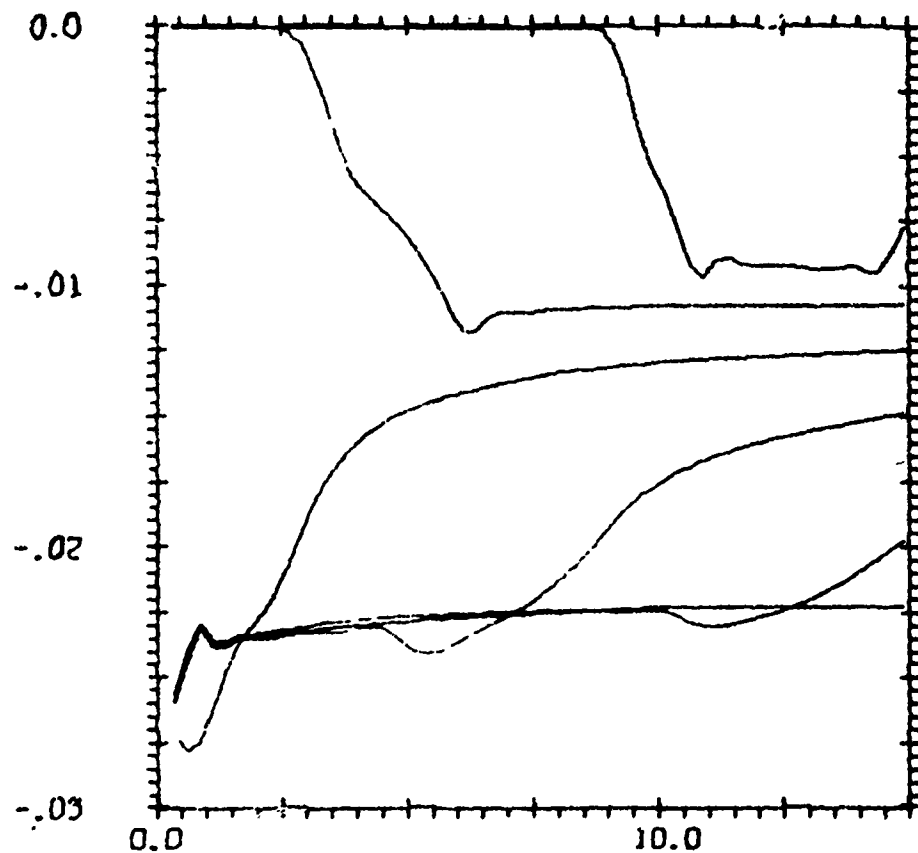
Figure 4b

A - 23



ICAR 73-14

FULTERIAN ELASTIC PLASTIC CYLINDRICAL PLATE IMPACT

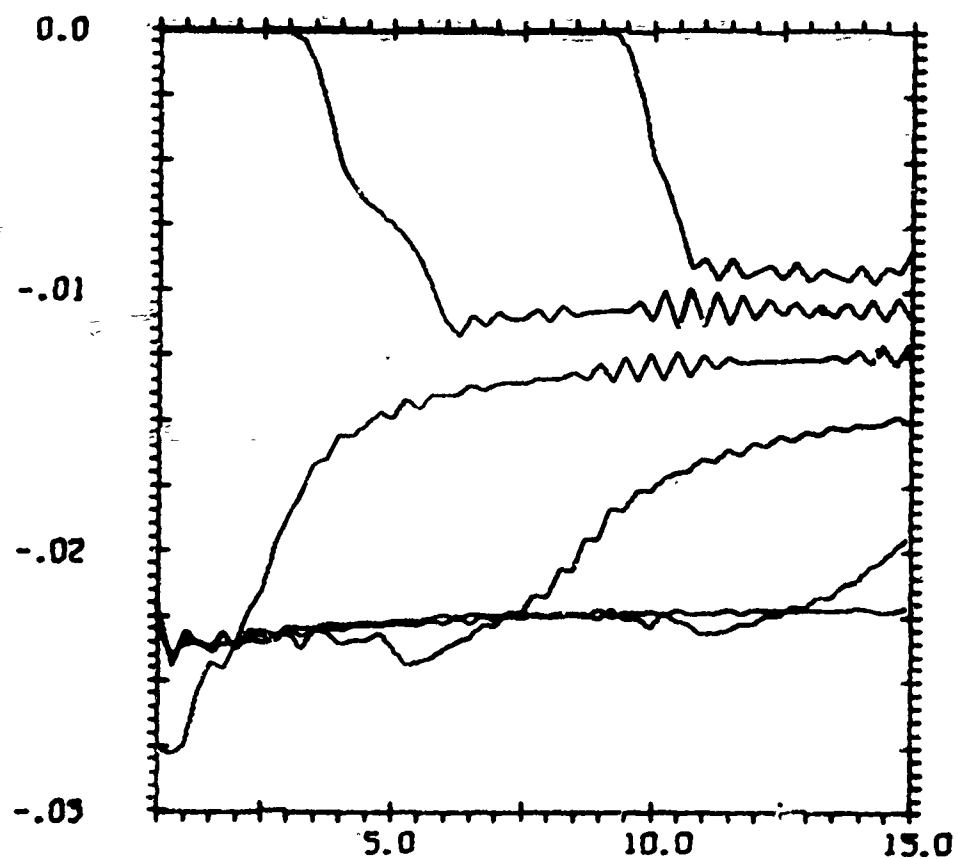


SIGR VS	R AT TIME =	5.05
SIGR VS	R AT TIME =	15.1
SIGR VS	R AT TIME =	25.1
SIGR VS	R AT TIME =	35.1
SIGR VS	R AT TIME =	45.1
SIGR VS	R AT TIME =	55.1

Figure 5a

TCAM 73-14

LAGRANGE ELASTIC PLASTIC CYLINDRICAL PLATE IMPACT

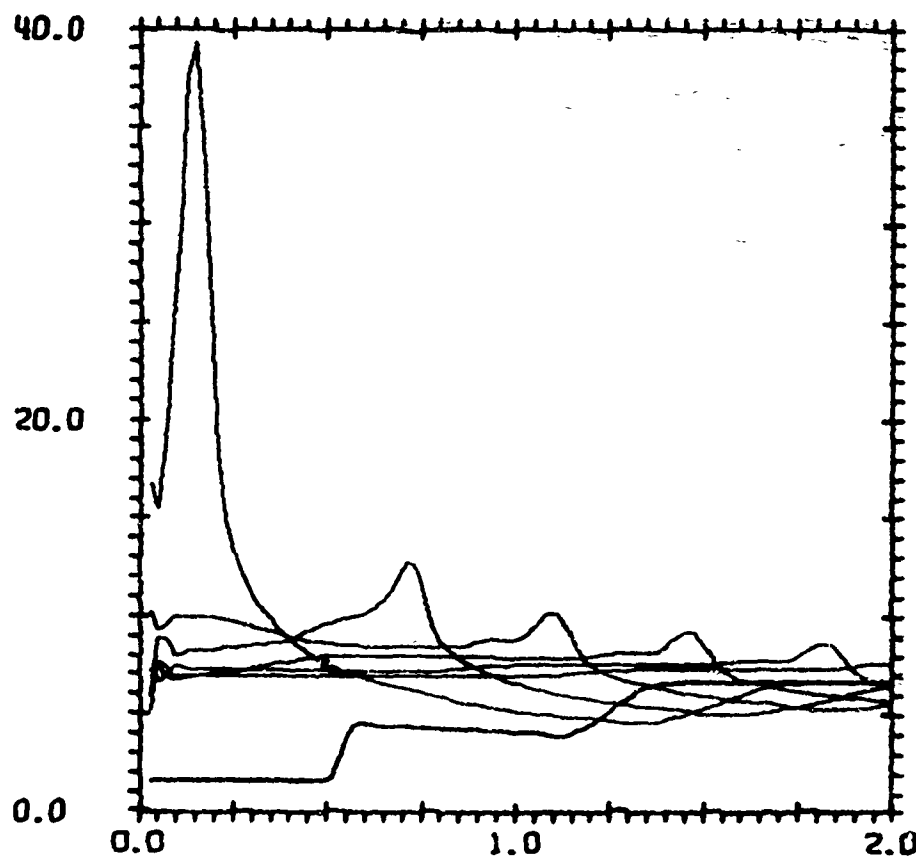


SIGR VS	R AT TIME =	5.05
SIGR VS	R AT TIME =	13.1
SIGR VS	R AT TIME =	25.1
SIGR VS	R AT TIME =	55.1
SIGR VS	R AT TIME =	45.1
SIGR VS	R AT TIME =	55.1

Figure 5b

TCAN 73-14

SPHERICAL IMPLOSION -- EULERIAN

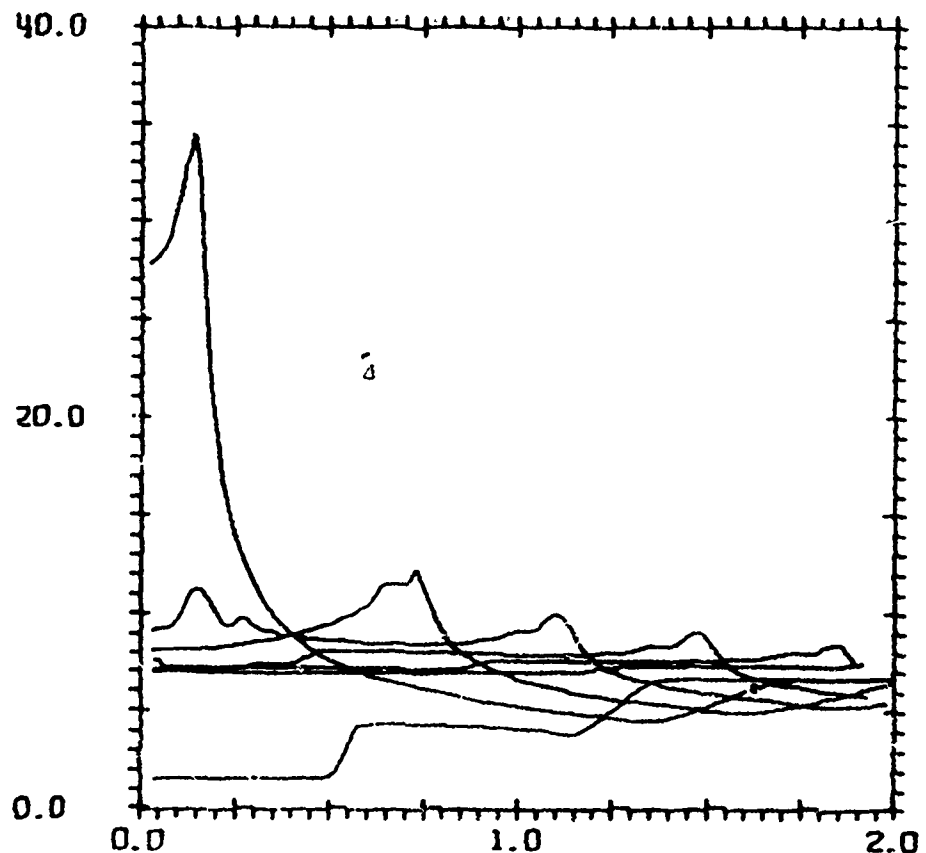


P VS	R AT TIME =	.201
P VS	R AT TIME =	.400
P VS	R AT TIME =	.600
P VS	R AT TIME =	.802
P VS	R AT TIME =	1.00
P VS	R AT TIME =	1.20
P VS	R AT TIME =	1.40

Figure 6a

TCAM 73-14

SPHERICAL IMPLOSION -- LAGRANGE

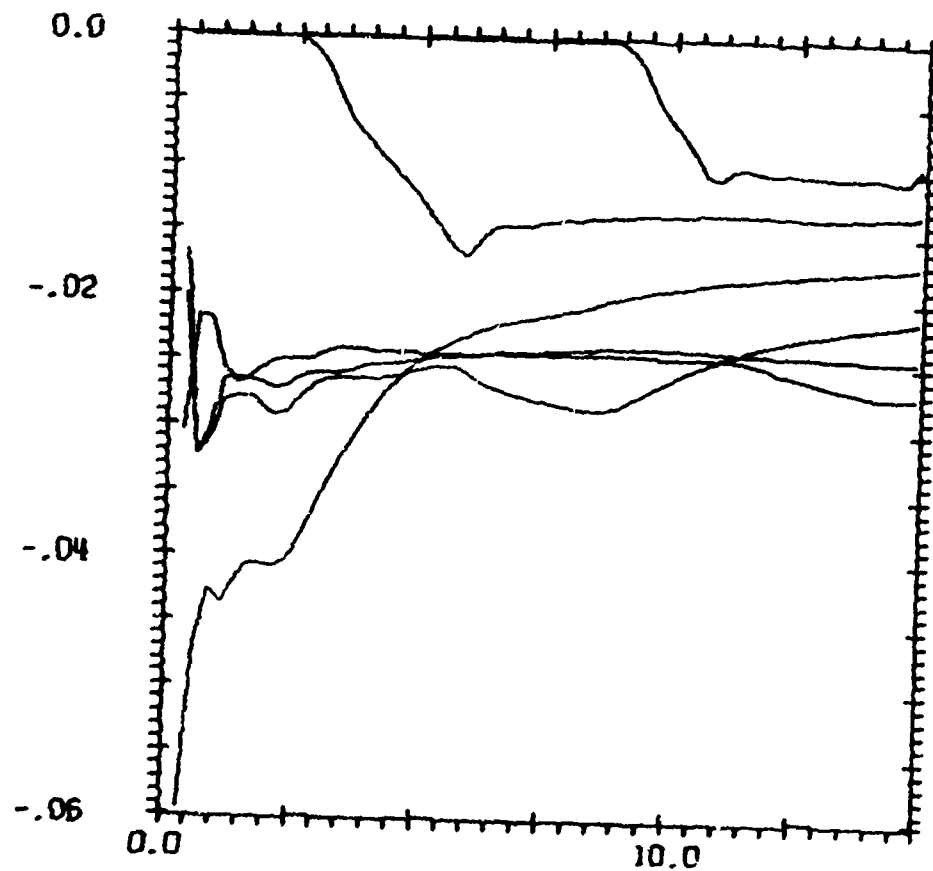


P VS R AT TIME = .201
P VS R AT TIME = .400
P VS R AT TIME = .601
P VS R AT TIME = .801
P VS R AT TIME = 1.00
P VS R AT TIME = 1.20
P VS R AT TIME = 1.40

Figure 6b

TCAM 73-14

EULERIAN ELASTIC PLASTIC SPHERICAL PLATE IMPACT



SIGR VS	R AT TIME =	5.05
SIGR VS	R AT TIME =	15.1
SIGR VS	R AT TIME =	25.1
SIGR VS	R AT TIME =	35.1
SIGR VS	R AT TIME =	45.1
SIGR VS	R AT TIME =	55.1

Figure 7a

TCAM 73-14

LAGRANGE ELASTIC PLASTIC SPHERICAL PLATE IMPACT

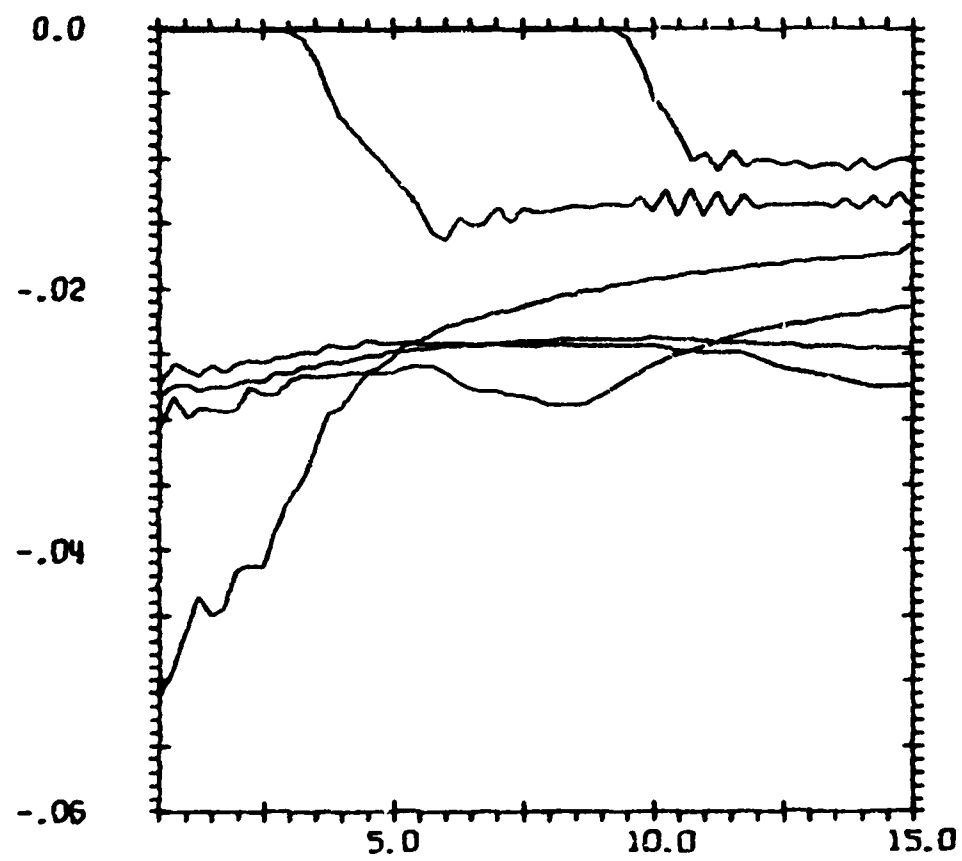


Figure 7b

SECTION 5
CONCLUDING REMARKS

1. The PISCES 1DE and the PISCES 1DL codes have been shown to be of comparable accuracy when each uses the same number of zones. However, since for many problems over twice as many cycles are used by PISCES 1DL to run to the same problem time, usually, PISCES 1DE is often much more cost effective than using PISCES 1DL.
2. The PISCES 1DE code could and should be extended in the near future to accurately handle more than one material in a given problem. The material interface must be treated in a second-order manner consistent with the accuracy of the rest of the calculation. Once this is accomplished, the PISCES 1DE code will have virtually all of the capabilities of the PISCES 1DL code and may be used to solve a wide class of problems that have traditionally been considered to be strictly Lagrangian in nature.
3. Once the material interface problem has been solved for one dimension, serious thought should be given toward extending this computational method to two and three dimensions. The accuracy of the elastic-plastic calculation combined with the inherent ability of an Eulerian code to handle problems involving large deformations should make this method an extremely useful computational tool for multi-dimensional calculations. It should be able to accurately compute phenomena which have heretofore been amenable only to a coupled Eulerian-Lagrangian computer code.

REFERENCES

1. Wilkins, M. L., "Calculation of Elastic-Plastic Flow," UCRL-7322, Rev. 1, January, 1969.
2. MacCormack, R. W., "The Effect of Viscosity in Hypervelocity Impact Cratering," AIAA Paper No. 69-354, May, 1969.
3. Jardin, S. C., "A Numerical Investigation of Unsteady Magnetogasdynamics," S.M. Thesis, Massachusetts Institute of Technology, June 1973.
4. Roache, P. J., Computational Fluid Dynamics, Hermosa Publishers, Albuquerque, N.M. (1972).
5. Richtmyer, R. D. and Morton, K. W., Difference Methods for Initial Value Problems, 2nd ed., Interscience Publishers, New York (1967).
6. Payne, R. B., "A Numerical Method for a Converging Cylindrical Shock," J. of Fluid Mechanics, (2)p. 185 (1957).
7. Lapidus, A., "Computation of Radially Symmetric Shocked Flows," J. of Computational Physics, (8), 1, p. 106 (1971)

APPENDIX A
ACCURACY AND STABILITY OF THE DIFFERENCE EQUATIONS

The accuracy and stability of finite-difference methods such as those previously described cannot be completely analyzed in the general non-linear form. The method of analysis we will use is to first linearize the set of differential equations (1) (with the vector \vec{R} absent) and then to study the amplification of Fourier components of the solution by the difference method applied to the linearized set.

The set of equations we will analyze is

$$\frac{\partial}{\partial t} \vec{U} + \vec{A} \frac{\partial}{\partial x} \vec{U} = \rho \mu \vec{B} \frac{\partial}{\partial x} \vec{U} \quad (A-1)$$

where \vec{A} and \vec{B} are the Jacobian matrices of \vec{F} and \vec{G} with respect to \vec{U} and are considered to be constant.

$$\vec{A} = \begin{bmatrix} 0 & 1 & 0 & 0 & 0 \\ -\frac{m^2}{\rho^2} + \frac{\partial p}{\partial \rho} + \frac{S}{\rho^2} & \frac{2m}{\rho} + \frac{\partial p}{\partial m} & \frac{\partial p}{\partial \epsilon} & -\frac{1}{\rho} & 0 \\ \frac{m}{\rho^2} \left[\rho \frac{\partial p}{\partial \rho} - \epsilon - p + 2 \frac{S}{\rho} \right] & \frac{1}{\rho} \left[\epsilon + p - \frac{S}{\rho} + m \frac{\partial p}{\partial m} \right] & \frac{m}{\rho} \left(1 + \frac{\partial p}{\partial \epsilon} \right) & -\frac{m}{\rho} & 0 \\ -\frac{m}{\rho^2} S & \frac{S}{\rho} & 0 & \frac{m}{\rho} & 0 \\ -\frac{m}{\rho^2} T & \frac{T}{\rho} & 0 & 0 & \frac{m}{\rho} \end{bmatrix}$$

TCAM 73-14

$$\vec{B} = \begin{bmatrix} 0 & 0 & 0 & 0 & 0 \\ 0 & 0 & 0 & 0 & 0 \\ 0 & 0 & 0 & 0 & 0 \\ -\frac{4}{3} \frac{m}{\rho^3} & \frac{4}{3} \frac{1}{\rho} & 0 & 0 & 0 \\ \frac{2}{3} \frac{m}{\rho^3} & -\frac{2}{3} \frac{1}{\rho} & 0 & 0 & 0 \end{bmatrix}$$

Application of the difference method to the set (A-1) gives

$$\vec{U}_j^* = \vec{U}_j^n - \frac{\Delta t}{\Delta x} \vec{A} \left[\vec{U}_{j+1}^n - \vec{U}_j^n \right] + \rho \mu \frac{\Delta t}{\Delta x} \vec{B} \left[\vec{U}_{j+1}^n - \vec{U}_j^n \right]$$

$$\vec{U}_j^{n+1} = \frac{1}{2} \left[\vec{U}_j^* + \vec{U}_j^n - \frac{\Delta t}{\Delta x} \vec{A} \left[\vec{U}_j^* - \vec{U}_{j-1}^* \right] + \rho \mu \frac{\Delta t}{\Delta x} \vec{B} \left[\vec{U}_j^* - \vec{U}_{j-1}^* \right] \right]$$

Next, rewrite, letting $\vec{C} = \vec{A} - \rho \mu \vec{B}$

$$\vec{U}_j^* = \vec{U}_j^n - \frac{\Delta t}{\Delta x} \vec{C} \left(\vec{U}_{j+1}^n - \vec{U}_j^n \right)$$

$$\vec{U}_j^{n+1} = \frac{1}{2} \left[\vec{U}_j^* + \vec{U}_j^n - \frac{\Delta t}{\Delta x} \vec{C} \left(\vec{U}_j^* - \vec{U}_{j-1}^* \right) \right]$$

and convert to a one-step difference method by substitution,

$$\vec{U}_j^{n+1} = \vec{U}_j^n - \frac{\Delta t}{2 \Delta x} \vec{C} \left[\vec{U}_{j+1}^n - \vec{U}_{j-1}^n \right] + \frac{1}{2} \left(\frac{\Delta t}{\Delta x} \right)^2 \vec{C}^2 \left[\vec{U}_{j+1}^n - 2 \vec{U}_j^n + \vec{U}_{j-1}^n \right] \quad (A-2)$$

Truncation error

The truncation error of the difference approximation (A-2) to the equation (A-1) is readily obtained from Taylor's series expansions. Thus, letting

$$\vec{U}_j^{n+1} = \vec{U}_j^n + \Delta t \frac{\partial \vec{U}}{\partial t} + \frac{(\Delta t)^2}{2} \frac{\partial^2 \vec{U}}{\partial t^2} + \dots$$

$$\vec{U}_{j+1}^n = \vec{U}_j^n + \Delta x \frac{\partial \vec{U}}{\partial x} + \frac{(\Delta x)^2}{2} \frac{\partial^2 \vec{U}}{\partial x^2} + \dots$$

and using the differential equation

$$\frac{\partial \vec{U}}{\partial t} = -C \frac{\partial \vec{U}}{\partial x}$$

to eliminate higher order time derivatives in favor of spatial derivatives, the difference equation (A-2) can be shown to be equivalent to the equation

$$\frac{\partial \vec{U}}{\partial t} + C \frac{\partial \vec{U}}{\partial x} = \vec{T}_\Delta$$

where the leading terms of the truncation error \vec{T}_Δ are

$$\vec{T}_\Delta = -\frac{\vec{C}}{3!} \left[(\Delta x)^2 - \vec{C}^2 (\Delta t)^2 \right] \frac{\partial^3 \vec{U}}{\partial x^3} + \frac{\vec{C}^2 \Delta t}{4!} \left[(\Delta x)^2 - \vec{C}^2 (\Delta t)^2 \right] \frac{\partial^4 \vec{U}}{\partial x^4} + \dots$$

It is interesting to note that this method would be exact (i.e., zero truncation error) if $C = \frac{\Delta x}{\Delta t} I$ where I is the identity matrix. The leading term in the truncation error is seen to be responsible for dispersion while the second term causes dissipation.

Stability

We investigate the effect of the difference equation (A-2) on a single Fourier component of the solution by making the substitution

$$\tilde{U}_j^n \rightarrow \tilde{U} r^n e^{ikj \Delta x} \quad (A-3)$$

where \tilde{U} is the amplitude vector of this Fourier component, $i = \sqrt{-1}$, k is the wave number, and $r^n = e^{i\omega n \Delta t}$ is the growth factor. The stability criterion will be that $|r| \leq 1$. If this condition is satisfied, no harmonic is amplified at all, whereas if it is violated, there is some harmonic that is amplified without limit as n increases.

Making the substitution (A-3) into (A-2) yields, after simplification,

$$r \tilde{U} = \left\{ I - i \frac{\Delta t}{\Delta x} C \sin(k \Delta x) + \frac{\Delta t^2}{\Delta x^2} C^2 \left[\cos(k \Delta x) - 1 \right] \right\} \cdot \tilde{U}$$

or, upon defining the "amplification matrix" Z by

$$Z = I - i \frac{\Delta t}{\Delta x} C \sin(k \Delta x) + \left(\frac{\Delta t}{\Delta x} \right)^2 C^2 \left[\cos(k \Delta x) - 1 \right]$$

we have

$$\{r I - Z\} \cdot \tilde{U} = 0$$

A unique solution will exist only if the determinant of the matrix in brackets vanishes, i.e.,

$$\det\{r I - Z\} = 0 \quad (A-4)$$

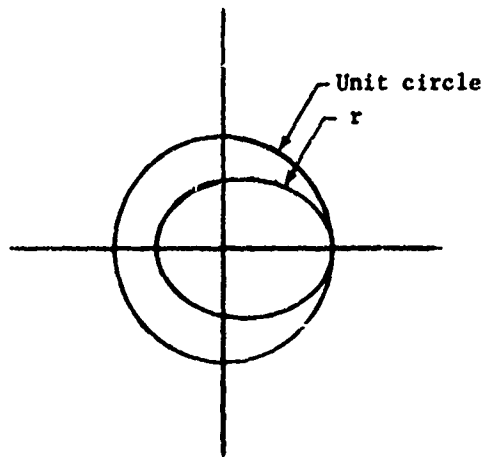
This is equivalent to the statement that r must equal one of the eigenvalues of the matrix \tilde{Z} . The eigenvalues of the matrix \tilde{Z} may be expressed in terms of the eigenvalues of the matrix \tilde{C} by making use of the Spectral Mapping Theorem which states that if $\tilde{Z} = f(\tilde{C})$ is a rational function of the matrix \tilde{C} and λ_c are the eigenvalues of \tilde{C} , then $f(\lambda_c)$ are the eigenvalues of \tilde{Z} . Thus,

$$r = 1 - i \lambda_c \frac{\Delta t}{\Delta x} \sin(k\Delta x) + \left(\frac{\Delta t}{\Delta x} \right)^2 \lambda_c^2 [\cos(k\Delta x) - 1]$$

taking the square of the absolute magnitude and imposing the condition $|r| \leq 1$ gives the requirement

$$|r|^2 = \left[1 + \left(\frac{\lambda_c \Delta t}{\Delta x} \right)^2 [\cos(k\Delta x) - 1] \right]^2 + \left(\frac{\lambda_c \Delta t}{\Delta x} \right)^2 \sin^2(k\Delta x) \leq 1$$

This is seen to trace out an ellipse in the complex plane as $(k\Delta x)$ varies from 0 to 2π .



The stability requirement can now be seen to be that the unit circle encompasses this ellipse. This is equivalent to the condition

$$\left| \frac{\lambda_c \Delta t}{\Delta x} \right| < 1 \quad (A-5)$$

This relation must hold for each of the eigenvalues of \tilde{C} .

To complete our analysis we must next find the eigenvalues of the matrix \tilde{C} . These are given by the equation

$$\det\{\tilde{C} - \lambda_c \tilde{I}\} = 0$$

or,

$$\begin{vmatrix} -\lambda_c & 1 & 0 & 0 & 0 \\ -\frac{m^2}{p^2} + \frac{\partial p}{\partial p} + \frac{s}{p^2} & \frac{2m}{p} + \frac{\partial p}{\partial m} - \lambda_c & \frac{\partial p}{\partial e} & -\frac{1}{p} & 0 \\ -\frac{m}{p^2} \left(n \frac{\partial p}{\partial p} - e - p + 2 \frac{s}{p} \right) & \frac{1}{p} \left(m \frac{\partial p}{\partial m} + e + p - \frac{s}{p} \right) & \frac{m}{p} \left(1 + \frac{\partial p}{\partial e} \right) - \lambda_c & -\frac{m}{p^2} & 0 \\ -\frac{m}{p^2} s + \frac{4}{3} \mu \frac{m}{p} & \frac{s}{p} - \frac{4}{3} \mu & 0 & \frac{m}{p} - \lambda_c & 0 \\ -\frac{m}{p^2} T - \frac{2}{3} \mu \frac{m}{p} & \frac{T}{p} + \frac{2}{3} \mu & 0 & 0 & \frac{m}{p} - \lambda_c \end{vmatrix} = 0 \quad (A-6)$$

(A-6)

It is easiest to evaluate this determinant by going back to the primitive variables ρ , $u = m/\rho$, $e = (\epsilon/\rho) - u^2/2$, and $s_1 = s/\rho$. Making use of the relations

$$\frac{\partial p}{\partial \epsilon} = \frac{\partial p}{\partial e} \frac{\partial e}{\partial \epsilon} = \frac{1}{\rho} \frac{\partial p}{\partial e}$$

$$\frac{\partial p}{\partial m} = \frac{\partial p}{\partial e} \frac{\partial e}{\partial m} = - \frac{m}{\rho^2} \frac{\partial p}{\partial e} = - \frac{u}{\rho} \frac{\partial p}{\partial e}$$

$$\frac{\partial p}{\partial \rho} = \frac{\partial p}{\partial \rho}|_e + \frac{\partial p}{\partial e} \frac{\partial e}{\partial \rho} = \frac{\partial p}{\partial \rho} + \left(-\frac{\epsilon}{\rho^2} + \frac{u^2}{\rho^2} \right) \frac{\partial p}{\partial e} = \frac{\partial p}{\partial \rho} + \left(-\frac{e}{\rho} + \frac{u^2}{2\rho} \right) \frac{\partial p}{\partial e}$$

Equation (A-6) can be factored to give

$$(\lambda_c - u)^3 \left[\lambda_c^2 - 2u\lambda_c + u^2 - \frac{4\mu}{3\rho} - \frac{\partial p}{\partial \rho} - \frac{1}{\rho^3} \frac{\partial p}{\partial e} (p - s_1) \right] = 0$$

Thus three of the eigenvalues of the matrix \bar{C} are degenerate and are equal to the particle velocity u . The other two are obtained by solving the above quadratic. This gives

$$\lambda_c = \begin{Bmatrix} u \\ u \\ u \\ u+c \\ u-c \end{Bmatrix} \quad (A-7)$$

where

$$c^2 = \frac{\partial p}{\partial \rho} + \frac{1}{\rho^2} \frac{\partial p}{\partial e} (p - s_1) + \frac{4\mu}{3\rho} \quad (A-8)$$

The quantity c is seen to be the sonic velocity for a general equation

TCAM 73-14

of state $p = p(\rho, e)$. To verify this, we look at two example equations of state.

Example 1: Ideal Gas

In this case, $p = (\gamma - 1)\rho e$, $\mu = 0$, $s_1 = 0$, and the expression for c^2 reduces to the well known formula

$$c^2 = \frac{\gamma p}{\rho}$$

Example 2: Linear Elastic

The equation of state for linear elasticity is $p = K\left(\frac{\rho}{\rho_0} - 1\right)$, where K is the bulk modulus. Substitution of this into Eq. (A-8) gives

$$c^2 = \frac{1}{\rho_0} K + \frac{4\mu}{3\rho}$$

which is the formula for the propagation velocity of a longitudinal wave in an elastic medium.

We are now in a position to state the complete linearized stability criterion. Substituting each of the eigenvalues in Eq. (A-7) into (A-5) and selecting the most restrictive gives the stability criterion

$$\Delta t \leq \frac{\Delta x}{|u| + c}$$

where c is given by Eq. (A-8). This is seen to be just the (CLF) stability criterion (Reference 5).

APPENDIX B
INPUT

The PISCES IDE code is input exactly the same as the PISCES IDL code with the following exceptions and/or restrictions.

1. A single TYPE 57 card must be input with the number 1.0 in the first field. This tells the code to do an Eulerian rather than a Lagrangian calculation.
2. Only one material type is allowed in a problem and it must have material number 1.
3. The Boundary Options card (TYPE 41) must be included in the input but it is ignored by the code. Standard boundary conditions, unless otherwise supplied are:

LEFT BOUNDARY: Kept at initial conditions for plane and flume symmetries, symmetry axis for cylindrical and spherical symmetries.

RIGHT BOUNDARY: Zero gradients at grid point (JMAX - 1)

4. Yield models based on the distortional energy may not be used as the distortional energy is not explicitly calculated by the code.
5. The shear modulus is assumed to be constant and to be equal to G0.
6. The input parameter DISL must always be included, but it is ignored for cylindrical or spherical symmetry problems.

Instead, DISL is computed by the code so that the first two grid points are centered about the symmetry point. The values at the first grid point are then not to be interpreted as being physical, but are chosen to provide a "symmetry" boundary condition.

7. The code has perhaps its greatest usefulness in calculating "moving wall flume" ($NSWD = 5$) problems. In these calculations, Subroutine MOVWAL is not called as it is in PISCES IDL. Instead, the user must supply a Subroutine AREE(AT,AX,AI,DH) which is called twice for each zone for each cycle. The variables AI and DH are not presently used by the code. (These should be set to 1.0 in the subroutine.) The variable AT must return the derivative of the area at zone J with respect to the time, divided by the area. Similarly, the variable AX must return the derivative of the area at zone J with respect to r, divided by the area. For the method to be fully second order, these derivatives must be evaluated at time n on the first call and time n+1 on the second call.

APPENDIX B
PISCESTM IDL
MANUAL A

B- II

CONTENTS

GENERAL DESCRIPTION	1
Equations of Motion	1
Constitutive Equations	3
Boundary and Initial Conditions	4
Void Option	5
Special File Option	5
Flume Option	5
Static Option	5
Extending Rezone Option	5
Microzone Option	6
Heat Flow Option	6
Restart Option	6
Data Display Option	6
FINITE-DIFFERENCE EQUATIONS	7
APPENDIX A: Derivation of Equation of Motion in Flume Symmetry	23
APPENDIX B: Relations Between Measures of Volume Change	25
APPENDIX C: The q Stability Criterion	27
APPENDIX D: Accuracy of the Pressure-Energy Iteration	31
APPENDIX E: Relation Between ϵ_r , ϵ_l and Compression in Plane, Cylindrical and Spherical Geometry	33
APPENDIX F: Formulae for Sound Speed in Elastic-Plastic Material	37

GENERAL DESCRIPTION

EQUATIONS OF MOTION

PISCES IDL is a one-dimensional, time-dependent finite-difference Lagrange code which is used to calculate the dynamic motion of continua including elastic-plastic and hydrodynamic media. The differential equations that govern the motions of these media are approximated by difference equations applied to a network of zones that describe the physical space occupied by the media. Groups of contiguous zones of the same material are described by constitutive equations which are coupled to the equations of motion. Time is also discretized and its formulation insures stable difference equations. The Lagrangian formulation of the differential equations requires that each zone contain a constant mass element of material that moves and distorts in space and time, the motion for all the zones approximating the continuum motion. In a one-dimensional formulation only one space variable exists, symmetry considerations account for the other two. There are three possible symmetries plane, cylindrical, and spherical. In plane symmetry, zones are infinite slabs and the thickness of a slab is the zone size. In cylindrical symmetry, zones are concentric hollow cylinders of infinite length. Spherically symmetric zones are concentric hollow spheres. In both of these latter geometries, zonal widths are radial thicknesses of the cylinders and spheres, respectively. The partial differential equations that govern the motions in PISCES IDL are shown on the following pages.

Momentum Equations

Plane symmetry

$$\rho \ddot{r} = \frac{\partial \Sigma}{\partial r}$$

Cylindrical symmetry

$$\rho \ddot{r} = \frac{\partial \Sigma_r}{\partial r} + \frac{\Sigma_r - \Sigma_t}{r}$$

Spherical symmetry

$$\rho \ddot{r} = \frac{\partial \Sigma_r}{\partial r} + 2 \frac{\Sigma_r - \Sigma_t}{r}$$

Continuity Equations

Plane symmetry

$$\frac{\dot{V}}{V} = \frac{\partial \dot{r}}{\partial r}$$

IDL-A

Cylindrical symmetry

$$\frac{\dot{V}}{V} = \frac{\partial \dot{r}}{\partial r} + \frac{\dot{r}}{r}$$

Spherical symmetry

$$\frac{\dot{V}}{V} = \frac{\partial \dot{r}}{\partial r} + 2 \frac{\dot{r}}{r}$$

Energy Equations

Plane symmetry

$$\dot{E} = -(p + q)\dot{V} + V \left(s_r \frac{\partial \dot{r}}{\partial r} \right) + \dot{H}$$

Cylindrical symmetry

$$\dot{E} = -(p + q)\dot{V} + V \left(s_r \frac{\partial \dot{r}}{\partial r} + s_t \frac{\dot{r}}{r} \right) + \dot{H}$$

Spherical symmetry

$$\dot{E} = -(p + q)\dot{V} + V \left(s_r \frac{\partial \dot{r}}{\partial r} + 2s_t \frac{\dot{r}}{r} \right) + \dot{H}$$

where

ρ \equiv mass density

r \equiv independent coordinate

\dot{r} \equiv velocity of independent coordinate

\ddot{r} \equiv acceleration of independent coordinate

s_r \equiv normal r stress $= s_r - (p + q)$

s_t \equiv tangential t stress $= s_t - (p + q)$

s_r \equiv r stress deviator

s_t \equiv t stress deviator

p ≡ hydrostatic pressure

q ≡ artificial viscosity

v ≡ relative volume ≡ $\frac{\rho_0}{\rho}$, ρ_0 ≡ reference density

E ≡ internal energy per original volume, \dot{H} ≡ heat flow.

In the equations of motion the position and velocity of a particular zone are defined at the zone corners (grid points that define the zonal boundary) while other variables such as pressure, stress, energy, etc., are defined as averages over the zonal interior. These differential equations are approximated by the finite-difference equations developed by Wilkins (Reference 1).

CONSTITUTIVE EQUATIONS

Besides the equations of motion it is necessary to have constitutive equations that describe the media. These material description equations are the equations of state, stress-strain models and transport property descriptions. In general, these functional relationships may take any form—discontinuous functions as well as tables are used to describe phase changes, hysteresis, cracking, etc.

The equations of state calculate pressure from the density and the total internal energy density of a zone in a two-step iteration. The interim internal energy density is evaluated from the old internal energy density, the new heat flux, the old pressure, and the new change of volume in the zone. This first approximation of the internal energy density is then used in the equation of state to get a first approximation of the new pressure. A revised estimate of the internal energy density comes from this first approximation of the new pressure and the new distortional energy density. Finally, the new pressure in a zone is determined from the second approximation to the internal energy density. In this way a simultaneous solution of the constitutive relations and the second law of thermodynamics is effected independently of the form of the equation of state.

An example of an available stress-strain model is the so-called elastic-plastic yield stress model. A yield stress model is a law that regulates the stress deviators. In a calculation, the stresses are decomposed into a hydrostatic component and a deviatoric component. The stress deviator describes the resistance of the material to shear distortion and is calculated in terms of an incremental stress resulting from an incremental strain. The deviators are limited by the yield stress according to some rule that describes the elastic-plastic behavior of the material. In this model, the deviatoric behavior of materials is determined by the shear modulus and the yield stress. (For a fluid, both are zero.) A temperature-dependent shear modulus is available and should be chosen to be consistent with the bulk modulus and Poisson's ratio for the material. The yield stress is defined as the stress at the yielding point in a uniaxial stress test and may be dependent on thermodynamic variables. For example, the code has available work-hardening models in which yield stress is a function of distortional energy. Mohr-Coulomb models in which

IDL-A

yield stress is a function of pressure, von Mises models in which yield stress is a constant, stress relaxation models based on dislocation motion, and temperature-dependent models in which yield stress is a function of internal energy.

Energy transport via Fourier's law of heat conduction is available. Specific heat and conductivity may be functions of temperature.

BOUNDARY AND INITIAL CONDITIONS

Time-dependent pressure profiles as well as time-dependent velocity profiles (pistons) can be automatically applied to either boundary. Fixed and free boundary conditions are merely sub-cases of the above capabilities. Energy boundary conditions are specified by applying temperature and heat flux histories at the appropriate boundaries. Internal or kinetic energy can be deposited into any region as an initial condition. Time- and space-dependent energy deposition and a zone-by-zone detonation description may be included in the solution of a problem as required. The code logic simulates a Chapman-Jouguet detonation.

Once the geometry, material properties, initial conditions, and boundary conditions are specified, the calculation of the problem is ready to proceed

The first time step that the problem takes must be specified, but from that point on, the code automatically calculates the subsequent time steps according to stability criteria imposed by the finite-difference equations. Physically, the restriction imposed on the calculation is that no signal may cross a zone in one time step so that a zone reacts only to activity being transmitted from a neighboring zone.

The accuracy of the solution in a Lagrangian code depends on the density of zones. With coarse zoning, gross features of the solution such as total energy and momentum in a region may be realistic, but the actual values of a variable at a point are apt to be in error. The resolution in both space and time is proportional to the zone size. A strong shock is handled by the finite-difference equations by using Von Neumann's artificial quadratic viscosity (Reference 2), which is introduced to spread any shock front over a distance of about three zones. Zone-to-zone noise may be smoothed by an artificial linear viscosity logic.

PISCES IDL contains several options that are worth special mention. Among these are the void, remap, flume, static, extending rezone, microzone, heat flow, restart, and data display options. These capabilities are described as follows:

VOID OPTION

Between any two mass regions it is possible to define a void of finite thickness. Motion in these regions can expand or shrink the void. However, once the void is closed, it cannot be reopened. This option is valuable when dealing with particle interaction problems and would probably be useful when dealing with some types of structural response.

SPECIAL FILE OPTION

The special file capability allows information calculated by PISCES IDL to be punched onto computer cards, written onto tape or disk, or stored by any computer resource on its media. This output can be formated in such a way as to be input to another code.

FLUME OPTION

The flume option turns the code into a one-and-one-half-dimensional code by defining a variable area duct as a boundary condition along the direction of flow. The duct may be fixed or free to respond to the flow pressures. In the latter case motion of the duct walls may be programmed to have some pre-described resistance or motion. A real strength wall model is available upon request. For material moving in a direction parallel to a fixed or slowly moving boundary, the flume option may obviate the need for a more expensive two-dimensional calculation. Flume materials must always be fluids while wall materials may be solid.

STATIC OPTION

Nondynamic, equilibrium stress distributions may be computed using PISCES IDL. An input switch changes the time variable to an iteration variable converting the code to a stress diffusion equation solver rather than a stress wave equation code. This option is relatively new but very powerful.

EXTENDING REZONE OPTION

The rezoner allows a user to extend automatically the spatial domain included in a calculation while a problem is in progress. For explosions emanating from a point, line, or plane, the spatial length of the problem is doubled when activity nears the outside boundary. The total number of zones with which the problem starts is held fixed so that the effect of this rezone procedure is that all zones are approximately doubled in size. There is no limit to the number of rezonings that may be allowed in a problem.

IDL-A

but since the accuracy of a solution depends on the zone size, resolution can become poor after several rezonings. Generally, for one-dimensional explosions, this procedure has the advantage of having the finest zoning when it is most necessary.

MICROZONE OPTION

The microzoner is used when fine zoning requirements at a shock front are economically too stringent for the entire grid. This option allows fine zoning to be initially specified only where it is necessary, while coarse zoning is defined elsewhere. Then the code automatically moves the microzoned (finely zoned) region to follow the activity that needs the fine zoning. A single pulse in a slab where the entire pulse is small compared to the width of the slab is an example of a problem that may need the microzoning option.

HEAT FLOW OPTION

Diffusion logic is available to handle heat conduction problems. Fourier's law is coupled to the difference equations of material motion under the assumption that the heat conduction need not be time centered in the energy equation when momentum effects control the time step.

RESTART OPTION

The restart option allows the user to complete a problem in sequential steps. Edits, rezones, boundary conditions, and material parameters may all be redefined at restart time.

DATA DISPLAY OPTION

Automatic plot display is available in PISCES IDL through the PI-PLOTTM Plotting System. The plotting capability allows parametric plots of any variable as a function of any variable at a point in Lagrange space with time as a parameter or at a particular time with laboratory coordinate as a parameter. These plots may be plotted automatically on a Cal Comp incremental or zip-mode plotter, an SC-4020 CRT plotter, or on the printer. In addition, shock front plots (values of a variable at the shock front as a function of distance and time) are available and are plotted on a log-log scale for convenience. Peak value printouts and plots are also available.

Automatic print edits are available as a function of problem time, cycle number and activity front.

FINITE-DIFFERENCE EQUATIONS

The differential equations solved in PISCES IDL have been summarized in the general description. The first order explicit finite-difference equations that have been used to approximate the differential equations are discussed below.

For the following discussion there are a few definitions and conventions which must be addressed. First, PISCES IDL is a one-dimensional Lagrange code. The space variable is divided into zones of fixed mass. Grid points bound each zone. An interior grid point is bounded by a zone on either side while a boundary grid point has one of the zones replaced by a boundary condition. A left boundary grid point has a zone only on its right; a right boundary grid point has a zone only on its left. Indexing of grid points is generally denoted by j and increases from left to right. Indexing of zones is done by associating a zone with its right side grid point index. Thus, the leftmost boundary grid point (or the lowest index number) has no zone associated with it.

The calculations are divided into two types--grid point and zone. Associated with each interior grid point is a Lagrange position, velocity, acceleration, half of the mass of each of the neighboring zones, and a heat flow area. Associated with each zone is the fixed zone mass, relative volume, density, compression, pressure, artificial viscosity, stress deviators, yield stress, internal energy density, distortional energy density, sound speed, and temperature.

Two basic conservation equations are solved- one for each of the two types of calculations. The Lagrange equation of motion, derived from conservation of momentum and conservation of mass, is used to update grid point variables. The Lagrange thermal energy equation, derived from conservation of energy and continuity, is used to update zone variables.*

Updating of grid point variables is done in subroutine MOTION. First the equation of motion is used to calculate grid point accelerations of the previous cycle from stresses calculated in the previous cycle.

For NSWD = 1 (plane symmetry)

$$\ddot{r}^n = \frac{1}{\rho^n} \frac{\partial \Sigma_r^n}{\partial r} .$$

For NSWD = 2 (cylindrical symmetry)

$$\ddot{r}^n = \frac{1}{\rho^n} \frac{\partial \Sigma_r^n}{\partial r} + \frac{1}{\rho^n} \left[\frac{\Sigma_r^n - \Sigma_t^n}{r} \right] j .$$

*Derivation of basic equations is available upon request.

IDL-A

For NSWD = 3 (spherical symmetry)

$$\ddot{r}^n = \frac{1}{\rho^n} \frac{\partial \Sigma_r^n}{\partial r} + \frac{2}{\rho^n} \left[\frac{\Sigma_r^n - \Sigma_t^n}{r} \right].$$

For NSWD = 4.5 (flume symmetry)*

$$\ddot{r}^n = \frac{1}{\rho^n} \frac{\partial \Sigma_r^n}{\partial r}.$$

A general form of these equations may be written in the following way:

$$\ddot{r}^n = \frac{1}{\rho^n} \frac{\partial \Sigma_r^n}{\partial r} + \frac{1}{\rho^n} (d-1) \left[\frac{\Sigma_r^n - \Sigma_t^n}{r} \right]$$

where $d = \text{NSWD}$ and for $\text{NSWD} > 3$, set $d = 1$. This equation may be rewritten in terms of the relative volume, $v^n = \rho_0 / \rho^n$ where ρ_0 is a reference density usually set equal to the initial density

$$\ddot{r}^n = \frac{v^n}{\rho_0} \frac{\partial \Sigma_r^n}{\partial r} + \frac{v^n}{\rho_0} (d-1) \left[\frac{\Sigma_r^n - \Sigma_t^n}{r} \right].$$

The finite difference analog of the coefficient of $\frac{\partial \Sigma_r^n}{\partial r}$ is the reciprocal of the grid point areal density. The areal density to the left of the grid point j and the areal density to the right of the grid point j are, respectively,

$$m_1^n = \rho_{0_j} (r_j^n - r_{j-1}^n) / V_j^n$$

$$m_2^n = \rho_{0_{j+1}} (r_{j+1}^n - r_j^n) / V_{j+1}^n.$$

*See Appendix A for derivation.

The stress difference in brackets is calculated from an average of the stress difference in the zones to the left and right of the grid point. These are, respectively,

$$\Sigma_{\theta 1}^n = \left[\left(\Sigma_{r_j}^n - \Sigma_{t_j}^n \right) / \left(\frac{r_{j-1}^n + r_j^n}{2} \right) \right] \frac{v_j^n}{\rho_{o_j}}$$

$$\Sigma_{\theta 2}^n = \left[\left(\Sigma_{r_{j+1}}^n - \Sigma_{t_{j+1}}^n \right) / \left(\frac{r_{j+1}^n + r_j^n}{2} \right) \right] \frac{v_{j+1}^n}{\rho_{o_{j+1}}}.$$

Thus, for an interior grid point, i.e., a non-boundary grid point, the finite difference formula for the equation of motion is

$$\ddot{r}_j^n = \left[\frac{2}{m_1^n + m_2^n} \right] \left[\Sigma_{r_{j+1}}^n - \Sigma_{r_j}^n \right] + (d-1) \left[\frac{\Sigma_{\theta 1}^n + \Sigma_{\theta 2}^n}{2} \right]. \quad (1)$$

When calculating a free left boundary, m_1^n is zero and $\Sigma_{\theta 1}^n$ is zero. For a pressure time history applied to the left boundary, m_1^n is still zero but $\Sigma_{\theta 1}^n$ takes on the values of the prescribed pressure. For a fixed boundary, the above equation is superfluous and $\dot{r}_j^{n+\frac{1}{2}}$ is set to zero. Similarly, a velocity condition on the boundary (piston) is automatically set equal to $\dot{r}_j^{n+\frac{1}{2}}$. Right boundaries are handled in a similar way, but m_2^n and $\Sigma_{\theta 2}^n$ are adjusted. Only one difference exists, $\Sigma_{\theta 2}^n$ takes on values of minus the pressure time history when a pressure profile is used.

Void boundaries are calculated as free boundaries. A left void boundary is a right free boundary of the solid region on the left. A right void boundary is a left free boundary of the solid region on the right. Void closure results in the two boundary points becoming one interior point. The velocity of closure is computed to give exact closure while conserving momentum. This will result in an induced energy error. To see this, consider the formulas for closure velocity derived from conservation of momentum

$$\dot{r}_{ave_M} = \frac{m_a \dot{r}_a + m_b \dot{r}_b}{m_a + m_b}$$

and from conservation of energy

$$\dot{r}_{ave_E} = \left[\frac{m_a \dot{r}_a^2 + m_b \dot{r}_b^2}{m_a + m_b} \right]^{\frac{1}{2}}.$$

IDL-A

When $m_a = m_b = m$, the formulas become

$$\dot{r}_{ave_M} = \left[\frac{\dot{r}_a + \dot{r}_b}{2} \right] \quad \text{and} \quad \dot{r}_{ave_E} = \left[\frac{\dot{r}_a^2 + \dot{r}_b^2}{2} \right]^{\frac{1}{2}}.$$

Furthermore, if $\dot{r}_b = 0$, then

$$\dot{r}_{ave_N} = \frac{\dot{r}_a}{2} \quad \text{and} \quad \dot{r}_{ave_E} = \frac{\dot{r}_a}{\sqrt{2}}.$$

The differences are clear.

When Equation (1) is used to get acceleration, \ddot{r}_j^n , subsequent calculations for new velocity, $\dot{r}_j^{n+\frac{1}{2}}$, and new position, r_j^{n+1} , are computed from the following time-centered equations:

$$\dot{r}_j^{n+\frac{1}{2}} = \dot{r}_j^{n-\frac{1}{2}} + \ddot{r}_j^n \Delta t^n \quad (2)$$

$$r_j^{n+1} = r_j^n + \dot{r}_j^{n+\frac{1}{2}} \Delta t^{n+\frac{1}{2}}. \quad (3)$$

In cases where a velocity boundary condition is used, only Equation (3) applies. Then $\dot{r}_j^{n-\frac{1}{2}}$ and r_j^n are the velocity and position from the previous cycle (or initial conditions); Δt^n and $\Delta t^{n+\frac{1}{2}}$ come from stability considerations based on the previous cycle (or an initial value).

Once the positions and velocities of grid points forming a zone have been updated in subroutine MOTION (and/or VOID), pressure, volume, energy, etc., can be calculated for the zone. These and other zone interior variables are computed in subroutine ZONE.

The first zone interior variable calculated in subroutine ZONE is the relative volume. It should be obvious that once new coordinates are available, one can compute a new volume.

For NSWD = 1 (plane symmetry)

$$\text{TRUE VOLUME}_j^{n+1} = r_j^{n+1} - r_{j-1}^{n+1}.$$

For NSWD = 2 (cylindrical symmetry)

$$\text{TRUE VOLUME}_j^{n+1} = \pi \left[(r_j^{n+1})^2 - (r_{j-1}^{n+1})^2 \right].$$

For NSWD = 3 (spherical symmetry)

$$\text{TRUE VOLUME}_j^{n+1} = \frac{4}{3}\pi \left[(r_j^{n+1})^3 - (r_{j-1}^{n+1})^3 \right].$$

For NSWD = 4 (fixed wall flume)*

$$\text{TRUE VOLUME}_j^{n+1} = \sum_{r_{j-1}^{n+1}}^{r_j^{n+1}} (\text{frustums defined by } R_i)$$

where R_i are wall points between r_{j-1}^{n+1} and r_j^{n+1} .

For NSWD = 5 (Moving wall flume)*

$$\text{TRUE VOLUME}_j^{n+1} = \sum_{r_{j-1}^{n+1}}^{r_j^{n+2}} (\text{frustums defined by } R_i^{n+1})$$

where R_i^{n+1} are wall points between r_{j-1}^{n+1} and r_j^{n+2} .

To compute relative volume, V , form the expression

$$V_j^{n+1} = \frac{(\text{TRUE VOLUME}_j^{n+1})(\text{REFERENCE DENSITY}_j)}{\text{MASS}_j}$$

*See Appendix A for a picture of a typical flume section.

IDL-A

and from this, the change in relative volume (needed to compute change of energy) would be

$$\Delta V_j^{n+\frac{1}{2}} = (\text{TRUE VOLUME}_j^{n+1} - \text{TRUE VOLUME}_j^n) \frac{\rho_{o,i}}{m_j}.$$

Expanding, the change of relative volume equation yields (e.g., plane symmetry)

$$\Delta V_j^{n+\frac{1}{2}} = \left[(r_j^{n+1} - r_{j-1}^{n+1}) - (r_j^n - r_{j-1}^n) \right] \frac{\rho_{o,i}}{m_j}.$$

Rearranging,

$$\Delta V_j^{n+\frac{1}{2}} = \left[(r_j^{n+1} - r_j^n) + (r_{j-1}^{n+1} - r_{j-1}^n) \right] \frac{\rho_{o,i}}{m_j}.$$

This form of the equation reveals possible numerical difficulties when the change in a coordinate is smaller than the number of significant digits available in a specific computer. If change of relative volume were calculated this way, it is possible to change the distance between zones a small amount without getting a correspondingly small change in relative volume. For this reason PISCES IDL does not calculate change of relative volume from coordinates as shown above. Instead, change of relative volume is computed directly from velocities in the following way.

For plane symmetry

$$v_j^{n+1} = \frac{\rho_{o,i}}{m_j} \left[r_j^{n+1} - r_{j-1}^{n+1} \right]$$

$$\frac{d(v_j^{n+1})}{dt} = \frac{\rho_{o,i}}{m_j} \frac{d}{dt} \left[r_j^{n+1} - r_{j-1}^{n+1} \right]$$

$$\Delta V_j^{n+\frac{1}{2}} = \frac{\rho_{o,i}}{m_j} \left[\dot{r}_j^{n+\frac{1}{2}} - \dot{r}_{j-1}^{n+\frac{1}{2}} \right]$$

$$\Delta V_j^{n+\frac{1}{2}} = \frac{\rho_{o,i}}{m_j} \left[\dot{r}_j^{n+\frac{1}{2}} - \dot{r}_{j-1}^{n+\frac{1}{2}} \right] \Delta t^{n+\frac{1}{2}}.$$

Computing new relative volume, $v^{n+\frac{1}{2}}$, from the change of relative volume, $\Delta v^{n+\frac{1}{2}}$, could also introduce round-off error if $v^{n+\frac{1}{2}} \ll v^n$. In general, $v^{n+\frac{1}{2}}$ is near 1.0 and $\Delta v^{n+\frac{1}{2}}$ is very small. To eliminate the possibility of this kind of round-off, a transformation of variables is made. The variable compression, C , is defined as follows:^{*}

$$C = 1. - v$$

$$\Delta C = \Delta(1. - v) = -\Delta v. \quad (4)$$

Compression and change in compression are generally both numbers of the same order of magnitude. The equation

$$c_j^{n+1} = c_j^n + \Delta c_j^{n+\frac{1}{2}}$$

therefore, does not introduce a round-off error. New relative volume comes directly from c_j^{n+1}

$$v_j^{n+1} = 1. - c_j^{n+1}.$$

The formula for change in compression in plane symmetry is

$$\Delta c_j^{n+\frac{1}{2}} = -\frac{\rho_{o,j}}{m_j} \Delta t^{n+\frac{1}{2}} \left[\dot{r}_j^{n+\frac{1}{2}} - \dot{r}_{j-1}^{n+\frac{1}{2}} \right]. \quad (4.1)$$

What we have here is a formula for the change of relative volume that depends on velocities, not position. If the velocities yield no change in relative volume, then one is guaranteed that the distance between zones actually is unchanged since new positions are computed from new velocities.

To use this formula, one must be sure that it agrees with the development based on coordinates. This must be a requirement since the TRUE VOLUME formulas are exact for large displacements. Again, looking at the plane symmetry case, we see

$$\Delta v_j^{n+\frac{1}{2}} = \frac{\rho_{o,j}}{m_j} \left[\left(\frac{\dot{r}_j^{n+1} - \dot{r}_j^n}{\Delta t^{n+\frac{1}{2}}} \right) - \left(\frac{\dot{r}_{j-1}^{n+1} - \dot{r}_{j-1}^n}{\Delta t^{n+\frac{1}{2}}} \right) \right] \Delta t^{n+\frac{1}{2}}$$

which reduces to the result obtained previously,

$$\Delta v_j^{n+\frac{1}{2}} = \frac{\rho_{o,j}}{m_j} \left[\left(r_j^{n+1} - r_j^n \right) - \left(r_{j-1}^{n+1} - r_{j-1}^n \right) \right].$$

^{*}See Appendix B for relations between volume, relative volume, dilation and compression.

IDL-A

For cylindrical symmetry, change of relative volume from coordinates is

$$\Delta V_j^{n+\frac{1}{2}} = \frac{\rho_0}{m_j} \pi \left| \left[\left(r_j^{n+1} \right)^2 - \left(r_{j-1}^{n+1} \right)^2 \right] - \left[\left(r_j^n \right)^2 - \left(r_{j-1}^n \right)^2 \right] \right|$$

$$\Delta V_j^{n+\frac{1}{2}} = \frac{\rho_0}{m_j} \pi \left| \left[\left(r_j^{n+1} \right)^2 - \left(r_j^n \right)^2 \right] - \left[\left(r_{j-1}^{n+1} \right)^2 - \left(r_{j-1}^n \right)^2 \right] \right|.$$

From velocities

$$\frac{d(V_j^{n+1})}{dt} = \frac{\rho_0}{m_j} \frac{d}{dt} \left\{ \pi \left[\left(r_j^{n+1} \right)^2 - \left(r_{j-1}^{n+1} \right)^2 \right] \right\}$$

$$\Delta V_j^{n+\frac{1}{2}} = \frac{\rho_0}{m_j} 2\pi \left[\dot{r}_j^{n+\frac{1}{2}} r_j^{n+\frac{1}{2}} - \dot{r}_{j-1}^{n+\frac{1}{2}} r_{j-1}^{n+\frac{1}{2}} \right] \Delta t^{n+\frac{1}{2}}$$

$$\Delta C_j^{n+\frac{1}{2}} = -2\pi \frac{\rho_0}{m_j} \Delta t^{n+\frac{1}{2}} \left[\dot{r}_j^{n+\frac{1}{2}} r_j^{n+\frac{1}{2}} - \dot{r}_{j-1}^{n+\frac{1}{2}} r_{j-1}^{n+\frac{1}{2}} \right]. \quad (4.2)$$

Expanding, we achieve agreement with the formula from coordinates:

$$\Delta V_j^{n+\frac{1}{2}} = \frac{\rho_0}{m_j} 2\pi \left[\left(\frac{r_j^{n+1} - r_j^n}{\Delta t^{n+\frac{1}{2}}} \right) r_j^{n+\frac{1}{2}} - \left(\frac{r_{j-1}^{n+1} - r_{j-1}^n}{\Delta t^{n+\frac{1}{2}}} \right) r_{j-1}^{n+\frac{1}{2}} \right] \Delta t^{n+\frac{1}{2}}$$

$$\Delta V_j^{n+\frac{1}{2}} = \frac{\rho_0}{m_j} 2\pi \left[\left(r_j^{n+1} - r_j^n \right) \left(\frac{r_j^{n+1} + r_j^n}{2} \right) - \left(r_{j-1}^{n+1} - r_{j-1}^n \right) \left(\frac{r_{j-1}^{n+1} + r_{j-1}^n}{2} \right) \right]$$

$$\Delta V_j^{n+\frac{1}{2}} = \frac{\rho_0}{m_j} \pi \left| \left[\left(r_j^{n+1} \right)^2 - \left(r_j^n \right)^2 \right] - \left[\left(r_{j-1}^{n+1} \right)^2 - \left(r_{j-1}^n \right)^2 \right] \right|.$$

Finally, in spherical geometry the change of relative volume from coordinates is

$$\Delta V_j^{n+\frac{1}{2}} = \frac{\rho_0}{m_j} \frac{4}{3} \pi \left\{ \left[\left(r_j^{n+1} \right)^3 - \left(r_{j-1}^{n+1} \right)^3 \right] - \left[\left(r_j^n \right)^3 - \left(r_{j-1}^n \right)^3 \right] \right\}$$

$$\Delta V_j^{n+\frac{1}{2}} = \frac{\rho_0}{m_j} \frac{4}{3} \pi \left\{ \left[\left(r_j^{n+1} \right)^3 - \left(r_j^n \right)^3 \right] - \left[\left(r_{j-1}^{n+1} \right)^3 - \left(r_{j-1}^n \right)^3 \right] \right\}.$$

From velocities

$$\frac{d(v_j^{n+1})}{dt} = \frac{\rho_0}{m_j} \frac{d}{dt} \left\{ \frac{4}{3} \pi \left[\left(r_j^{n+1} \right)^3 - \left(r_{j-1}^{n+1} \right)^3 \right] \right\}$$

$$\Delta V_j^{n+\frac{1}{2}} = \frac{\rho_0}{m_j} 4 \pi \left[\dot{r}_j^{n+\frac{1}{2}} \left(r_j^{n+\frac{1}{2}} \right)^2 - \dot{r}_{j-1}^{n+\frac{1}{2}} \left(r_{j-1}^{n+\frac{1}{2}} \right)^2 \right] \Delta t^{n+\frac{1}{2}}.$$

If this formula is expanded, it will not agree with the formula derived directly from coordinates. There is an error reflecting the lack of second-order accuracy in taking the derivative. The formula in terms of velocities becomes

$$\Delta V_j^{n+\frac{1}{2}} = \frac{\rho_0}{m_j} 4 \pi \left[\dot{r}_j^{n+\frac{1}{2}} \left(r_j^{n+\frac{1}{2}} \right)^2 - \dot{r}_{j-1}^{n+\frac{1}{2}} \left(r_{j-1}^{n+\frac{1}{2}} \right)^2 + x_j^{n+\frac{1}{2}} \right] \Delta t^{n+\frac{1}{2}}$$

where

$$x_j^{n+\frac{1}{2}} = \frac{(\Delta t^{n+\frac{1}{2}})^2}{12} \left[\left(\dot{r}_j^{n+\frac{1}{2}} \right)^3 - \left(\dot{r}_{j-1}^{n+\frac{1}{2}} \right)^3 \right]$$

when the error is accounted for. The change in compression is

$$\Delta c_j^{n+\frac{1}{2}} = -\frac{4}{3} \pi \frac{\rho_0}{m_j} \Delta t^{n+\frac{1}{2}} 3 \left[\dot{r}_j^{n+\frac{1}{2}} \left(r_j^{n+\frac{1}{2}} \right)^2 - \dot{r}_{j-1}^{n+\frac{1}{2}} \left(r_{j-1}^{n+\frac{1}{2}} \right)^2 + x_j^{n+\frac{1}{2}} \right] \quad (4.3)$$

IDL-A

where again

$$x_j^{n+\frac{1}{2}} = \frac{(\Delta t^{n+\frac{1}{2}})^2}{12} \left[\left(\dot{r}_j^{n+\frac{1}{2}} \right)^3 - \left(\dot{r}_{j-1}^{n+\frac{1}{2}} \right)^3 \right].$$

New relative volume is now computed from new compression.

$$c_j^{n+1} = c_j^n + \Delta c_j^{n+\frac{1}{2}} \quad (5)$$

$$v_j^{n+1} = 1. - c_j^{n+1}. \quad (6)$$

Change in relative volume is of course the negative of the change in compression.

$$\Delta v_j^{n+\frac{1}{2}} = - \Delta c_j^{n+\frac{1}{2}}. \quad (7)$$

The rate of change of relative volume can be computed directly.

$$\frac{\dot{v}_j^{n+\frac{1}{2}}}{v_j^{n+\frac{1}{2}}} = \frac{\Delta v_j^{n+\frac{1}{2}} / \Delta t^{n+\frac{1}{2}}}{v_j^{n+\frac{1}{2}}}. \quad (8)$$

Once the new relative volume has been determined, the artificial viscosity, pressure, energy, stress deviators and new time step may be determined.

Artificial viscosity, $q_j^{n+\frac{1}{2}}$, is computed in the following way (Appendix C):

$$q_j^{n+\frac{1}{2}} = q_{Q,j}^{n+\frac{1}{2}} + q_{L,j}^{n+\frac{1}{2}}. \quad (9)$$

The artificial viscosity is the sum of an artificial quadratic viscosity, $q_{Q,j}^{n+\frac{1}{2}}$, and an artificial linear viscosity, $q_{L,j}^{n+\frac{1}{2}}$.

$$q_{Q,j}^{n+\frac{1}{2}} = - \frac{\rho_0}{v_j^{n+\frac{1}{2}}} c_j^2 \left(\Delta r_j^{n+\frac{1}{2}} \right)^2 \frac{\dot{v}_j^{n+\frac{1}{2}}}{v_j^{n+\frac{1}{2}}} \left| \frac{\dot{v}_j^{n+\frac{1}{2}}}{v_j^{n+\frac{1}{2}}} \right| \quad (9.1)$$

where ρ_0 = reference density, $v_j^{n+\frac{1}{2}}$ = relative volume, Δx is distance across the zone, and c_Q = coefficient of quadratic viscosity.

$$q_L^{n+\frac{1}{2}} = - \frac{\rho_0}{v_j^{n+\frac{1}{2}}} c_{Lj} \Delta x_j^{n+\frac{1}{2}} c_j^n \left| \frac{\dot{v}_j^{n+\frac{1}{2}}}{v_j^{n+\frac{1}{2}}} \right| \quad (9.2)$$

where c_L = coefficient of linear viscosity and c = sound speed.

The computation of pressure and energy cannot be done in a straightforward manner because one depends on the other. Therefore, an iterative approach* is required. First, a preliminary calculation is made, estimating the new energy from new change in relative volume, new artificial viscosity, and old pressure. Distortional energy change is ignored since new stress deviators have not yet been calculated. This first estimate of the new energy is called \tilde{E}_j^{n+1} .

$$\tilde{E}_j^{n+1} = E_j^n - \left[\frac{1}{2} (p_j^n + p_j^n) + q_j^{n+\frac{1}{2}} \right] \Delta V_j^{n+\frac{1}{2}}. \quad (10)$$

If energy is deposited from outside the grid, it is added into E_j^n prior to the first approximation to the energy, e.g.,

$$E_j^n = E_j^n + \frac{1}{\tau} E'_j \Delta t^{n+\frac{1}{2}}$$

where E'_j is the total energy to be deposited in a zone.

Now using the energy estimate, \tilde{E}_j^{n+1} , subroutine STATE is called to get an estimate of pressure, \tilde{p}_j^{n+1} .

$$\tilde{p}_j^{n+1} = f(\tilde{E}_j^{n+1}, v_j^{n+1}). \quad (11)$$

Returning to subroutine ZONE, stress deviators are computed by first calculating the "elastic" deviators at plus time from strain rates at half time. The elastic one-dimensional deviators are computed from

$$s_r_j^{n+1} = s_r_j^n + 2G \left(\dot{\epsilon}_r_j^{n+\frac{1}{2}} \Delta t^{n+\frac{1}{2}} - \frac{1}{3} \frac{\dot{v}_j^{n+\frac{1}{2}}}{v_j^{n+\frac{1}{2}}} \right) \quad (12)$$

*Appendix D.

IDL-A

where $2G$ equals two times the shear modulus, G . $\Delta v_j^{n+\frac{1}{2}}$, $v_j^{n+\frac{1}{2}}$, and $\Delta t^{n+\frac{1}{2}}$ have been previously defined, and

$$\dot{\epsilon}_{r_j}^{n+\frac{1}{2}} = \left(\dot{v}_j^{n+\frac{1}{2}} - \dot{v}_{j-1}^{n+\frac{1}{2}} \right) / \Delta r^{n+\frac{1}{2}}. \quad (13)$$

In PISCES 1DL only the radial deviator is independent. The tangential deviator and the deviator normal to the radial and tangential deviators are calculated from symmetry considerations.*

For NSWD = 1 (plane symmetry)**

$$\dot{\epsilon}_{t_j}^{n+\frac{1}{2}} = \dot{\epsilon}_{N_j}^{n+\frac{1}{2}} = 0$$

$$s_{t_j}^{n+1} = s_{N_j}^{n+1} = -\frac{1}{2} s_{r_j}^{n+1}.$$

For NSWD = 2 (cylindrical symmetry)**

$$\dot{\epsilon}_{t_j}^{n+\frac{1}{2}} = \frac{\dot{v}_j^{n+\frac{1}{2}}}{v_j^{n+\frac{1}{2}}} - \dot{\epsilon}_{r_j}^{n+\frac{1}{2}}, \quad \dot{\epsilon}_{N_j}^{n+\frac{1}{2}} = 0$$

$$s_{t_j}^{n+1} = s_{r_j}^n + 2G \left(\dot{\epsilon}_{t_j}^{n+\frac{1}{2}} \Delta t^{n+\frac{1}{2}} - \frac{1}{3} \frac{\Delta v_j^{n+\frac{1}{2}}}{v_j^{n+\frac{1}{2}}} \right), \quad s_{N_j}^{n+1} = - \left(s_{r_j}^{n+1} + s_{t_j}^{n+1} \right).$$

For NSWD = 3 (spherical symmetry)**

$$\dot{\epsilon}_{t_j}^{n+\frac{1}{2}} = \dot{\epsilon}_{N_j}^{n+\frac{1}{2}} = \frac{1}{2} \left(\frac{\dot{v}_j^{n+\frac{1}{2}}}{v_j^{n+\frac{1}{2}}} - \dot{\epsilon}_{r_j}^{n+\frac{1}{2}} \right)$$

$$s_{t_j}^{n+1} = s_{N_j}^{n+1} = -\frac{1}{2} s_{r_j}^{n+1}.$$

These elastic deviators may now be reduced in subroutine YIELD so that they do not exceed a von Mises yield surface. The elastic yield stress squared is defined by

*In PISCES 2DL there are three independent deviators

**See Appendix E for relations between ϵ_r , ϵ_t and C

$$\left(\sigma_{o_j}^{n+1}\right)^2 = \frac{3}{2} \left[\left(s_{r_j}^{n+1}\right)^2 + \left(s_{t_j}^{n+1}\right)^2 + \left(s_{N_j}^{n+1}\right)^2 \right]. \quad (14)$$

This quantity is compared with the computed allowable yield stress squared. $(Y_j^{n+1})^2$.

$$Y_j^{n+1} = f_o(p_j^{n+1}, E_j^{n+1}, v_j^{n+1}, z_j^n, t^{n+1}). \quad (15)$$

(Notice that p_j^{n+1} and E_j^{n+1} are really \tilde{p}_j^{n+1} and \tilde{E}_j^{n+1} .)

The comparison is made in the following way:

$$\Delta Y_j^{n+1} = \frac{2}{3} \left[\left(\sigma_{o_j}^{n+1}\right)^2 - \left(Y_j^{n+1}\right)^2 \right].$$

If ΔY_j^{n+1} is negative, the deviators are correct already; everything is elastic. If ΔY_j^{n+1} is positive, the deviators are adjusted by the ratio of allowable to elastic yield stress

$$\begin{aligned} Y_{*j}^{n+1} &= Y_j^{n+1}/\sigma_{o_j}^{n+1} \\ s_{r_j}^{n+1} &= Y_{*j}^{n+1} s_{r_j}^{n+1}, \quad s_{t_j}^{n+1} = Y_{*j}^{n+1} s_{t_j}^{n+1}. \end{aligned} \quad (16)$$

(If $Y_j^{n+1} = 0$, then $s_{r_j}^{n+1} = s_{t_j}^{n+1} = s_{N_j}^{n+1} = 0$. exactly. This is the condition for hydrodynamic flow.)

From the new stress deviators one can calculate the change in distortional energy.

$$\Delta Z_j^{n+\frac{1}{2}} = v_j^{n+\frac{1}{2}} \Delta t^{n+\frac{1}{2}} \left[s_{r_j}^{n+\frac{1}{2}} \dot{\varepsilon}_{r_j}^{n+\frac{1}{2}} + (d-1) s_{t_j}^{n+\frac{1}{2}} \dot{\varepsilon}_{t_j}^{n+\frac{1}{2}} \right] \quad (17)$$

where

$$s_{r_j}^{n+\frac{1}{2}} = \frac{1}{2} (s_{r_j}^n + s_{r_j}^{n+1}), \quad s_{t_j}^{n+\frac{1}{2}} = \frac{1}{2} (s_{t_j}^n + s_{t_j}^{n+1}).$$

IDL-A

Now the energy is recalculated.

$$E_j^{n+1} = E_j^n + \Delta Z_j^{n+\frac{1}{2}} - \Delta V_j^{n+\frac{1}{2}} \left[\left(p_j^n + \tilde{p}_j^{n+1} \right) \frac{1}{2} + q_j^{n+\frac{1}{2}} \right] + H_j \quad (18)$$

where H_j is the energy transfer due to conduction (Reference 3). This value of energy is used to compute the final value of pressure.

$$p_j^{n+1} = f(E_j^{n+1}, V_j^{n+1}). \quad (19)$$

Stresses are calculated from pressure and the deviator tensor

$$\Sigma_r_j^{n+1} = s_r_j^{n+1} - \left(p_j^{n+1} + q_j^{n+\frac{1}{2}} \right) \quad (20)$$

$$\Sigma_t_j^{n+1} = s_t_j^{n+1} - \left(p_j^{n+1} + q_j^{n+\frac{1}{2}} \right).$$

The sound speed squared is calculated in subroutine SSPD *

$$(c_j^{n+1})^2 = f_1(p_j^{n+1}, V_j^{n+1}) \quad (21)$$

and upon the return to ZONE, a time step squared based on the just calculated sound speed and the zone width is computed.

$$\left(\Delta t_j^{n+\frac{1}{2}} \right)^2 = \frac{\left(\Delta r_j^{n+\frac{1}{2}} \right)^2}{\left(c_j^{n+1} \right)^2 \left(1 + 4c_L^2 \right) + \left(2c_Q \right)^2 \left(\Delta r_j^{n+\frac{1}{2}} \right)^2 \left(\frac{V_j^{n+\frac{1}{2}}}{V_j^{n+\frac{1}{2}}} \right)^2}. \quad (22)$$

The smallest $\left(\Delta t_j^{n+\frac{1}{2}} \right)^2$ is saved to be used to get the time step for the next cycle.

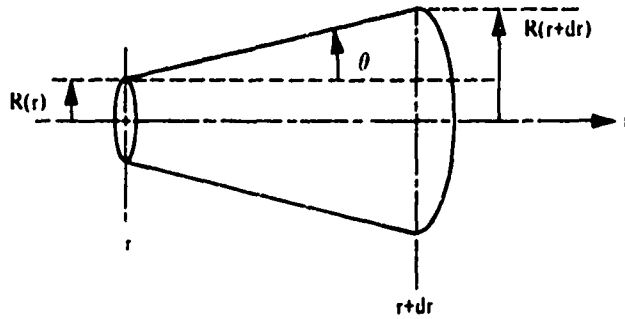
$$\Delta t^{n+3/2} = f_2 \left(\sqrt{\min_j \left(\Delta t_j^{n+\frac{1}{2}} \right)^2} \right).$$

*See Appendix F for definition of adiabatic sound speed in terms of different density parameters for elastic-plastic materials.

REFERENCES

1. "Calculation of Elastic-Plastic Flow," Mark L. Wilkins, UCRL-7322, Rev. 1, January 24, 1969, Lawrence Radiation Laboratory, Livermore, California.
2. "A Method for the Numerical Calculation of Hydrodynamic Shocks," J. Von Neumann and R. D. Richtmyer, *J. Appl. Phys.*, 21, March 1950, pp. 232-237.
3. "Heat Conduction in the PISCES IDL Code," S. Jardin, TCAM 72-3, 1972.

APPENDIX A
DERIVATION OF EQUATION OF MOTION IN FLUME SYMMETRY



The external force on the left face of the frustum is

$$F_L = -\Sigma(r) \pi [R(r)]^2$$

Similarly, the external force on the right face is

$$F_R = \Sigma(r+dr) \pi [R(r+dr)]^2$$

The axial component of the force of constraint due to the rigid wall may be given by

$$\begin{aligned}
 F_W &= -\Sigma(r^*) \times [\text{area of frustum}] \times \sin \theta \text{ where } r \leq r^* \leq r+dr \\
 &= \Sigma(r^*) \times \pi [R(r) + R(r+dr)] \sqrt{(dr)^2 + [R(r+dr) - R(r)]^2} \\
 &\times \frac{R(r+dr) - R(r)}{\sqrt{(dr)^2 + [R(r+dr) - R(r)]^2}} \\
 &= \Sigma(r^*) \pi [R(r) + R(r+dr)][R(r+dr) - R(r)]
 \end{aligned}$$

1DL-A

Newton's second law takes the form

$$\rho \pi [R(r^*)]^2 dr \ddot{r} = -\Sigma(r) \pi [R(r)]^2 + \Sigma(r+dr) \pi [R(r+dr)]^2$$
$$-\Sigma(r^*) \pi [R(r) + R(r+dr)][R(r+dr) - R(r)]$$

Letting

$$R(r+dr) = R(r) + dr \frac{\partial R}{\partial r}, \text{ etc. gives}$$

$$\rho R^2 dr \ddot{r} = dr \frac{\partial \Sigma}{\partial r} R^2 - 2dr \Sigma R \frac{\partial R}{\partial r} + 2dr \Sigma R \frac{\partial R}{\partial r}$$

$$\ddot{r} = \frac{1}{\rho} \frac{\partial \Sigma}{\partial r}$$

APPENDIX B

RELATIONS BETWEEN MEASURES OF VOLUME CHANGE

Notation:

$$V_o = \text{initial volume}$$

$$V = \text{actual volume}$$

$$V_r = \text{relative volume} = \frac{V}{V_o}$$

$$\Delta = \text{cubical dilation} = \frac{V}{V_o} - 1 = \frac{V - V_o}{V_o}$$

$$C = \text{compression} = 1 - V_r = 1 - \frac{V}{V_o} = \frac{V_o - V}{V_o}$$

$$\mu \equiv \frac{C}{1-C} = \frac{1-V_r}{V_r} = \frac{V_o - V}{V}$$

$$\rho \equiv \rho_o \frac{V_o}{V} = \frac{\rho_o}{V_r}$$

	Δ	μ	C	V_r
Δ	Δ	$\frac{-\Delta}{1+\Delta}$	$-\Delta$	$1+\Delta$
μ	$\frac{-\mu}{1+\mu}$	μ	$\frac{\mu}{1+\mu}$	$\frac{1}{1+\mu}$
C	$-C$	$\frac{C}{1-C}$	C	$1-C$
ρ	$\frac{\rho_o - \rho}{\rho}$	$\frac{\rho - \rho_o}{\rho_o}$	$\frac{\rho - \rho_o}{\rho}$	$\frac{\rho_o}{\rho}$
V_r	$V_r - 1$	$\frac{1 - V_r}{V_r}$	$1 - V_r$	V_r
V, V_o	$\frac{V - V_o}{V_o}$	$\frac{V_o - V}{V}$	$\frac{V_o - V}{V_o}$	$\frac{V}{V_o}$

APPENDIX C

THE q STABILITY CRITERION

The derivation of the q stability criterion may be found in the references listed at the end of this appendix. When reading these references, it will help to know the corresponding notation. PISCES IDL C_Q is c in Von Neumann and Richtmyer's article and a in Richtmyer's book. The ℓ in Richtmyer's book is C_Q times the zone size ahead of the shock. Richtmyer's V is specific volume, and his E is internal energy per unit mass. Richtmyer's R is the same as PISCES IDL r , but for the distance across a zone he often uses the more complicated expression,

$$\Delta R = \frac{\rho_0}{\rho} \Delta r \left(\frac{r}{R} \right)^{\alpha-1}$$

where r is the original coordinate and α is 1, 2, or 3 for plane, cylindrical, or spherical symmetry, respectively.

A simplified derivation of the quadratic q_Q stability criterion will be given here. The same method may be used to derive the linear q_L criterion. The differential equations in plane symmetry are

$$\rho \frac{\partial U}{\partial t} = - \frac{\partial(p + q_Q)}{\partial x}$$

$$\frac{1}{V} \frac{\partial V}{\partial t} = \frac{\partial U}{\partial x}$$

$$q_Q = - C_Q^2 \rho (\Delta x)^2 | \frac{1}{V} \frac{\partial V}{\partial t} | \frac{1}{V} \frac{\partial V}{\partial t} .$$

where U is velocity and Δx is the zone size. We want to examine the case where pressure is negligible compared to q_Q . Set p equal to zero in the first equation. Eliminate relative volume from the last two equations.

$$\rho \frac{\partial U}{\partial t} = - \frac{\partial q_Q}{\partial x}$$

$$q_Q = - C_Q^2 \rho (\Delta x)^2 | \frac{\partial U}{\partial x} | \frac{\partial U}{\partial x} .$$

These equations may be combined into one:

$$\rho \frac{\partial U}{\partial t} = C_Q^2 (\Delta x)^2 \frac{\partial}{\partial x} \left[\rho | \frac{\partial U}{\partial x} | \frac{\partial U}{\partial x} \right].$$

In order to make this equation look like the diffusion equation, we want to take the density out from inside the derivative on the right. Say that the variation of density is small compared to the other derivatives (Von Neumann and Richtmyer make the same gross assumption),

$$\begin{aligned} \rho \frac{\partial u}{\partial t} &= C_Q^2 (\Delta x)^2 \rho \frac{\partial}{\partial x} \left[\left| \frac{\partial u}{\partial x} \right| \frac{\partial u}{\partial x} \right] \\ &= C_Q^2 (\Delta x)^2 \rho 2 \left| \frac{\partial u}{\partial x} \right| \frac{\partial^2 u}{\partial x^2}. \end{aligned}$$

Rearranging,

$$\frac{\partial u}{\partial t} = 2C_Q^2 (\Delta x)^2 \left| \frac{\partial u}{\partial x} \right| \frac{\partial^2 u}{\partial x^2}.$$

Again following Von Neumann and Richtmyer, say that the first derivative of velocity varies slowly compared to the second derivative. Then the last equation is the diffusion equation

$$\frac{\partial u}{\partial t} = \sigma \frac{\partial^2 u}{\partial x^2}$$

with the diffusion coefficient

$$\begin{aligned} \sigma &= 2C_Q^2 (\Delta x)^2 \left| \frac{\partial u}{\partial x} \right| \\ &= 2C_Q^2 (\Delta x)^2 |\dot{v}|. \end{aligned}$$

In Chapters 1 and 8 of Richtmyer's book, you will find that all explicit finite difference approximations for the diffusion equation must satisfy the stability criterion

$$\Delta t < \frac{(\Delta x)^2}{2\sigma}.$$

Applied to the present case, the diffusion stability criterion is

$$\Delta t < \frac{1}{4C_Q^2 |\dot{v}|}.$$

This result may be found in Von Neumann and Richtmyer's article at Equation 65 with the diffusion coefficient defined at Equation 45. In the first edition of Richtmyer's book, this result is Equation 10.32 and in the second edition it is Equation 12.48.

Von Neumann and Richtmyer did not stop their derivation with this result, which applies in general, but went on to relate this criterion to the sound speed behind the shock front for the case of a steady uniform shock in a gamma-law gas. Their final result depends on the shock strength, on the equation of state, and on the assumption that the state is uniform behind the shock. The lesson to be learned here is that even the greatest mathematicians sometimes do not know when to stop an analytic derivation of a relation to be used in a general purpose finite difference code. The simplest, most general relation should be used. If one works toward a more specific analytic result to put into a code, the code will be more complicated, less flexible, and less general.

REFERENCES

1. J. Von Neumann and R. D. Richtmyer, *J. Appl. Phys.*, **21**, pp. 232-237 (1950).
2. R. D. Richtmyer, *Difference Methods for Initial-Value Problems*, Interscience Publishers, Inc., New York (1957), First Edition, pp. 218-222 or Second Edition, pp. 320-324.
3. G. E. Forsythe and W. R. Wasow, *Finite-Difference Methods for Partial Differential Equations*, John Wiley & Sons, Inc., New York (1960), pp. 78-82.

APPENDIX D

ACCURACY OF THE PRESSURE-ENERGY ITERATION

Consider two simultaneous equations in two unknowns

$$y = f(x)$$

$$x = g(y).$$

A procedure is to be devised to solve the equations when the functional form of f or g is not known a priori. An iteration may be defined by

$$x_1 = g[f(x_0)]$$

$$x_2 = g[f(x_1)]$$

$$x_{i+1} = g[f(x_i)]$$

where x_0 is a first guess and x_i is the i^{th} approximation. The iteration converges if the derivative of the combined function gf is less than one in absolute value.

$$\left| \frac{d(gf)}{dx} \right| = |g'f'| < 1.0$$

(See Courant, Differential and Integral Calculus, Vol. 1, p. 358.) If the derivative is greater than 1, an iteration using the inverse of the two functions will converge.

If Δx_i is the error of the i^{th} approximation, the error of the next approximation is

$$\Delta x_{i+1} = g'f' \Delta x_i.$$

In PISCES 1DL and 2DL the updated pressure and internal energy density are related by a pair of simultaneous equations.

$$E^{n+1} = f(p^{n+1}) = -\frac{1}{2}(P^{n+1} + p^n) \Delta V^{n+\frac{1}{2}} + E^n$$

$$P^{n+1} = g(V^{n+1}, E^{n+1})$$

where the superscript is the cycle number and g is the equation of state. Following the notation above,

$$f' = -\frac{1}{2} \Delta V$$

$$g' = \Gamma/V$$

1DLA

where $\Gamma = v \left(\frac{\partial P}{\partial E} \right)_V$ is the Gruneisen ratio. Then the convergence factor for the iteration is

$$g' f' = - \frac{\Gamma}{2} \frac{\Delta V}{V}.$$

The Gruneisen ratio is usually near 2 or smaller. Therefore, the error after one iteration is about $-\Delta V/V$ times the error of the first guess and the error after two iterations is about $(\Delta V/V)^2$ times the error of the first guess.

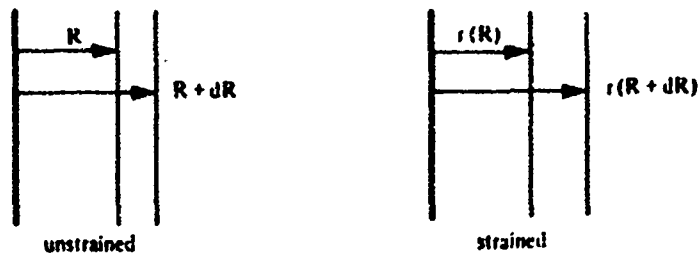
APPENDIX E

RELATION BETWEEN ϵ_r , ϵ_t AND COMPRESSION
IN PLANE, CYLINDRICAL AND SPHERICAL GEOMETRY

Notation:

- R = undeformed coordinate of material point
 $r(R)$ = coordinate of material point in strained state
 $u(R)$ = $r(R) - R$ = displacement of material point
 ϵ_r = du/dr = radial strain
 C = compression
 ϵ_t = tangential strain

Plane Symmetry



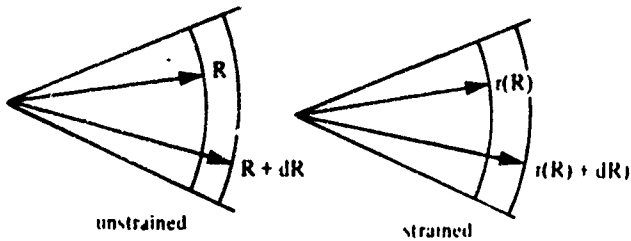
$$\begin{aligned}
 \Delta V &= [\text{final volume}] - [\text{initial volume}] \\
 &= [r(R+dR) - r(R)] - [(R+dR) - R] \\
 &= r(R) + r'(R)dR - r(R) - dR \\
 &= [r'(R) - 1]dR \\
 &= u'(R)dR
 \end{aligned}$$

$$C = -\frac{\Delta V}{V} = -\frac{u'(R)dR}{dR} = -u'(R) = -\epsilon_r \quad (1)$$

$$\epsilon_t = 0.$$

III-A

Cylindrical Symmetry



$$\begin{aligned}
 \Delta V &= [r^2(R+dR) - r^2(R)] - [(R+dR)^2 - R^2] \\
 &= [r^2(R) + 2rr'(R)dR - r^2(R)] - [R^2 + 2RdR - R^2] \\
 &= [2(u(R) + R)(u'(R) + 1) - 2R]dR \\
 &= [2u(R)u'(R) + 2u(R) + 2Ru'(R) + 2R - 2R]dR
 \end{aligned}$$

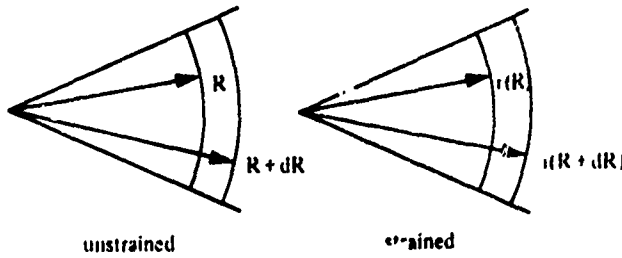
$$C = -\frac{\Delta V}{V} = \frac{2uu' + 2u + 2Ru'}{2R}$$

$$= -\left[c_r + u \frac{\epsilon_r + 1}{R} \right] \quad (2a)$$

$$\epsilon_t = u \frac{\epsilon_r + 1}{R} \quad (2b)$$

$$C = -\epsilon_r - \epsilon_t \quad (2c)$$

Spherical Symmetry



$$\begin{aligned}
 \Delta V &= [\text{final volume}] - [\text{initial volume}] \\
 &= [r^3(R+dR) - r^3(R)] - [(R+dR)^3 - R^3] \\
 r^3(R+dR) &= [r(R) + r'(R)dR]^3 = r^3(R) + 3r^2(R)r'(R)dR \\
 (R+dR)^3 &= R^3 + 3R^2dR \\
 \Delta V &= [r^3(R) + 3r^2(R)r'(R)dR - r^3(R)] - [R^3 + 3R^2dR - R^3] \\
 &= 3r^2(R)r'(R)dR - 3R^2dR \\
 &= 3[u(R) + R]^2[u'(R) + 1]dR - 3R^2dR \\
 &= [3u^2(R)u'(R) + 6u(R)Ru'(R) + 3R^2u'(R) + 3u^2(R) + 6u(R)R + 3R^2 - 3R^2]dR
 \end{aligned}$$

$$C = -\frac{\Delta V}{V} = -\frac{[3u^2u' + 6uRu' + 3R^2u' + 3u^2 + 6uR]dR}{3R^2dR}$$

$$\begin{aligned}
 &= -\left[u' + \frac{u^2u'}{R^2} + \frac{2uu'}{R} + \frac{u^2}{R^2} + \frac{2u}{R} \right] \\
 &= -\left[\epsilon_r + 2u \frac{\epsilon_r + 1}{R} + u^2 \frac{\epsilon_r + 1}{R^2} \right] \quad (3a)
 \end{aligned}$$

$$\epsilon_t = u \frac{\epsilon_r + 1}{R} + \frac{u^2}{2} \frac{\epsilon_r + 1}{R^2} \quad (3b)$$

$$C = -\epsilon_r - 2\epsilon_t. \quad (3c)$$

APPENDIX F

FORMULAS FOR SOUND SPEED IN ELASTIC-PLASTIC MATERIAL

Notation

$$v = \text{specific volume} = 1/\rho$$

$$v_0 = \text{initial specific volume} = 1/\rho_0$$

$$V = v/v_0 = \text{relative volume}$$

$$\mu = (v_0 - v)/v$$

$$C = (v_0 - v)/v_0$$

$$\rho_0 = \text{initial density}$$

$$\rho = \text{true density}$$

The definition for the longitudinal adiabatic sound speed is

$$c_L = \left(\frac{\partial \Sigma}{\partial \rho} \right)^{\frac{1}{2}}$$

$$\left. \begin{aligned} \frac{\rho_0}{\rho} &= \frac{v}{v_0} \\ \end{aligned} \right\} \quad \begin{aligned} v &= \frac{v_0 \rho_0}{\rho} \\ \frac{\partial v}{\partial \rho} &= - \frac{v_0 \rho_0}{\rho^2} = - \frac{v^2}{\rho_0 v_0} \end{aligned}$$

$$\frac{\partial \Sigma}{\partial \rho} = \frac{\partial \Sigma}{\partial C} \frac{\partial C}{\partial V} \frac{\partial V}{\partial \rho} = \frac{\partial \Sigma}{\partial C} \left(- \frac{1}{v_0} \right) \left(- \frac{v^2}{\rho_0 v_0} \right) = \frac{\partial \Sigma}{\partial C} \frac{1}{\rho_0} \left(\frac{v}{v_0} \right)^2 = v^2 \frac{1}{\rho_0} \frac{\partial \Sigma}{\partial C}$$

$$\frac{\partial \Sigma}{\partial \rho} = \frac{\partial \Sigma}{\partial \mu} \frac{\partial \mu}{\partial V} \frac{\partial V}{\partial \rho} = \frac{\partial \Sigma}{\partial \mu} \left(- \frac{v_0}{v^2} \right) \left(- \frac{v^2}{\rho_0 v_0} \right) = \frac{1}{\rho_0} \frac{\partial \Sigma}{\partial \mu}$$

Thus,

$$c_L = \left(\frac{\partial \Sigma}{\partial \rho} \right)^{\frac{1}{2}} = v \left(\frac{1}{\rho_0} \frac{\partial \Sigma}{\partial C} \right)^{\frac{1}{2}} = \left(\frac{1}{\rho_0} \frac{\partial \Sigma}{\partial \mu} \right)^{\frac{1}{2}}$$